UNIVERSITÀ
DEGLI STUDI
DI PADOVA

UNIVERSITA' DEGLI STUDI DI PADOVA

Department of Industrial Engineering

Master Thesis in Energy Engineering

Numerical analysis of hydrodynamic cavitation. Influence of vapour compressibility in the cavitation model.

Supervisor: Prof. Anna Stoppato

Co-supervisor: Ing. Edoardo Sech

Candidate: Luca Simioni

Student ID: 2062304

Academic year 2023/2024

Abstract

The purpose of the work is to build a CFD model of hydrodynamic cavitation in a Venturi. Considerations about the compressibility of the vapour phase are conducted, and a function describing the equation of state of the phase is created. The function is added to the model in order to describe in a more realistic way the cavitation phenomena. A numerical simulation is performed, and the results are validated with those founded in the literature.

Table of contents

1 Introduction 1

2 Cavitation 5

2.1 Cavitation technologies 8

2.1.1 Laser cavitation 8

2.1.2 Acoustic cavitation 9

2.1.3 Hydrodynamic cavitation 10

2.2 Hydrodynamic cavitation in a venturi nozzle 11

2.3 Cavitation's dimensionless numbers 14

2.3.1 Cavitation number σ 14

2.3.2 Loss factor K 15

2.3.3 Strouhal number St_d 15

3 Mechanism of shedding 17

3.1 Re-entrant jet shedding 19

3.2 Condensation shock shedding 21

4 Vapour compressibility 25

4.1 Ideal gas behaviour 25

4.2 Density 30

4.3 Speed of sound 32

4.3.1 Speed of sound in mixtures 35

5 CFD model 37

5.1 CFD modelization procedure 37

5.1.1 Pre-processor 38

5.1.2 Solver 38

5.1.3 Post processor 39

5.2 Governing equations 39
5.2.1 Conservation of mass 39
5.2.2 Navier-stokes equations 40
5.2.3 Energy equation 40
5.2.4 Equation of state 41
5.3 Turbulence 41
5.3.1 RANS governing equations 44
5.4 Turbulence models 44
5.4.1 k-ε model 44
5.4.2 k-ω model 45
5.4.3 k-ω SST 46
5.4.4 Dimensionless number Y+ 49
5.5 Cavitation model 52
5.5.1 Schnerr-Sauer model 54
5.5.2 Zwart-Gerber-Belamri (ZGB) model 55
6 Construction of the model 57
6.1 Fluid properties 58
6.2 Ansys Fluent geometry 59
6.3 Meshing process 61
6.3.1 Mesh quality 63
6.3.2 Mesh constructions 65
6.3.3 Problems in the mesh construction 67
6.4 User Defined Functions (UDF) 67
6.4.1 Vapour compressibility UDF 68
6.4.2 Turbulent viscosity UDF 69
6.5 Sensitivity analysis and choice of the mesh 70

6.6 Setup and initialization 77
6.6.1 General settings 77
6.6.2 Models 77
6.6.3 Materials 77
6.6.4 Boundary conditions 78
6.6.5 Methods 78
6.6.6 Controls 79
6.6.7 Calculation 80
6.6.8 Initialization 80
7 Results 81
7.1 Analysis 81
7.1.1 Re-entrant jet mechanism 83
7.1.2 Condensation shock 86
7.1.3 Differences from experiment 89
7.2 Validation 91
7.3 Model limitations 96
8 Conclusion 99
9 Bibliography 101

List of figures

Figure 2-1: Phase diagram describing the two processes of boiling and cavitation [3]. .. 5
Figure 2-2: Evolution of the implosion of a vapour bubble collapse [4]. 6
Figure 2-3: Three different zones of the cavitation phenomena described in the hot-spot theory [5]. 7
Figure 2-4: Laser cavitation working principle for a surface process [7]. 8
Figure 2-5: Illustration of acoustic cavitation throughout external ultrasonic wave propagation [8]. 9
Figure 2-6: Typical damage of cavitation in a Francis turbine runner [10]. 10
Figure 2-7: Schematic descriptions of the hydraulic implant of a hydrodynamic cavitation reactor [6]. 12
Figure 2-8: Profiles of the local pressure (b) and velocity (c) along the venturi tube [1]. 13
Figure 3-1: Typical vortex cavitation in a venturi tube [14]. 17
Figure 3-2: Position of a travelling bubble in a venturi tube at different timesteps [15]. 18
Figure 3-3: Sheet or partial cavitation in a foil [3]. 18
Figure 3-4: partial and cloud cavitation occurring at the same time in foil [3]. 19
Figure 3-5: Deviation of fluid streamlines around the vapour cavity [1]. 19
Figure 3-6: Bubble tracking video frames of the reverse jet shedding [1]. 21
Figure 3-7: X/t diagram representing the condensation shock mechanism in the venturi [1]. 22
Figure 3-8: Path of the wave front in the X/t diagram [1]. 23
Figure 3-9:Bubble tracking video frames of the condensation shock shedding mechanism [1]. 23
Figure 4-1: critical point of water [24]. 27
Figure 4-2: Nelson Obert's compressibility charts [25] 29
Figure 4-3: Particles positioning during the transmission of a sound wave [29]. 33
Figure 4-4: Comparison between Woods and Nguyen models to calculate the speed of sound in a mixture varying the volume fraction of air into an air-water mixture. In the

figure, eff cw and eff cg, are parameters for the calculation of the Nguyen formula. In the graph on the abscissa of the graph there is the volume fraction of air [35]. 35
Figure 5-1: Schematic representation of laminar flow in a tube [43]..... 42
Figure 5-2: Schematic representation of turbulent flow in a tube [43]. 42
Figure 5-3: Typical point measurement of velocity in turbulent regime [38] 43
Figure 5-4: Values of the blending function depending on its distance to the wall [44]. 47
Figure 5-5: Turbulent flow average velocity variation near the wall [49]..... 49
Figure 5-6: correlation between the two dimensionless parameters $Y+$and $u+$ [51]. . 51
Figure 5-7: First row: real representation of a vapour cloud formation. Second row: representation of the real flow with a volume fraction method. Third row: concentration of bubbles in the real flow [52]. 53
Figure 6-1: Schematic representation of the experimental set-up used in [1]. 57
Figure 6-2: Geometrical properties of the venturi tube [1]. 58
Figure 6-3: Geometric construction in the Ansys Fluent software. 60
Figure 6-4: Illustration of the four different sections in the geometry. 61
Figure 6-5: Example of a 2D structured and unstructured grid [57]. 62
Figure 6-6: Aspect ratio of two different cells [60]. 63
Figure 6-7: Illustration of the skewness parameter [59]. 64
Figure 6-8: illustration of the orthogonality parameter [59]..... 64
Figure 6-9: Mesh created by default in Ansys Fluent using only the face meshing tool.65
Figure 6-10: Mesh constructed in Ansys fluent at the inlet of the domain. 66
Figure 6-11: Distribution of the cells at the throat. 67
Figure 6-12: UDF compiled for the vapour density.**Errore. Il segnalibro non è definito.**
Figure 6-13: UDF compiled for the turbulent viscosity.**Errore. Il segnalibro non è definito.**
Figure 6-14: Inlet pressure variation during the numerical simulation. 72
Figure 6-15: Results of the sensitivity analysis. 73
Figure 6-16: Results of the final sensitivity analysis..... 75
Figure 6-17: Value of the aspect ratio in all the domain. 76
Figure 6-18: Skeweness parameter in the domain. 76
Figure 6-19:Orthogonal quality in the domain. 76

Figure 7-1: Comparison between bubble implosion in the transient (a) regime and after (b). 82
Figure 7-2: Re-entrant jet mechanism in the model with the operating conditions $\sigma D = 0{,}88$..... 84
Figure 7-3: evolution of axial velocity in the model with the operating conditions: $\sigma D = 0{,}88$..... 85
Figure 7-4: Condensation shock mechanism of the model with $\sigma D = 0{,}46$. 87
Figure 7-5: axial velocity for different flow times at $\sigma D = 0{,}46$. 88
Figure 7-6: K as a function of σD. 92
Figure 7-7: K as a function of CN. 93
Figure 7-8: Lines used for the frequency analysis..... 94
Figure 7-9: Std as a function of σD. 95
Figure 7-10: Std as a function of CN..... 96
Figure 7-11: values of $Y+$ at the divergent with a cavitation number $\sigma D = 0{,}51$..... 97
Figure 7-12: values of $Y+$ at the divergent with a cavitation number $\sigma D = 0{,}88$..... 98

1 Introduction

Hydrodynamic cavitation is a physical phenomenon that is often studied in fluid mechanics and turbomachinery. Due to a local decrease of pressure under the saturation conditions of the liquid, vapour bubbles appear in the fluid. When the pressure returns to its previous values, vapour cavities or bubbles suddenly implode. Depending on the dynamic conditions, these bubbles can agglomerate forming a big cavity of vapour in the fluid or remain homogeneously dispersed in the liquid phase. How the vapour cavity behaves and evolve during the phenomenon determines the type of shedding characterizing the cavitations process. The implosion of a bubble leads to a significant local release of energy within the system, generating extremely high temperatures, up to $5000\ K$, as well as pressures reaching $500\ atm$, along with the formation of liquid jets and ultrasonic waves. These implosions in most of fluid machinery are an issue, as they erode the materials, increase the drag force and create vibrations, leading to a decrease in the performance. Despite these negative effects, in the last years cavitation has been studied for its high potential in integration in various industrial processes. The idea is to concentrate the physical and chemical energy released by cavity implosions in specific energy consuming processes. This can be used to trigger chemical reactions or physical processes, which can be used in a wide range of applications, going from food industry to oil refinery, but also from wastewater treatment to biomass pretreatment. The use of cavitation reactors can be more energy efficient and less pollutant with respect to traditional processes. For this reason, the study of cavitation reactors has developed in the last years. Hydrodynamic cavitation obtained by forcing the fluid inside a nozzle or an orifice, results the most efficient and used technology in industrial scale. The venturi tube geometry consists in three different parts: the converging, the throat and the diverging section. The simplicity of construction, coupled with the reduction in pressure losses compared to the corresponding configuration using orifices, makes it the most used geometry in literature and the one chosen for this study.

Cavitation is an extremely complex phenomena due to the interplay of different physical phenomena, such as turbulence, multiphase flow and bubbles dynamics; furthermore, it happens in few milli or microseconds. Because of this, experimental cavitation studies

are extremely costly, requiring high-tech machinery and software to capture all the transitional processes. To overcome this problem computational fluid dynamic (CFD) models are used. These mathematical models solve the Navier Stokes equations that describe the behaviour of the fluids motion, trying to simulate numerically what occur in reality. The exact representation of the phenomenon in a CFD model would require an extremely high computation cost and the Navier Stokes equations are non-linear complex equation, that in many cases cannot be resolved correctly. For these reasons, some simplifications are used in the models, to reduce the computational cost and simplify the solution. Finding solutions with less simplification as possible is crucial to obtain a result that reflect the reality of the phenomena studied. In cavitation CFD models, one of the most used simplifications is the incompressibility of the fluid. Previous studies carried out at the University of Padua on hydrodynamic cavitation took this hypothesis as the basis for the first approach of the problem. These becomes the basis for the actual work, The objective of this thesis is to improve the existing CFD model taking into count the vapour compressibility. Starting from the equations describing the behaviour of the gas in the cavitation phenomena, an equation of state describing the variation of density based on local pressure is obtained and implemented with a user defined function, UDF. Of particular interest are also the evaluations made on the turbulent viscosity. According to the literature, this parameter is strongly penalising the possibility to simulate the real movement and periodicity of the vapour cavity. Then the model is validated according to the experimental data available in the literature, performed by Jahangir [1], and the work of Brunhart [2]. To build the CFD model Ansys Fluent 2024 R1 software is used. First of all, the geometry according to the work of Brunhart [2] is built, then the meshing of the geometry is performed. To verify the robustness of the mesh, a sensitivity analysis among four different meshes is carried out. The parameters taken in consideration to perform the sensitivity analysis are the difference of pressure between inlet and outlet of the venturi reactor and the computational time to get an entire cavitation cycle; the mesh chosen for the later computational studies is a compromise between these two factors. The setup of the simulation is realized basing mainly on the literature. The most used and verified sub models that in literature reflect with good accuracy the experimental results are applied. Boundary conditions are settled following Brunhart [2]. After that, the initialization is carried out: first a stationary simulation with incompressible water is performed, then,

from this solution, the cavitation process involving the two user defined functions describing the vapour compressibility and the turbulent viscosity of the mixture, are implemented. In the numerical solution, first a transient regime appears. After $30\ ms$ are computed, the transient ends and the process of cavitation start with thermodynamic values and frequency that reflect the reality. The values used to verify the model with the experimental results are collected in the simulation, when the time needed for a fluid particle to get from the inlet to the outlet of the tube is reached. From the results the dimensionless numbers of the cavitation process are calculated and compared to the one obtained in the works of Jahangir [1] and Brunhart [2]. Also, considerations about the shedding mechanism are conducted. Those are based on the evolution of the vapour cavity during the cavitation phenomenon and are compared with the works taken as reference.

2 Cavitation

Cavitation identifies the physical phenomenon of appearance of vapour cavity or micro bubbles inside a homogeneous fluid. Its explanation could be described by observing the water phase diagram in Fig. 2-1. The phase transition from water to vapour happens when the values of pressure and temperature cross the vapor saturation curve. Starting from water at ambient conditions, there are two main ways for this to happen as showed in the Fig. 2-1: one is to increase the water temperature, the second is to decrease the pressure. The first method represents the well-known phenomenon of boiling. At atmospheric pressure increasing the temperature over $100°C$, water reaches the saturation curve and starts boiling becoming steam. While the second case represents cavitation phenomenon: having water at ambient condition and decreasing the pressure at constant temperature under the saturation curve, vapor cavities start appearing [3].

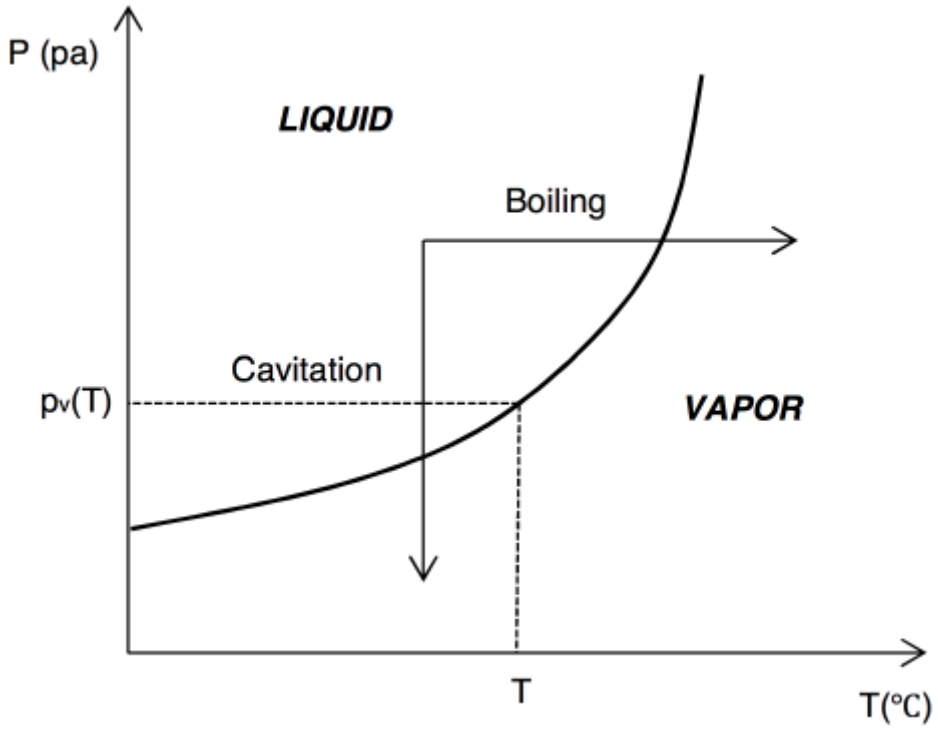

Figure 2-1: Phase diagram describing the two processes of boiling and cavitation [3].

Cavitation is based on three steps. First voids or micro bubbles start appearing due to the decrease of pressure. The initiation of cavitation is favoured by small air or gas particles that are always present in the fluid, or by some discontinuities in the solid surface. These factors act like cavitation nuclei. Then after that the bubble is initiated, it grows up if the pressure remains under the saturation vapor limit, reaching a maximum size. Finally, when it reaches a zone where there is a sudden increase of pressure, it evolves into an adiabatic compression, bringing to the collapse of the bubble. This collapse releases a large amount of energy in the fluid and leads to the formation of micro jets and shock waves. In Fig 2-2, the bubble collapse is illustrated in five different timesteps [4].

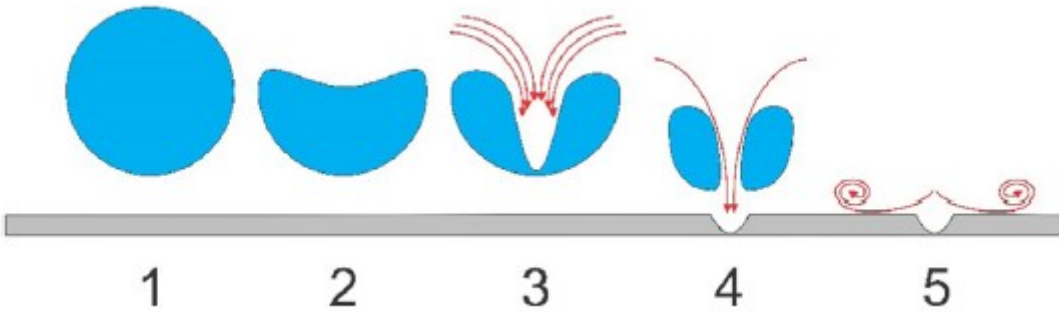

Figure 2-2: Evolution of the implosion of a vapour bubble collapse [4].

Various theories have been used to describe the bubble collapse: the most used is the hot spot theory illustrated in Fig. 2-3 and discussed by Adewuyi [5]. This suggest that the cavity is divided in three different reacting zones: a hot gaseous nucleus, a bulk solution at ambient temperature and an interface region with radial gradient of temperature and density. The gaseous nucleus is the inner zone of the cavity. Here temperatures of $5000\ K$ and pressure of $500\ atm$ are reached, providing the activation energy for the bond cleavage of the atoms, and so creating radicals and other highly reactant excitation states. Radicals formed react with each other or diffuse in the proximity of the cavity acting like an oxidant. In the shell immediately around the cavity implosion the bulk liquid reaches temperatures up to $2000\ K$. Here two types of reactions occur: the oxidization of free radicals formed in the core, which diffuse in this region, and the pyrolysis reactions. Most of the particle degradation take place in this bubble-cavity interface. After, in the bulk zone, which is the external side, the last free radicals diffuse and react with molecules in the bulk. In Fig.2-3 the three different zones are illustrated.

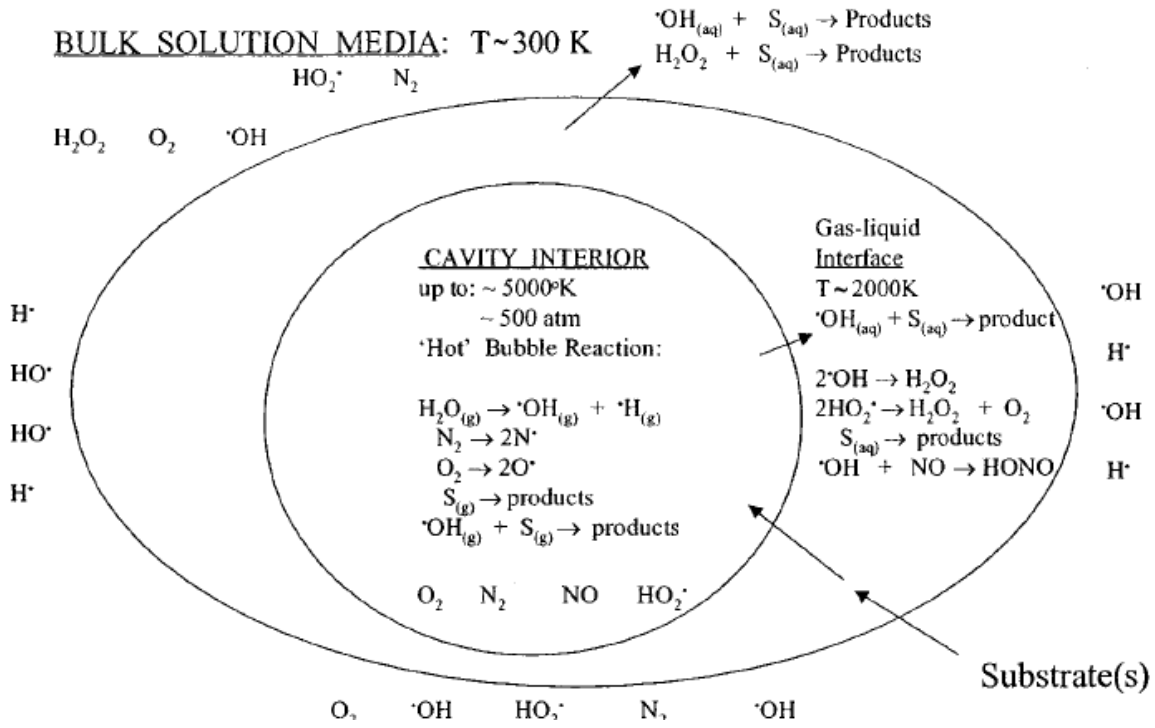

Figure 2-3: Three different zones of the cavitation phenomena described in the hot-spot theory [5].

There are two types of bubble collapse: symmetric and asymmetric. These types of collapse emit the same quantity of energy but lead to different physical phenomena. In the symmetric collapse, the cavity grows without any physical constrain and remains spherical until the implosion. Here the formation of free radicals and pyrolysis reactions are favoured. Symmetrical collapse is appropriate if the main aim of the cavitation is to operate from a chemical point of view in the bulk fluid. Instead, if there are some constrains in the proximity of the cavity, the collapse is asymmetric. In this case the bubble does not grow up spherically due to the constrain, and the implosion creates high velocity micro-jets and high local turbulence, favouring physical transformations differently from the symmetrical case. Asymmetric cavitation may be used for the emulsion of fluids or erosion of some solid particle [5] [6].

2.1 Cavitation technologies

Nowadays there are three main technologies to generate cavitation: laser, acoustic and hydrodynamic cavitation. The common basic principle behind all these methods is the imposition of a pressure variation in the fluid, generating alternating high and low pressure peaks, which fall below the vapour pressure value creating vapour cavities.

2.1.1 Laser cavitation

In this process the laser beam focalizes in a small area and its energy is absorbed by water. The water heats up creating a vapour bubble that increases his size, as long as the pressure inside the bubble is higher than the one of the liquid. When this pressure condition is not respected, the bubble is compressed and then collapse. The main advantage of this kind of cavitation is that the cavitation phenomenon is more controllable. With the laser technology bubbles position are well controlled and they evolve into a perfect spherical way. That's the reason why this method is used in the micro-electronics or micro milling and in many biomedical applications [7]. In Fig. 2-4 the working principle of this method is illustrated.

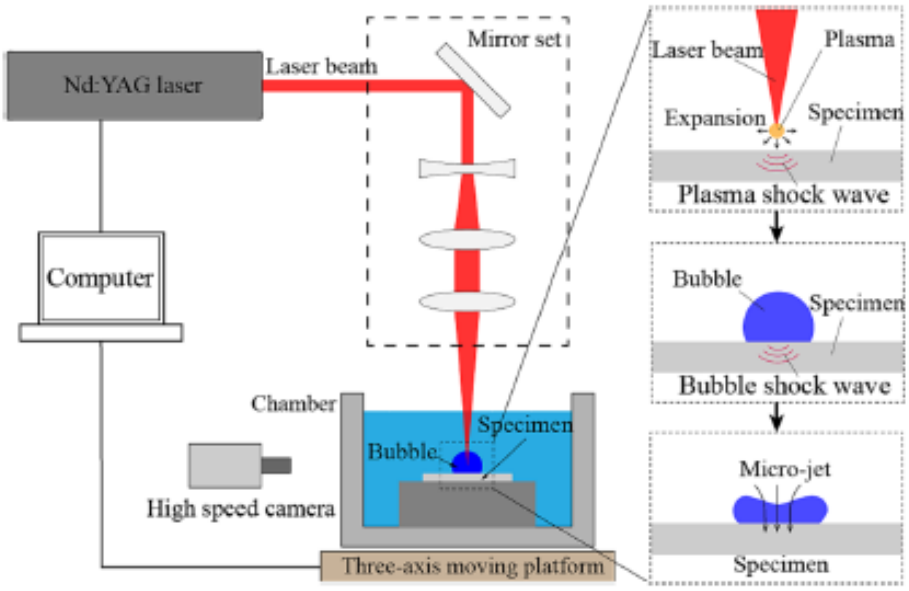

Figure 2-4: Laser cavitation working principle for a surface process [7].

2.1.2 Acoustic cavitation

Another method is the acoustic cavitation. Sound is constituted by the movement of pressure waves through a medium, occurring in cycles of compression and expansion. In a liquid transmitting ultrasound wave with a frequency higher than 20 *Hz*, the expansion produced exceeds the tensile strength between the molecules of the medium, creating the cavitation bubbles. As illustrated in Fig. 2-5, along the cycles of compression and rarefaction of the sound wave, the bubbles can increase their size arriving than at a critical point and finally collapse. Acoustic cavitation is used for sonochemistry, using the sound waves and the radicals generated by the collapse of the cavitation phenomena for chemical reaction. There are also research where acoustic cavitation is used for physical phenomena like cleaning and erosion [8] [9].

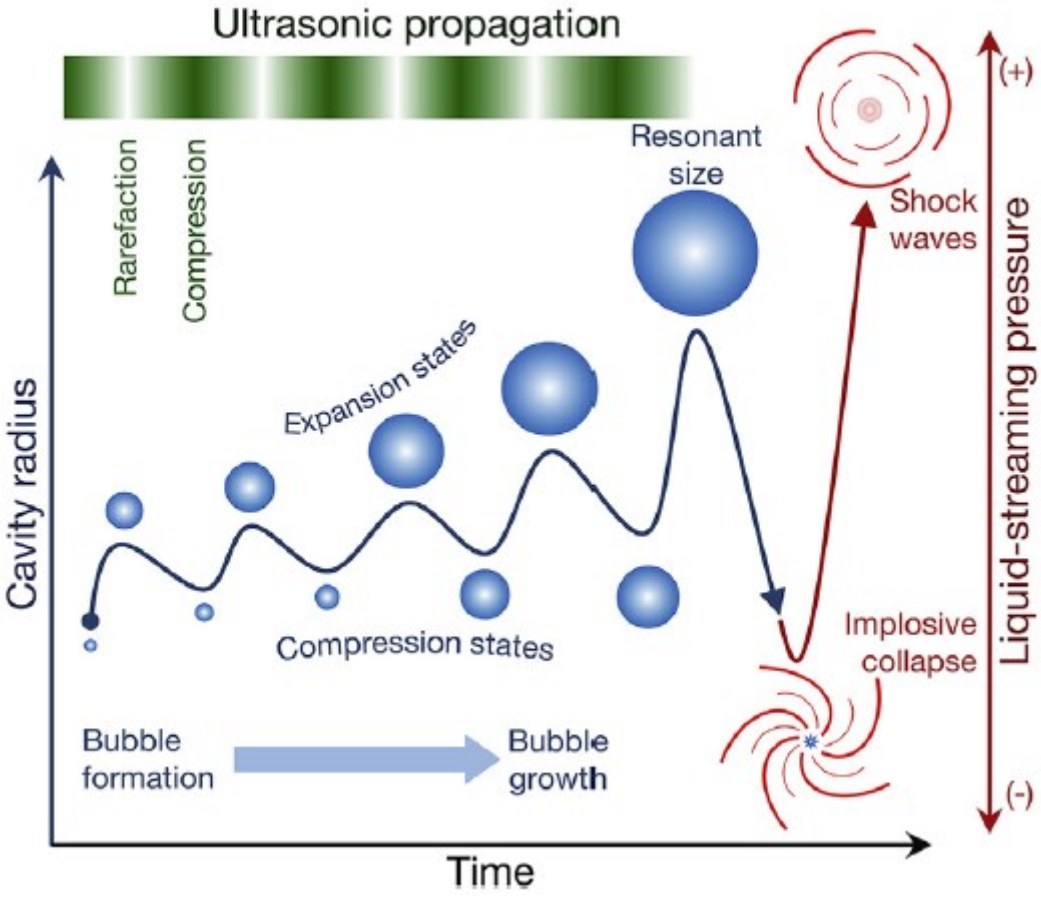

Figure 2-5: Illustration of acoustic cavitation throughout external ultrasonic wave propagation [8].

2.1.3 Hydrodynamic cavitation

Hydrodynamic cavitation is a well-known phenomenon that has been studied a lot in fluid mechanics, as it appears in machinery operating with water. Basing on the Bernoulli theorem in fluid dynamics (neglecting the potential energy of the fluid), a sudden increase in the velocity determines a decrease in the pressure. Once that the saturation curve is reached, vapour bubbles start appearing. In fluid dynamics machinery like pumps, turbines or some valves cavitation may occur and is generally not desired. Its main disadvantages are:

- A decrease in plant performances, increasing the drag force.
- Noise and vibration due to the shockwaves generated in the implosion of the bubbles.
- Erosion of the runner, reducing the lifetime of the machine.

To avoid cavitation specific precautions, it is needed to be take in count in the geometry and in the assembly of the hydro machine. Specific materials or coatings are also used to resist the cavitation erosion [10].

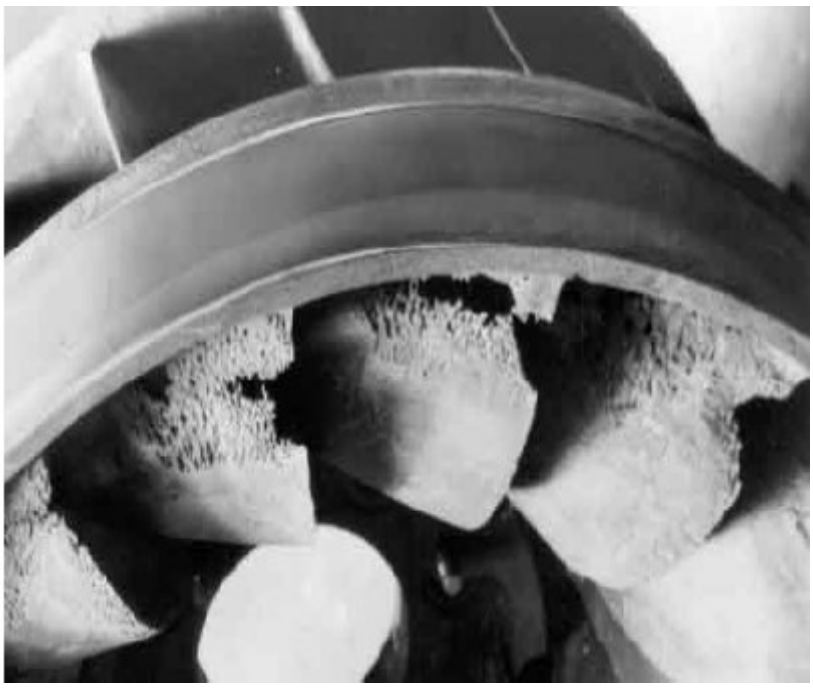

Figure 2-6: Typical damage of cavitation in a Francis turbine runner [10].

2.2 Hydrodynamic cavitation in a venturi nozzle

As already discussed, in hydrodynamic the cavitation phenomenon is usually something to avoid, and many precautions are taken to prevent it. Despite its negative impact on hydrodynamic machinery, recent research has significantly advanced our understanding of cavitation, uncovering new insights into its mechanisms and revealing innovative, beneficial applications in various physical and chemical processes. Following the hot-spot theory explained before, the implosion of the vapour results in a high release of energy that comports the creation of radicals, numerous reactions and various physical phenomenon like re-entrant jets and shock waves. The idea is to use and exploit this energy taking advantage of the chemical reactions and physical processes that occur in the bubble implosions. From the chemical point of view the cavitation with the formation of radicals can activate reactions in the fluid that usually are obtained in fossil fuels reactors or with catalyst. An example is the use of cavitation in the oil refinery where cavitation is adopted to transform molecules of ultraheavy oil into molecules of small hydrocarbons or to crack high molecules compounds [11]. In the same way cavitation can be used for oxidization reactions or synthesis of alcohols. Another alternative use of cavitation regards the water waste treatment. In this process, the pollutants inside the water are pulled, due to drag forces and the pressure difference, towards the vapour bubbles and diffuse in it. Once the bubble collapses, the re-entrant jet fragmentate the pollutants and the high temperatures and pressures produced in the bubble implosion degrade them [12]. Similarly hydrodynamic cavitation is used for biomass pretreatment [13]. All these processes usually require high amount of energy to reach the temperatures and pressure needed for the reactions or physical phenomenon to occur. Hydrodynamic cavitation reactors substitute the traditional ones in a more energy-efficient and sustainable way, as the energy required for the process is the electrical energy at the pump. In the cavitation reactors used for industrial processes the venturi tube is a typical geometry and is the one used in this study. An image of a typical hydraulic plant is showed in Fig. 2-7; it is an open circuit plant, and its dimension depends on the different case of study. The main components are here described:

- Water storage, usually at atmospheric pressure and at ambient temperature.
- Volumetric pump to reach the high pressures needed.

- The venturi nozzle needed to perform cavitation.
- A bypass line to control the mass flow rate at the venturi nozzle.
- Pressure monitors.
- Valves to regulate the flow in the open circuit.

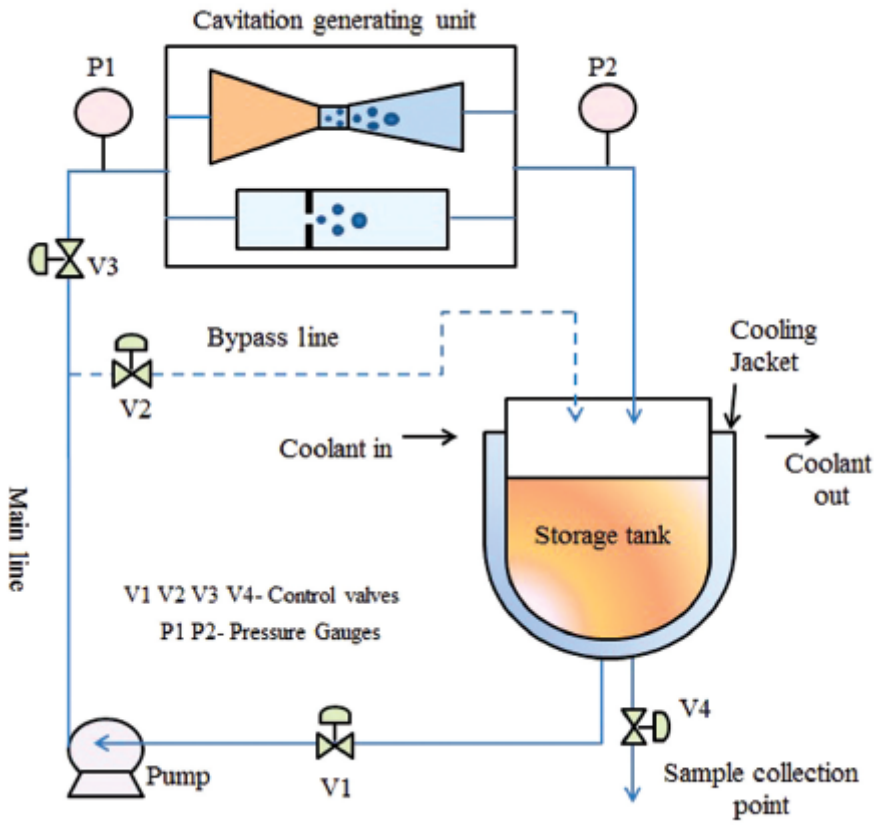

Figure 2-7: Schematic descriptions of the hydraulic implant of a hydrodynamic cavitation reactor [6].

The venturi nozzle is the most important component as it generates the cavitation phenomenon. It is composed in three different sections. First at the inlet of the nozzle there is a convergent side. Here the cross-sectional area diminishes and so, basing on the Bernoulli principle for fluid dynamics, velocity increases as the pressure decrease. The convergent section proceeds until a point of minimum cross-sectional area. Here the fluid pressure arrives at his minimum triggering the inception of cavitation. From this point the second section starts, which maintains a constant cross-sectional area called throat. It is

not present in all venturi nozzles, and in this thesis the venturi used for the numerical research does not have it, as illustrated in Fig 2-8 (a). Then after the throat there is the diverging section: here the cross section slowly returns to the inlet conditions, resulting into a decrease of the speed and increase of pressure. In Fig. 2-8 the velocity and pressure profiles along the venturi tube are represented. In the graphs, u_t represents the throat velocity, u the local velocity, P and P_{max} are respectively the local and maximum pressure in the venturi tube. With L is indicated the whole length of the tube and with x the actual distance from the inlet.

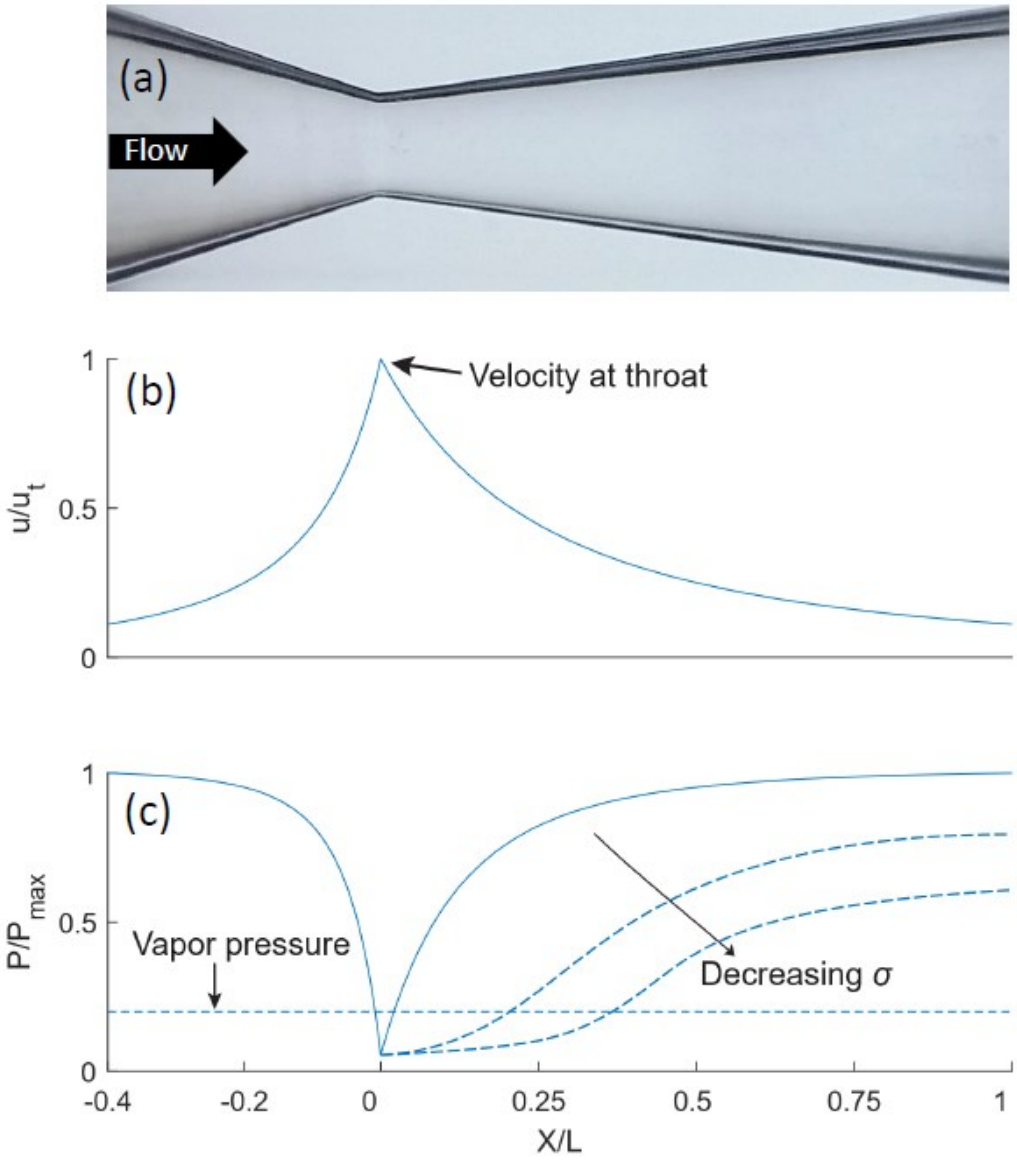

Figure 2-8: Profiles of the local pressure (b) and velocity (c) along the venturi tube [1].

2.3 Cavitation's dimensionless numbers

Dimensionless numbers have an important role in analysing the behaviour of fluids and their flow as well as in other transport phenomena. They typically involve ratios between relative magnitudes of fluids and physical system characteristics, such as density, viscosity, speed of sound, flow speed and hydraulic diameter. Those numbers are fundamental to describe a phenomenon independently from the geometry and the operative conditions considered. As regard cavitation in a venturi tube, dimensionless numbers allow to understand how a scale-up of a model behave and to compare different geometries. In this chapters the main dimensionless numbers involved in cavitation study are presented.

2.3.1 Cavitation number σ

In literature one of the most used parameters is the cavitation numbers σ. This dimensionless number relates the difference between local and vapour pressure with the dynamic pressure of the fluid through the venturi.

$$\sigma = \frac{p - p_{vap}}{\frac{1}{2}\rho u^2} \tag{2.1}$$

In this formula p and p_{vap} are respectively the local and reference pressure, u is the velocity of the fluid, usually measured at the throat and ρ is the liquid density. Depending on what local pressure is measured it is possible to have an upstream and downstream cavitation number.

$$\sigma_D = \frac{p_{down} - p_{vap}}{\frac{1}{2}\rho u^2} \tag{2.2}$$

$$\sigma_U = \frac{p_{up} - p_{vap}}{\frac{1}{2}\rho u^2} \tag{2.3}$$

p_{down} is the pressure measured at the outlet while p_{up} is the pressure at the inlet. The cavitation number indicates if, with those dynamic conditions, the fluid will cavitate or not. With high values of σ fluid will not cavitate while instead with values lower than one cavitation will occur.

2.3.2 Loss factor K

Another dimensionless number in the cavitation process is the loss factor K. This is used as an indicator of the energy losses in the system. A high loss factor K means that high losses are present in the domain. While instead, a factor K near to zero means that no big losses are present. The cavitation process introduces pressure losses in the system increasing so the loss factor. K factor is calculated as:

$$K = \frac{\Delta p}{\frac{1}{2}\rho u^2} \tag{2.4}$$

where Δp is the difference of pressure between inlet and outlet, u is the velocity of the fluid, measured at the throat, and ρ is the liquid density [2].

2.3.3 Strouhal number St_d

The Strouhal number is a dimensionless number used in fluid dynamics to define the oscillatory and periodic phenomenon. Hydrodynamic cavitation in a venturi tube is a periodic phenomenon, in fact the cavitation bubbles inceptions and then implosion occur with a specific frequency. The Strouhal number is defined as:

$$St_d = \frac{f\ D}{u} \tag{2.5}$$

In this formula f is the frequency of the phenomenon, D is the characteristic dimension and u is the local velocity. In this work, as in the one done by Brunhart [2], the characteristic dimension is the throat diameter and for the velocity u is used the average throat velocity.

3 Mechanism of shedding

The distribution of the vapour phase along the venturi can differ basing on the flow and geometric characteristic of the nozzle. Its different development and behaviour distinguish four different types of cavitation.

- Vortex cavitation: Vortex cavitation develops at the core of the vortex where the pressure is below saturation limit. This type of cavitation occurs in hydro propellers at the tip of the blade or it is possible to create vortex cavitation also in a venturi reactor. In this case vortex have a core inclined by 45° with respect to the flow direction and the cavitating bubbles are angulated and not spherical [14]. In Fig. 3-1, the white arrows are indicating the different core of the vortices.

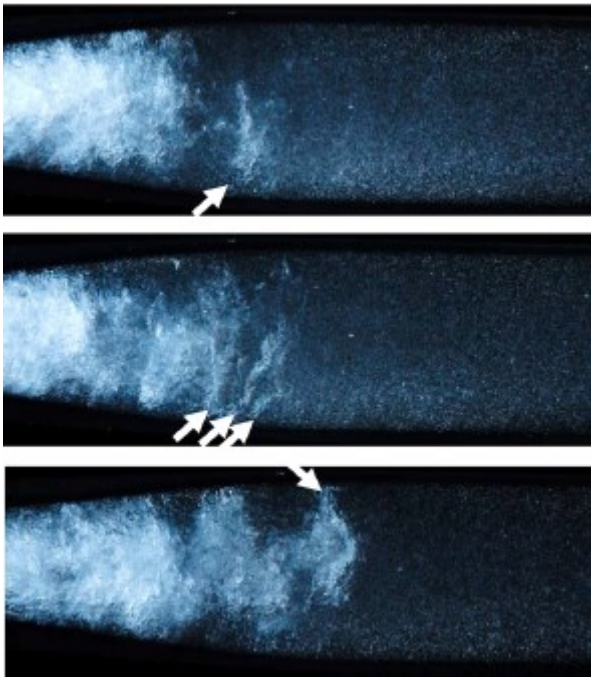

Figure 3-1: Typical vortex cavitation in a venturi tube [14].

- Travelling cavitation: as illustrated in Fig. 3-2, travelling cavitation consists of spherical bubbles that move along the venturi. Bubbles are in general well separated between each other. This type of cavitation can be obtained in venturi tubes rounding the angles at the converging section. In Fig. 3-2 the entire cycle of a single travelling bubble is illustrated. In the image the end of the converging

section, the throat and the start of the diverging part of the venturi are indicated [15].

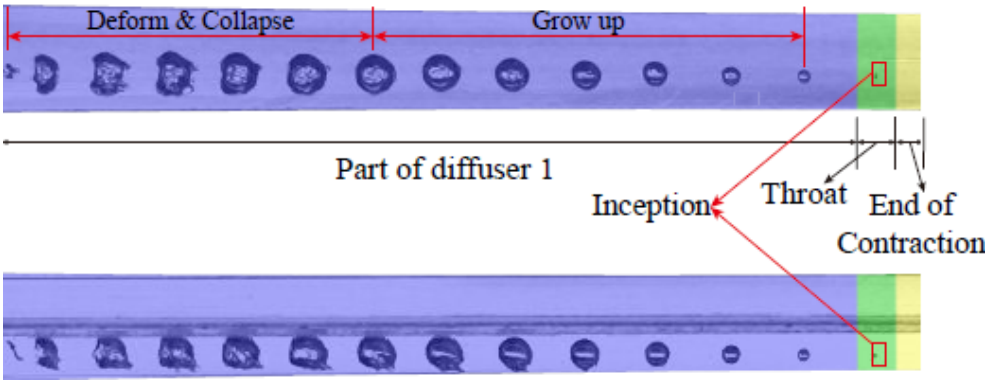

Figure 3-2: Position of a travelling bubble in a venturi tube at different timesteps [15].

- Sheet cavitation: also called partial cavitation in this case, all the cavitated bubbles form a cavity that remains attached to the throat section. This cavity may change in size but always remain attached. In Fig. 3-3 is illustrated the partial cavitation in a hydrofoil.

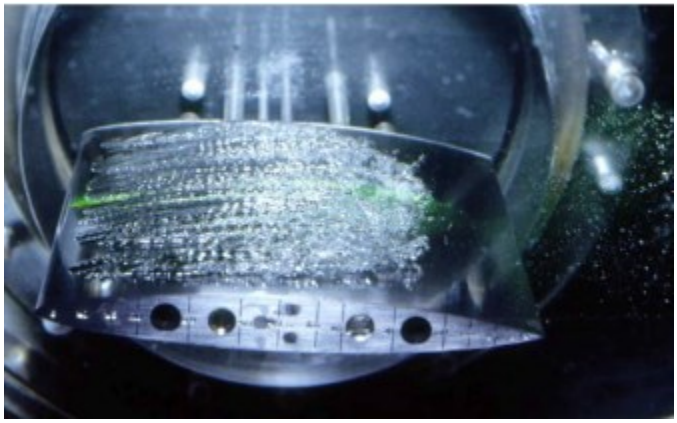

Figure 3-3: Sheet or partial cavitation in a foil [3].

- Cloud cavitation: the cavity of the sheet cavitation, instead of being stable, fluctuates with a cyclic expansion and contraction that occur with a certain frequency. This could compromise the stability of the cavity creating a cloud of small bubbles in the downstream section of the flow.

Figure 3-4: partial and cloud cavitation occurring at the same time in foil [3].

In the present work due to the geometry and dynamic conditions imposed, cavitation reactor operates in sheet cavitation with the vapor cavity that grows in the diverging section of the venturi, remaining attached to the wall. Depending on the flow condition it is possible that cloud cavitation starts appearing. From the cavity two different types of shedding may occur. The re-entrant jet and the condensation shock.

3.1 Re-entrant jet shedding

The main characteristic of the re-entrant jet shedding is the presence of a re-entrant flow in the fluid, moving upwards with respect to the main motion. In fact, as demonstrated by experiment and illustrated in the Fig 3-5, the flow streamlines deviates generating a clock-wise vorticity in order to reach the closure region.

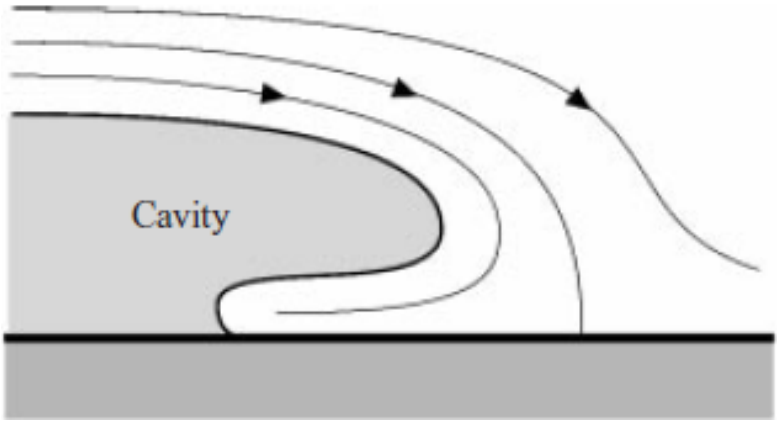

Figure 3-5: Deviation of fluid streamlines around the vapour cavity [1].

Many authors have studied the re-entrant jet phenomenon arriving at important conclusion. In the work of Pham [16] the authors verified that the magnitude of the jet is of the same magnitude of the free stream liquid velocity. Kawanami et al. [17] concluded that re-entrant jet is the mechanism that triggers the cloud shedding, placing an obstruction in the venturi divergent section. Doing so the re-entrant jet could not develop and it was observed that without it cloud cavitation did not occur. The work of Callenaere [18] stated that in this shedding mechanism two parameters are important: the vapor cavity thickness and the entity of the adverse pressure gradient, calculated as the sum of the jet friction losses at the wall and the pressure recovery in the divergent section. He concluded that if the energy provided by the adverse pressure gradient is smaller than the friction losses the jet could not develop, demonstrating how the re-entrant jet shedding is a pressure driven mechanism. A typical cavity cycle is documented in Fig.3-6 by the subsequent bubble tracking video-frames, where with T the total time of a shedding cycle is indicated. Vapour cavity development starts at four milliseconds, after the inception, the cavity starts to grow linearly, and then decreases the growth rate, arriving at a maximum length. During the decrement of the cavity front grow, the re-entrant jet develops flowing in the opposite direction with respect to the main flow. When the reverse jet arrives at the throat, the cavity detaches from it, and the position of the upstream side of the cavity move in less than a millisecond of four millimetres. After the detachment, vapor cloud appears in the divergent part of the venturi tube. The vapour cloud is advected by the main flow and its cavity front velocity increases constantly. This cavity behaviour is also called slip-stick. The upstream side of the vapor cavity is sticking to the throat section, and then as the re-entrant jet arrives at the throat, detach which correspond to the slip of the vapor [1].

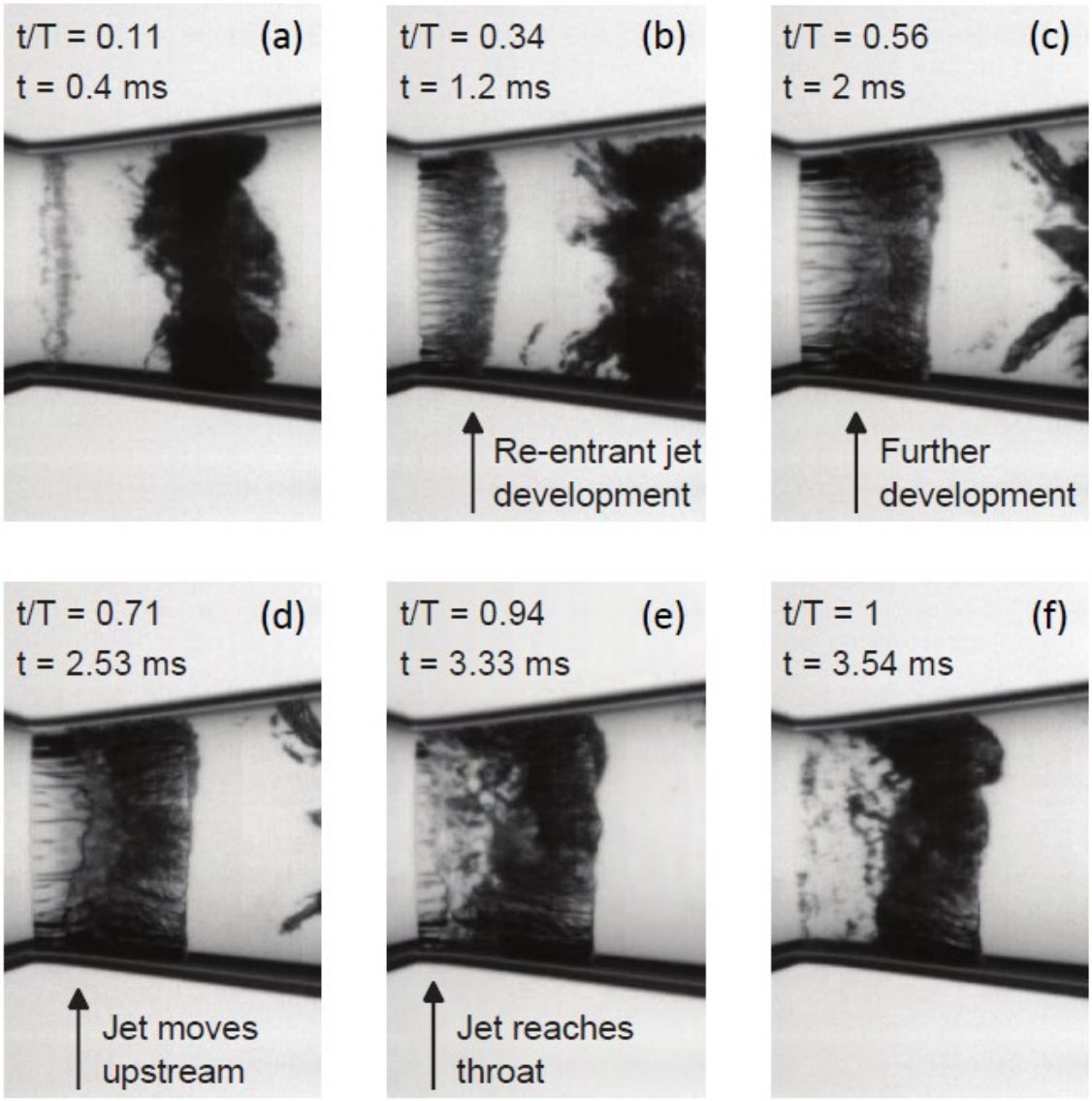

Figure 3-6: Bubble tracking video frames of the reverse jet shedding [1].

3.2 Condensation shock shedding

In the bubbly shock shedding, differently from the re-entrant jet, the driving mechanism are the pressure waves generated by the vapor cloud implosion. To explain in a complete manner this phenomenon an X/t diagram is used. In this graph an image data of the volume fraction is averaged over the Y axis (vertical axis). In this way at an instant time a single line is describing the system behaviour and the vapour volume fraction in the divergent section of the venturi. Stacking up lines for each time instant, it is possible to show in a clear way the periodicity and evolution of the vapour cavity at different time

steps. In Fig. 3-7 with *t* is represented the time X is the local distance from the throat and L is the maximum one.

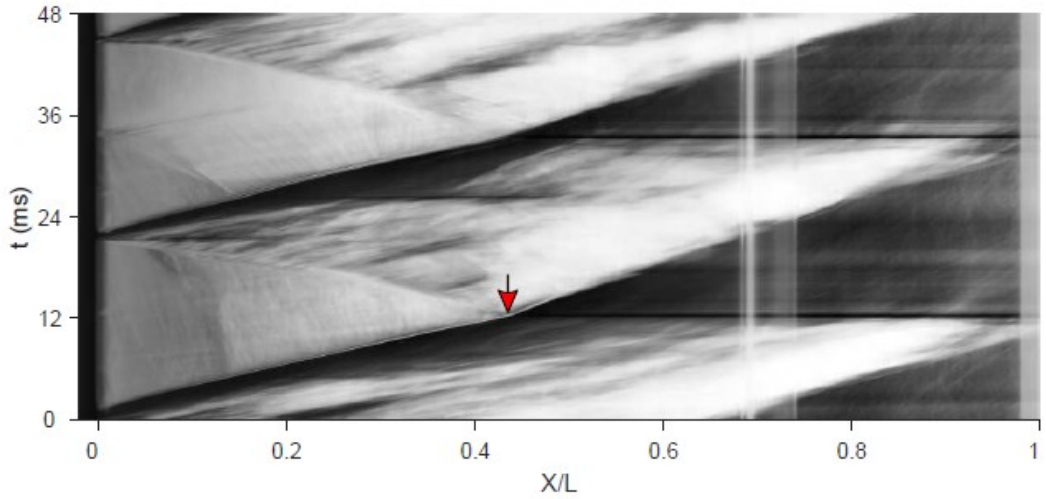

Figure 3-7: X/t diagram representing the condensation shock mechanism in the venturi [1].

From the figure it is possible to observe that cavity trigger at the throat at zero milli seconds. Then with a constant rate grow up and, when a black line, representing the bulk liquid, hits the cavity (in Fig. 3-7 this is pointed out with a red arrow), the grow rate changes, decreasing its value. It is interesting to note that above the interface between the vapor and the liquid, the vapour cloud of the previous cycle vanishes. This means that the implosion of the downstream cavity occurs at that instant propagating in both directions. When the pressure wave arrives at the throat, the cavity detaches from the wall, and is transported downstream with the flow. This detached cavity will be responsible of the next pressure wave, triggering the next cavity detachment. In the vapour attached cavity, after the passage of the pressure wave front, the void fraction decreases because of a partial condensation due to an increase in the pressure. This is well represented in the figure by a change in the colour of the cavity in the X-t diagram. Is also possible to build a path of the pressure wave front along the cavity, well represented by the Fig. 3-8. From this path it is possible to calculate pressure wave-front velocity.

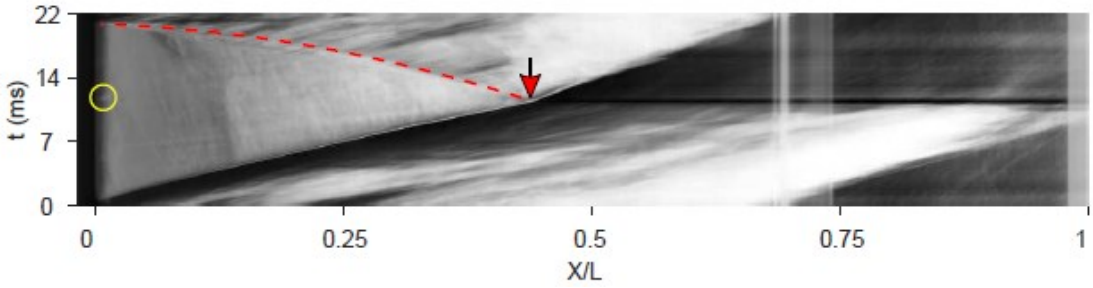

Figure 3-8: Path of the wave front in the X/t diagram [1].

To understand in a more complete way the phenomenon, video frames of the bubbly shock mechanism are reported in Fig. 3-9, indicating how the pressure wave front propagates upstream to the throat section of the venturi. It is evident from these frames, the correlation between the vapor cloud vanishment and the pressure wave effects on the vapour cavity.

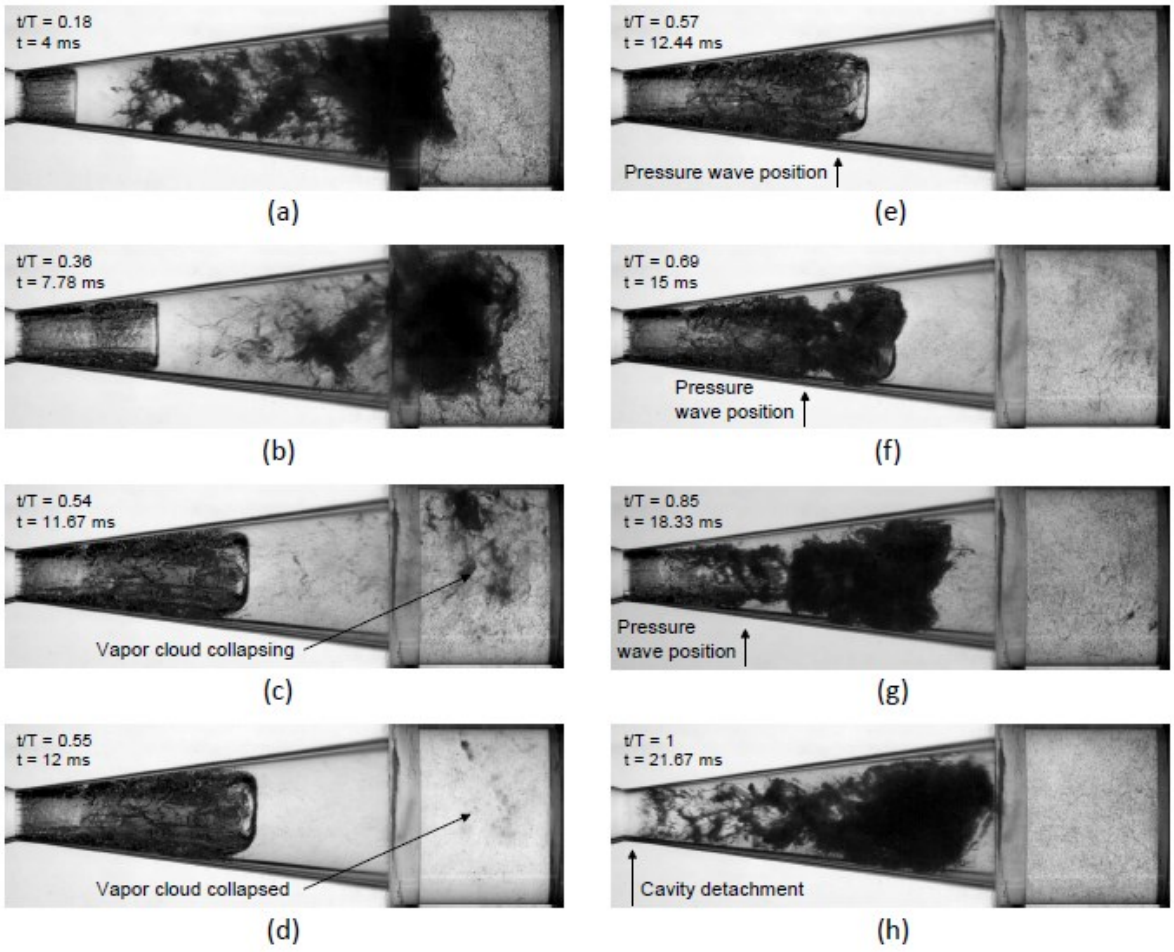

Figure 3-9:Bubble tracking video frames of the condensation shock shedding mechanism [1].

4 Vapour compressibility

In hydrodynamic cavitation phenomenon, cavities of vapour are formed, as already discussed in the previous chapters. Trying to represent the phenomena in a computational fluid dynamic model is a complicated task, as it involves complex flow conditions like turbulence, phase transition, two phase flow and compressible fluids. That is the reason why most of the CFD cavitation models apply some simplifications. One of the most common simplifications is the use of incompressible fluids. In the literature, many authors have introduced compressibility of the fluids to describe the hydrodynamic cavitation more realistically. In the work of Kumar [19] for example the cavitation phenomenon inside a nozzle is studied, analysing the influence of liquid and vapor compressibility. In this work the equations of state used for the fluids are the Tait equation for the liquid phase and the ideal gas law for the vapour. From the numerical simulation it is possible to conclude that the compressibility of the liquid phase made no changes in the cavitation results, having an insignificant role. While instead the results of the numerical analysis using the ideal gas law for the vapour, are closer to the experimental one. In the next sections the physical equations that are implemented and used in the cavitation model to describe the compressibility of the vapour are explained.

4.1 Ideal gas behaviour

For an ideal gas thermodynamic properties follow the ideal gas law, obtained combining the Charles, Boyle and Avogadro laws. Boyle's law state that the volume of a gas at constant temperature is inversely proportional to the pressure.

$$\left(V \propto \frac{1}{p}\right)_{T,n} \tag{4.1}$$

Charles and Gay Lussac found that for a fixed amount of gas at constant pressure the volume varies linearly with the temperature.

$$(V \propto T)_{p,n} \tag{4.2}$$

Finally, Avogadro stated that the volume occupied by the molecules at constant temperature and pressure is independent from the type of gas used.

$$(V \propto n)_{p,T} \quad 4.3$$

From these three statements is possible to obtain the ideal gas law [20].

$$PV = nRT \quad 4.4$$

The main assumptions for an ideal gas are the subsequent [21]:

- The gas particles have a negligible volume with respect to the total volume occupied by the gas.
- Gas particles are equally sized, and there are no interactions between them.
- They move randomly in the volume according to the Newton's law of motions.
- The gas particles have perfect elastic collision between each other without a gain or loss of energy.

It is evident that gases which can completely fulfil all these assumptions do not exist. Any gas particle has a finite volume, depending on the type, they are of different sizes, and they do have intermolecular forces between each other. Collisions between the particles are random but they are not perfectly elastic. To count the deviation from the behaviour of an ideal gas, a factor Z called compressibility factor, for real gases is used [22]. Practically the Z factor is the ratio between the actual volume occupied by the gas and the volume calculated in the same thermodynamic conditions for an ideal gas, using the ideal gas equation of state (4.4).

$$Z = \frac{V_{actual}}{V_{ideal}} \quad 4.5$$

With the compressibility factor it is possible modifying the ideal gas equation of state, to obtain a new equation of state for real gases.

$$PV = ZnRT \quad 4.6$$

The value of the Z factor, change depending on the type of gas and on its thermophysical properties, and for the value of Z=1, the gas behaves like an ideal one. To build a generalized diagram and get the compressibility factor for all gases the principle of corresponding state is used [23]. This principle, discovered by van der Waals, states that substances at the same reduced state behave similarly. The reduced properties of the substances can be obtained with the ratio between the value of the thermophysical property and the relative critical value. Critical properties represent the limit after which

the two phases of vapour and liquid of a substance, cannot be distinguished. As illustrated in Fig. 4-1, this condition is represented in a phase diagram at the end of the vapor-liquid saturation curve. If the fluid overcomes the critical point, enters in a phase called supercritical fluid where the two different phases of the material coexist in the same moment. At this condition, the material has some properties of the liquid, like for example the density, but at the same moment has properties of a gas phase, like the viscosity [24].

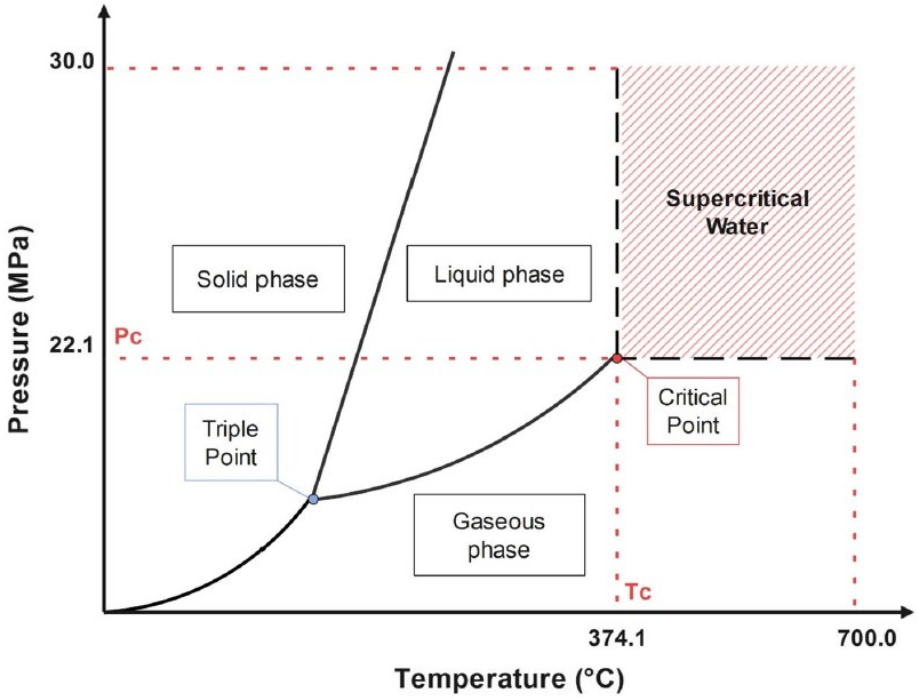

Figure 4-1: critical point of water [24].

So, the principle of corresponding state, affirms that two gases at the same relative departure from their critical conditions, behave similarly. Thanks to this statement it is possible to build a generalized graph like the one in Fig. 4-2 by Nelson Obert, from which is easy to calculate the compressibility factor of the gas, knowing its reduced temperature and pressure. From the diagram it is possible to note that depending on the reduced factors, there are zones where the gas is more compressible than the ideal condition, when Z is higher than one. On the opposite, at lower reduced pressures and temperatures Z is lower than one, indicating that at these conditions the gas is less compressible. There are also some thermophysical conditions, where the compressibility factor reaches a value of one. For this value of the compressibility factor, is evident that the real gas equation of

state (equation 4.6) is equal to the ideal gas (equation 4.4), so for these conditions is possible to conclude that the real gas behaves like an ideal one. As is possible to note in the Fig. 4-2 this happens generally at high temperatures and low pressures.

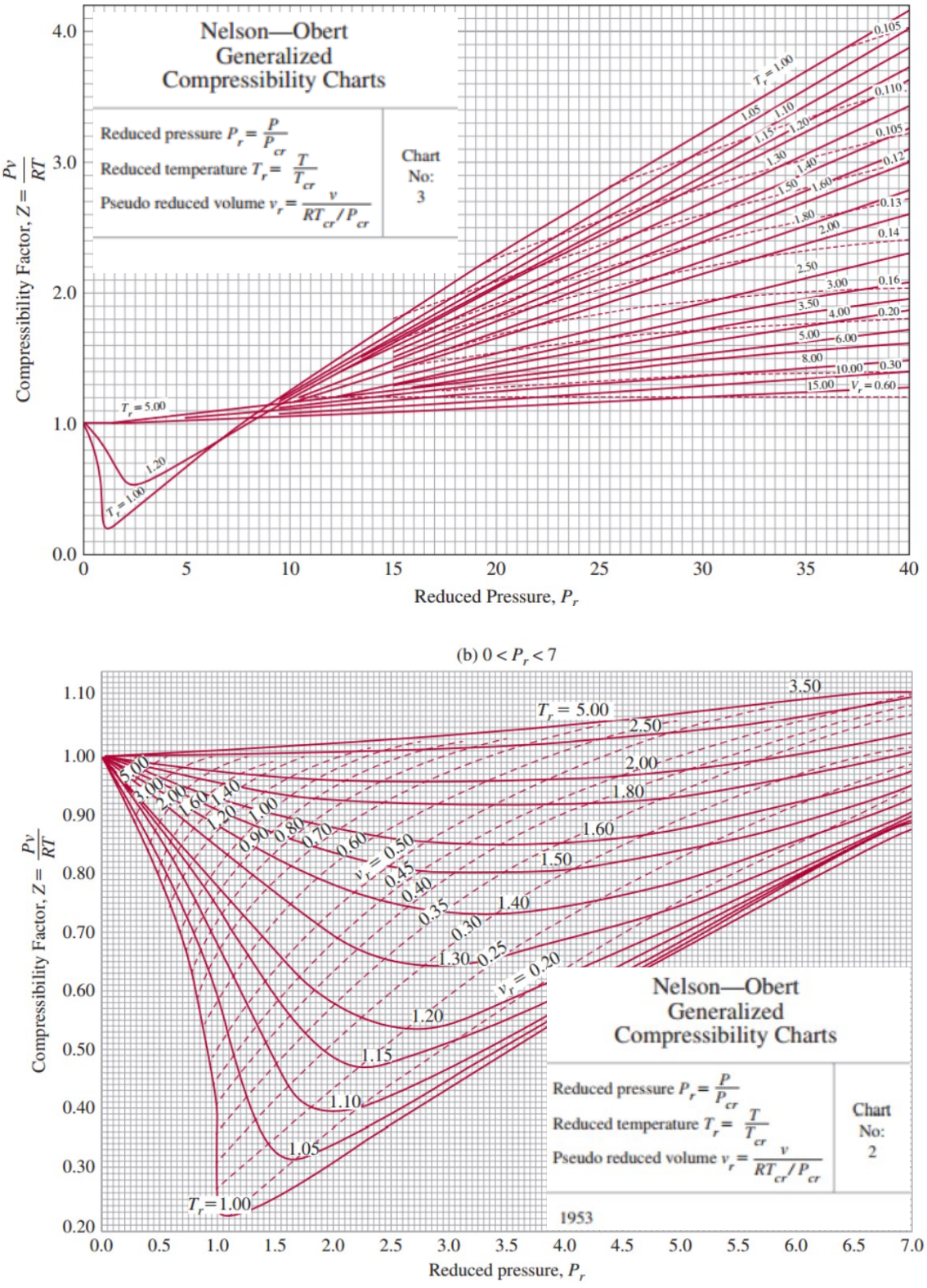

Figure 4-2: Nelson Obert's compressibility charts [25].

In fact, at high temperatures the repulsive and attractive forces between molecules are negligible with respect to their kinetic energy, similarly to the assumption of an ideal gas. In the same way at low pressures, the gas particles are detached among each other, so the interaction between them is negligible and their volume with respect to the whole volume occupied by the gas is small, acting like an ideal gas that has particles with negligible volume and no interaction forces between them. In this work vapour, that appears due to the cavitation phenomenon, is present at pressures that ranges from $400\ Pa$ to $4000\ Pa$. The critical pressure of steam is $220{,}55\ bar$ so also if we take the upper limit of the pressure in our work the reduced pressure is very low.

$$P_r = \frac{P_{actual}}{P_{critical}} = \frac{4 * 10^3}{220{,}55 * 10^5} = 0{,}00018 \tag{4.7}$$

As the value close to zero, is possible to treat the gas as ideal, because the difference with real gas is negligible.

4.2 Density

To relate the pressure of the gas to its density the bulk modulus is used. Bulk modulus, indicated with the letter *k*, is the parameter that define how a volume of a substance varies when is compressed or expanded, relating pressure *p* and the relative change in volume *V*.

$$k = -\frac{dp}{\frac{dV}{V}} = -V\frac{dp}{dV} \tag{4.8}$$

Having a constant mass the density is inversely proportional to the volume of the fluid, so is possible from the above formula to relate the change of pressure with the variation of density [26].

$$k = \rho\frac{dp}{d\rho} \tag{4.9}$$

Talking about ideal gases for compressible flow, is necessary to calculate how the bulk modulus vary with the thermodynamic conditions of the vapour. First, as already said in the chapter describing the cavitation phenomena, the implosion of vapour cavities, where the vapour reaches high pressure and temperatures, happens in a really short time, so that is possible to consider the cavitation an adiabatic phenomenon. For an ideal gas the

adiabatic transformation occurs following the sequent equation of state, where the coefficient γ is the specific heat capacity ratio.

$$p\,V^{\gamma} = constant \tag{4.10}$$

This can be demonstrated knowing that in a gas the internal energy U is a state variable depending on the temperature. And that from the first law of thermodynamics the energy is equal to the heat exchanged minus the work accomplished.

$$dU = nC_v dT \tag{4.11}$$

$$dU = dQ - pdV \tag{4.12}$$

In these formulas, n is the number of moles, C_v is the heat capacity of the gas at constant volume, Q is the heat exchanged (equal to 0 for an adiabatic transformation). From these statements it is possible to calculate the adiabatic bulk modulus for an ideal gas [27] [28]. Deriving in the volume the equation of state for an adiabatic transformation for an ideal gas:

$$\frac{d}{dV}\,(p\,V^{\gamma}) = 0 \tag{4.13}$$

$$\frac{dP}{dV}V^{\gamma} + P\gamma V^{\gamma-1} = 0 \tag{4.14}$$

Dividing the terms per $V^{\gamma-1}$:

$$\frac{dP}{dV}V + \gamma P = 0 \tag{4.15}$$

$$-V\,\frac{dP}{dV} = \gamma P \tag{4.16}$$

And knowing that the definition of bulk modulus is:

$$k = -\frac{dp}{\frac{dV}{V}} = -V\frac{dp}{dV} \tag{4.17}$$

Is possible to conclude that for an ideal gas the adiabatic bulk modulus, k, is:

$$k = \gamma P \tag{4.18}$$

Knowing that the *k* is proportional to the pressure of the gas, is possible now to calculate the value of the density for each different pressure condition thanks to the definition of the Bulk modulus.

$$k = \rho \frac{dp}{d\rho} = \rho \frac{p - p_{ref}}{\rho - \rho_{ref}} \tag{4.19}$$

Knowing the local pressure, the reference pressure and density of the gas, is than possible to calculate the local density.

$$1 - \frac{\rho_{ref}}{\rho} = \frac{p - p_{ref}}{k} \tag{4.20}$$

$$\frac{\rho}{\rho_{ref}} = \frac{1}{1 - \frac{p - p_{ref}}{k}} \tag{4.21}$$

$$\rho = \frac{\rho_{ref}}{1 - \frac{p - p_{ref}}{k}} \tag{4.22}$$

In conclusion it is now possible, knowing the reference properties, to calculate how the density of a compressible ideal gas varies with the variation of local pressure from the reference one.

4.3 Speed of sound

Sound is defined as a mechanical wave that propagates in a medium. The wave is composed by zones of compression where particles are compressed between each other increasing the local pressure of the medium, and zones of rarefaction where particles are farther from each other generating a depression in the medium. The interchanging of this conditions traduces in a sound wave, having an amplitude, frequency and speed. Speed of sound is measured in meters per second and represent the distance covered by the sound wave in the medium for a unit time.

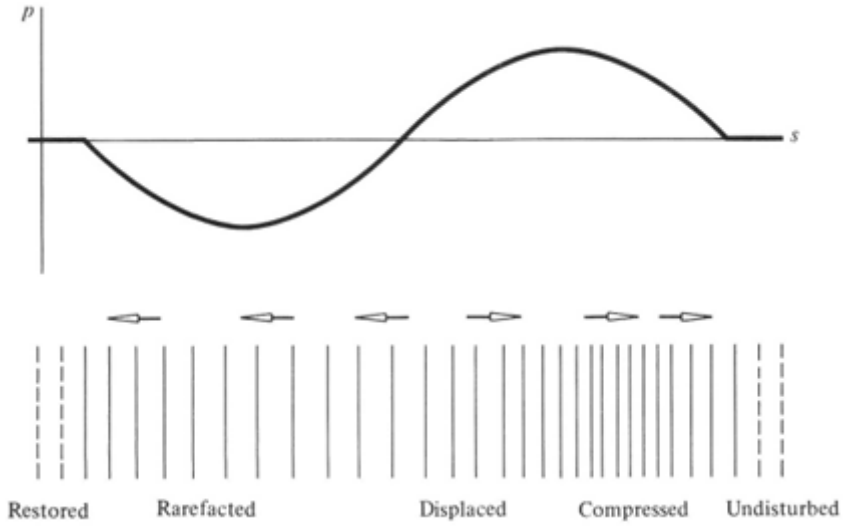

Figure 4-3: Particles positioning during the transmission of a sound wave [29].

As sound is a mechanical wave that transports energy thorough the medium, the sound speed is an indicator of how fast sound or any other mechanical disturbance, travel through the medium [29] [30]. It depends on two factors, the elastic property of the medium and its density. Thinking to the bonds of the particles in a material as springs, the more rigid the spring the faster any disturbance will travel between particles. This means that in mediums where particles are close and bonded by strong forces, like solids, the energy of the disturbance propagates faster and so the speed of sound of the medium will be high. While instead for materials where particles are farther between each other and bounded by weak forces, the disturbances propagate slower, meaning that the medium has a low speed of sound. This indicates that the phase of the material has a big influence in the speed of sound. Solid phase has the higher speed of sound due to the reasons explained above, the gas has the lower while the speed of sound in the liquid phase is in between.

Another factor influencing the speed of sound in a medium is its density. Given a constant volume for two different materials, the one with higher density has heavier particles or a higher number of particles per a unit of volume. The energy of the disturbance propagates under the form of kinetic energy between the particles. Clearly heavier particles need more energy to move and so to transmit the perturbation to the other bounded particles. On the same way materials with a higher number of molecules per unit of volume, will need a higher number of interactions between its molecules needing more time to transmit

the perturbation through the medium. This demonstrate that an increase in the medium density decreases its speed of sound [31] [32]. In the cavitation phenomena presented on this work, a liquid and a gas are present: water and steam. Speed of sound equation mainly derives from the study of the Euler equations in fluid dynamics. For a liquid the speed of sound is calculated by the subsequent formula.

$$c = \sqrt{\frac{K_s}{\rho}} \tag{4.23}$$

Where c is the speed of sound, K_s is the adiabatic bulk modulus of the liquid and ρ is the liquid density. The adiabatic bulk modulus is a measure of the elasticity of the liquid. Higher bulk modulus means lower elasticity and higher speed of sound. Instead for ideal gases the value of the speed of sound according to Laplace, with a constant coefficient of γ defined as the ratio between heat capacity calculated at constant pressure and heat capacity at constant temperature.

$$c = \sqrt{\frac{\gamma p}{\rho}} \tag{4.24}$$

Where p is the local pressure of the gas. In particular, for an ideal gas, knowing its equation of state it is possible to conclude that the speed of sound is only dependent on temperature

$$\frac{p}{\rho} = R\,T \tag{4.25}$$

$$c = \sqrt{\gamma R T} \tag{4.26}$$

This means that for an ideal gas if the temperature is constant its speed of sound does not vary, independently from pressure or density [33] [34] . In most of CFD simulations to simplify the problem and so increase the stability of the numerical simulation, fluids can be treated as incompressible. An incompressible fluid has a constant density independently from any thermodynamic condition, acting like a completely rigid material. This means that for an incompressible fluid the adiabatic bulk modulus is infinite, leading to the conclusion that also the speed of sound is infinite.

4.3.1 Speed of sound in mixtures

Until now talking about the speed of sound only one phase fluids have been considered. But in the cavitation phenomena two phases coexist in a single moment, the liquid and gaseous phase. The speed of sound clearly changes depending on the medium. Taking in example water and steam, where only the water phase is present, speed of sound value is 1498 *m/s*, and must decrease until 423 *m/s* in the portion of domain where only vapour is present. In the zones where the two phases are coexisting, instead the speed of sound arrives to values of less than 20 *m/s*.

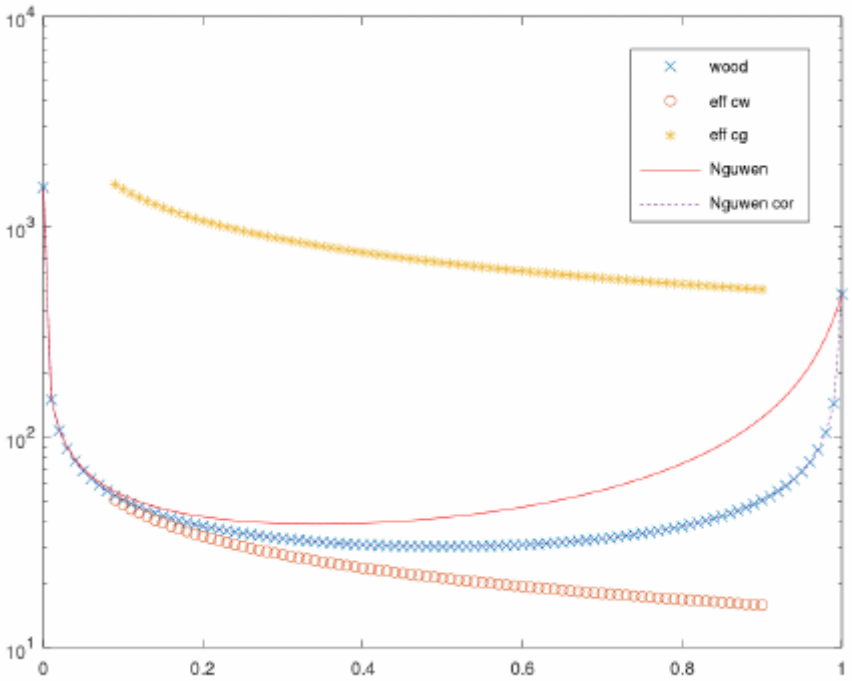

Figure 4-4: Comparison between Woods and Nguyen models to calculate the speed of sound in a mixture varying the volume fraction of air into an air-water mixture. In the figure, eff cw and eff cg, are parameters for the calculation of the Nguyen formula. In the graph on the abscissa of the graph there is the volume fraction of air [35].

Speed of sound in a mixture phase is well explained in Fig. 4.4, taken from the work of Benjelloun et al. [35], where three models to calculate the speed of sound in a water air mixture, are confronted and then validated with experimental data from other studies. As is possible to note in the graph, the speed of sound obtained varying the volume fraction

varies abruptly with a minimum value of the volume fraction of air, arriving at values of $50\ m/s$ with a $0{,}1$ volume fraction of air. Then this value remains more or less constant with the same order of magnitude, and when the volume fraction arrives at a value of $0{,}8$, another abrupt change in the speed of sound occurs, but this time it increases until the value of the speed of sound of air is reached. These low values of the speed of sound occur because the compressibility of the medium changes in the mixture, with air being more compressible than water. When a gas bubble surrounded by liquid is impacted by a pressure wave, it is suddenly compressed, absorbing energy and transmitting the wave significantly more slowly than the surrounding liquid phase. These energy losses are greater than those caused by the transmission of a pressure wave through air alone. For this reason, the speed of sound in the mixture can reach values even lower than the speed of sound in the vapor phase alone. In literature many authors implemented models and equations to describe the speed of sound in mixtures [36] [37]. In particular, Benjelloun [35] discussed and compared many different models for CFD simulations.

5 CFD model

Computational fluid dynamics (CFD) is a branch of fluid mechanics that employs numerical analysis and data structures to analyse and solve problems centring on fluid flows. These kind of analysis is based on solution of the nonlinear Navier-Stokes equations for fluid motion, a set partial differential equations which describe the motion of viscous fluid substances. CFD has become an essential tool in both industrial and research fields due to its numerous advantages. Firstly, CFD models can replace scaled-down prototypes in the development of projects, which are typically necessary to understand the behaviour of full-scale systems. This substitution saves both money and time. Additionally, CFD allows for the identification and calculation of potential inefficiencies in a project, enabling corrections before physical implementation. Another significant advantage of CFD modelling is its ability to simulate extreme conditions and complex phenomena that would be expensive and difficult to test in real life. Real-world experiments would require high-cost equipment, such as specialized machinery, and extensive resources.

As already mentioned, cavitation is a complex and rapid phenomenon, and experimental setups to study require costly tools, including high-speed cameras, high-speed video equipment, special light sources, light analysers, and, in addition, the hydraulic installation of the experiment [1] [14]. For these reasons, CFD models are widely used in the study of cavitation. Given the importance of CFD, many authors have explored its methods, equations, and applications, analysing both fundamental and advanced aspects of this approach [38], [39], [40], [41].

5.1 CFD modelization procedure

All commercial CFD software differs from each other containing different interfaces, parameters or result analyser. However, they all have the same workflow, constituted by pre-processor, solver and post processor [38].

5.1.1 Pre-processor

The pre-processing step consists in the definition of the input properties for a flow problem, and the sequent transformation of these properties into a form suitable for the solver. Here the user needs to:

- Build the geometry of the flow problem, defining the computational domain.
- Perform the grid generation, subdividing the domain is smaller sub-domains called cells or control volumes.
- Define the flow phenomena that needs to be modelled.
- Define the fluid properties.
- Specify the initial conditions at the borders of the main domain.

The solution of the problem (pressure, velocity, viscosity temperature etc) is defined inside each cell. The accuracy of the numerical simulation is dependent on the number of cells in the domain. In general, a finer mesh increases the solution accuracy but at the same time increases also the computational effort and time. The correlation between computational time and number of cells is dependent on many factors regarding the flow problem and the method of resolutions. In general, the correlation is at least linear but, in many cases, this can also be quadratic [42]. Creation of an optimized mesh is not straightforward. Unform dimension of mesh elements all over the domain is often not very convenient, instead a higher cell concentration is adopted in the region where higher precision is required. Lower concentration is adopted where less precision of the solution is needed, reducing computational effort and solution time.

5.1.2 Solver

In the Ansys fluent solver a finite volume method, is used. In this numerical algorithm the sequent steps occur:

- Integration of the governing flow equation in all the cells of the domain.
- Conversion of the results from the integrations into algebraic equations.
- Resolution of the algebraic equations.

Operating with this method, the conservation of a general flow property within a control volume can be defined as a balance between the processes that tend to increase it and those that tend to decrease it. In other terms, this can be expressed as:

$$\begin{matrix} Rate\ of \\ change \\ with\ respect \\ of\ time \end{matrix} = \begin{matrix} Net\ rate\ of \\ increase \\ due\ to \\ convection \end{matrix} + \begin{matrix} Net\ rate\ of \\ increase \\ due\ to \\ diffuson \end{matrix} + \begin{matrix} Net\ rate\ of \\ creation \end{matrix}$$

5.1.3 Post processor

This final step of the CFD numerical simulations, asses the results visualizations. In this final section, having completed the numerical resolution, the user can create surface plots, contour plots or vectors, see the streamlines of the flow and calculate the problem solution in different zones of the domain.

5.2 Governing equations

The governing equation that are solved in the CFD models are the equations expressing the conservation laws in physics [40]:

- Conservation of mass.
- Newton's second law: the change in the particle momentum, equals the sum of the forces applied in it.
- First law of thermodynamics: the change in the energy rate is the sum of the heat added and the work done by the fluid.

The fluid in these models is treated as a continuum, this means that the molecular motion of the particles is not counted.

5.2.1 Conservation of mass

For the mass conservation in the three dimensions the first step is to write the mass balance of a single volume control:

$$\begin{matrix} Rate\ of\ increase \\ of\ mass\ in\ a\ single\ cell \end{matrix} = \begin{matrix} Net\ rate\ of\ mass\ flow \\ into\ the\ single\ cell \end{matrix}$$

Next the mass flow rate across the boundary of the element is calculated, from the values of density, area and velocity at the boundary. The mass conservation equation in a compact form, for compressible fluid is expressed as:

$$\frac{\partial \rho}{\partial t} = \nabla(\rho \, \boldsymbol{u}) \tag{5.1}$$

ρ is the fluid density, t is the time instant, and $\boldsymbol{u}$ is the vector of velocities in the three dimensions.

5.2.2 Navier-stokes equations

The Navier Stokes equations are a set of partial differential equations describing the rate of change in momentum for a viscous flow motion. This are based on the Newton's second law:

$$\begin{matrix} Rate\ of\ increase \\ of\ momentum\ in\ a\ particle \end{matrix} = \begin{matrix} Sum\ of\ forces \\ in\ the\ particle \end{matrix}$$

Is possible to distinguish two types of forces that can be applied in a fluid particle:

- Surface forces: like pressure, viscous or gravity forces.
- Body forces: as for example the centrifugal electromagnetic and Coriolis forces.

The Navier Stokes equations for the three directions x, y and z are reported below.

$$\rho \frac{Du}{Dt} = -\frac{\partial p}{\partial x} + \nabla(\mu \nabla u) + S_{Mx} \tag{5.2}$$

$$\rho \frac{Dv}{Dt} = -\frac{\partial p}{\partial y} + \nabla(\mu \nabla v) + S_{My} \tag{5.3}$$

$$\rho \frac{Dw}{Dt} = -\frac{\partial p}{\partial z} + \nabla(\mu \nabla w) + S_{Mz} \tag{5.4}$$

In these formulas μ is the viscosity of the liquid and S_M is the generation of momentum. While u, v and w are the velocities with respect to x, y and z.

5.2.3 Energy equation

For compressible flow simulations, as the one performed in this thesis, the energy equation needs to be added. The energy equation derives from the first law of thermodynamics who states that:

$$\begin{matrix} Rate\ of\ increase \\ of\ wnergy\ in\ a\ particle \end{matrix} = \begin{matrix} Rate\ of\ heat \\ added\ to\ the\ fluid \end{matrix} + \begin{matrix} Rate\ of\ work \\ done\ on\ the\ fluid \end{matrix}$$

The energy equation for compressible flow is:

$$\rho \frac{Di}{Dt} = -p\nabla \boldsymbol{u} + \nabla(k\nabla T) + S_i + \phi \quad 5.5$$

In the energy formulation i is the internal energy, p is the local pressure, T is the temperature, S_i is the generated internal energy, while ϕ is the dissipation factor for viscous stresses.

5.2.4 Equation of state

Among the equations discussed earlier, the thermodynamic properties of the fluid are unknown variables. Relationships between these properties can be established by assuming thermodynamic equilibrium, requiring only two state variables. For example, in the case of an ideal gas, using density and temperature as state variables, the equations of state that need to be added to the set of equations are:

$$p = \rho\, R\, T \quad 5.6$$

$$i = C_v\, T \quad 5.7$$

C_v is the specific heat at constant volume, while R is the gas constant.

5.3 Turbulence

The Reynolds number is a dimensionless quantity representing the ratio between the inertial and viscous forces in the fluid. Experiments have shown that, below a specific threshold called the critical Reynolds number (Re_{crit}) the fluid motion remains smooth, with adjacent layers sliding past one another in an orderly manner as demonstrated in Fig. 5-1 [43]. This type of flow is called laminar.

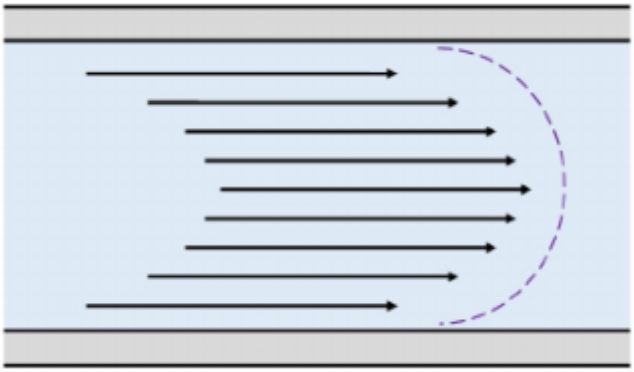

Figure 5-1: Schematic representation of laminar flow in a tube [43].

Instead at values higher than Re_{crit} inertial forces prevail over the viscous comporting an effective change in the fluid motion changing his motion from laminar flow to what is called turbulent flow. Its motion becomes highly unsteady with the appearance of vortices and fluctuations. The state values like velocity or pressure vary in a random and chaotic way, as is possible to see from Fig. 5-2.

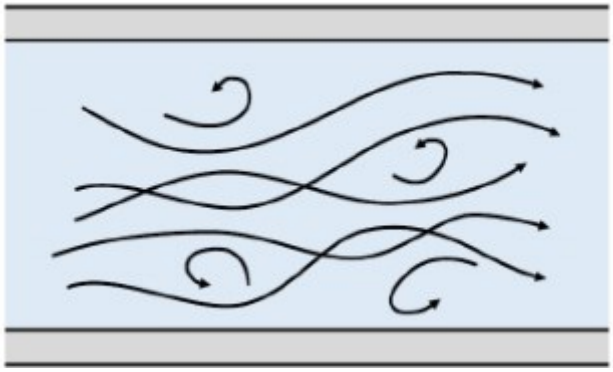

Figure 5-2: Schematic representation of turbulent flow in a tube [43].

Calculating precisely at every instant the velocity u in Fig 5-2, would require a really high cost in terms of computational effort, due to the chaotic and random variation of the turbulent flow. For this reason, the velocity is divided into a mean stationary value U and a fluctuant time dependent value $u'(t)$ superimpose to it.

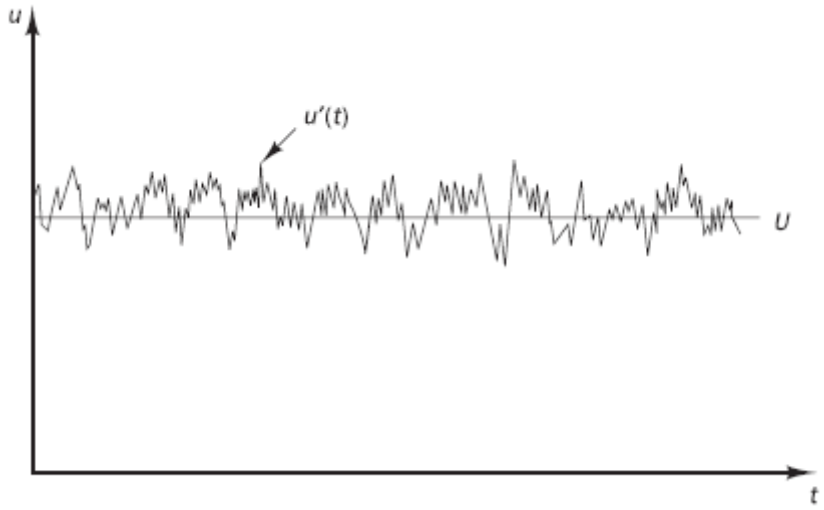

Figure 5-3: Typical point measurement of velocity in turbulent regime [38].

This method to represent turbulence is called Reynolds decompositions. Thanks to it, it is now possible to characterize a turbulent flow with its average value and a statistical property that represents the fluctuations around the average value. Solving the governing equations for the flow with a direct calculation, would require a huge amount of time and computational power. As this is not affordable, the Reynolds decompositions is used. In CFD field large amount of research effort is spent to build methods able to describe the behaviour and related phenomena of turbulence. The whole amount of models can be grouped in three different categories:

- Reynolds average Navier-Stokes (RANS): In these models, the focus are the mean values in the Reynolds decompositions and the effect of turbulence on them. Due to the interaction that occur between different fluctuations, additional terms appear in the averaged flow equations. Those models are the less precise between the three categories but in opposite are also the ones that need less computational power.
- Large eddy simulation (LES): within these models is possible to capture the behaviour of larger eddies. A space filtering prior to the computations is used, allowing the passage of larger eddies and denying it at the smaller ones.
- Direct Numerical Simulation (DNS): these models calculate apart from the mean flows also all the velocity fluctuations. These are the costliest methods regarding the computational power and clearly are also the most precise.

5.3.1 RANS governing equations

In most models adopted at industrial level available from the literature for the type of simulations targeted in this thesis, the turbulence methods applied belong to the Reynolds-Averaged Navier-Stokes (RANS) category. As previously discussed, these methods are based on the Reynolds decomposition of the state variables. This implies that the governing equations mentioned earlier will be modified, as averaged values are used to account for turbulence. Therefore, the governing equations in RANS turbulence models for compressible fluids are as follows:

$$\frac{\partial \bar{\rho}}{\partial t} = \nabla(\bar{\rho}\,\tilde{\boldsymbol{u}}) \tag{5.8}$$

$$\frac{\partial(\bar{\rho}\,\tilde{u})}{\partial t} + \nabla(\bar{\rho}\,\tilde{u}\,\tilde{\boldsymbol{u}}) = -\frac{\partial \bar{p}}{\partial x} + \nabla(\mu\nabla\tilde{u}) + \left[-\frac{\partial\overline{(\bar{\rho}u'^2)}}{\partial x} - \frac{\partial\overline{(\bar{\rho}u'v')}}{\partial y} - \frac{\partial\overline{(\bar{\rho}u'w')}}{\partial z}\right] + S_{Mx} \tag{5.9}$$

$$\frac{\partial(\bar{\rho}\,\tilde{v})}{\partial t} + \nabla(\bar{\rho}\,\tilde{v}\,\tilde{\boldsymbol{u}}) = -\frac{\partial \bar{p}}{\partial y} + \nabla(\mu\nabla\tilde{v}) + \left[-\frac{\partial\overline{(\bar{\rho}u'v')}}{\partial x} - \frac{\partial\overline{(\bar{\rho}v'^2)}}{\partial y} - \frac{\partial\overline{(\bar{\rho}v'w')}}{\partial z}\right] + S_{My} \tag{5.10}$$

$$\frac{\partial(\bar{\rho}\,\tilde{w})}{\partial t} + \nabla(\bar{\rho}\,\tilde{w}\,\tilde{\boldsymbol{u}}) = -\frac{\partial \bar{p}}{\partial z} + \nabla(\mu\nabla\tilde{w}) + \left[-\frac{\partial\overline{(\bar{\rho}u'w')}}{\partial x} - \frac{\partial\overline{(\bar{\rho}v'w')}}{\partial y} - \frac{\partial\overline{(\bar{\rho}w'^2)}}{\partial z}\right] + S_{Mz} \tag{5.11}$$

Equation 5.8 represents the mass conservation and from equations 5.9 to 5.11 there are the Reynolds averaged Navier Stokes equations. In these formulas the overline indicates a time-averaged variable while instead the variables with the tilde are indicating a density weighted average also called Favre-averaged variable. This type of averaging is used because turbulent fluctuations in compressible flow models lead to density fluctuations.

5.4 Turbulence models

The simpler turbulent models are the two equations methods. These models involve the addition of two transport equations to the set of governing RANS equations. These permit the calculation of the turbulent viscosity, an unknown in the governing RANS equations, and so allow the resolution of the flow problem [38], [40], [44].

5.4.1 k-ε model

In CFD analysis this model has become the basis of flow calculations. For heat transfer simulations and industrial flow, the k-ε has become one of the most used methods due to

its robustness, economy in terms of computational power and reasonable accuracy for turbulent flows. It is a semi-empirical model, based on empiricism and phenomenological considerations. It is based on the modelling of transport equations to account the turbulent kinetic energy and its dissipation rate. The transport equation for the kinetic energy derived from its exact equation, while instead the transport equations for its dissipation rate derived from physical reasoning and empirical assumptions. This method is based on two main assumptions:

- The flow is fully turbulent
- Effects of molecular viscosity are negligible

This imply that k-ε model can be used only for fully turbulent flow. In particular, it shows good accuracy in the free stream region, farther from the boundary of the domain. The two transport equations that need to be added are:

$$\frac{\partial(\rho \mathrm{k})}{\partial \mathrm{t}} + \frac{\partial(\rho \mathrm{k} u_\mathrm{i})}{\partial \mathrm{x_i}} = \frac{\partial}{\partial \mathrm{x}_j}\left[\left(\mu + -\frac{\mu_t}{\sigma_k}\right)\frac{\partial \mathrm{k}}{\partial \mathrm{x}_j}\right] + G_k + G_b - \rho\varepsilon - Y_M + S_k \tag{5.12}$$

$$\frac{\partial(\rho \varepsilon)}{\partial \mathrm{t}} + \frac{\partial(\rho \varepsilon u_\mathrm{i})}{\partial \mathrm{x_i}} = \frac{\partial}{\partial \mathrm{x}_j}\left[\left(\mu + -\frac{\mu_t}{\sigma_\varepsilon}\right)\frac{\partial \varepsilon}{\partial \mathrm{x}_j}\right] + C_{1\varepsilon}\frac{\varepsilon}{\mathrm{k}}\left(G_k + C_{3\varepsilon}G_b\right) - \frac{C_{2\varepsilon}\rho\varepsilon^2}{\mathrm{k}} + S_\varepsilon \tag{5.13}$$

In these partial differential equations G_b is the term that account for the turbulent kinetic energy due to buoyancy. G_k is the generation of turbulent kinetic energy due to mean velocity variation, while Y_M is the contribution of fluctuating dilatation in compressible turbulence to the overall dissipation rate. $C_{1\varepsilon}$, $C_{2\varepsilon}$, $C_{3\varepsilon}$ are constants, σ_ε and σ_ε are the turbulent Prandtl numbers and finally S_k and S_ε are user source dined terms. From these transport equations it is then possible to calculate the turbulent viscosity, necessary to solve the Reynolds averaged governing equations.

$$\mu_t = \rho C_\mu \frac{k^2}{\varepsilon} \tag{5.14}$$

Where C_μ is a constant [45].

5.4.2 k-ω model

In Ansys fluent, this method is based on the previous Wilkox model [46], that includes modifications for low Reynolds number, compressibility and shear flow spreading. This model can predict shear flow spreading rates that are in close agreement with

measurement for far wakes mixing layers plane round or radial jets and is also applicable for wall bounded flow. This indicates that this turbulence model is particularly indicated to solve the turbulence in near wall regions. It is an empirical model that calculates the transport equation for the turbulent kinetic energy and its specific dissipation rate which can be related to the variable ε with a simple formula.

$$\varepsilon = C_{\mu}\, k\, \omega \tag{5.15}$$

This model has been modified through the years with production terms in both transport equations which improved the accuracy in the prediction of free shear flows. The two transport equations are the following.

$$\frac{\partial(\rho \mathrm{k})}{\partial \mathrm{t}} + \frac{\partial(\rho \mathrm{k} u_{\mathrm{i}})}{\partial \mathrm{x}_{\mathrm{i}}} = \frac{\partial}{\partial \mathrm{x}_j}\left(\Gamma_k \frac{\partial \mathrm{k}}{\partial \mathrm{x}_j}\right) + G_k - Y_k + S_k \tag{5.16}$$

$$\frac{\partial(\rho \omega)}{\partial \mathrm{t}} + \frac{\partial(\rho \omega u_{\mathrm{i}})}{\partial \mathrm{x}_{\mathrm{i}}} = \frac{\partial}{\partial \mathrm{x}_j}\left(\Gamma_\omega \frac{\partial \omega}{\partial \mathrm{x}_j}\right) + G_\omega - Y_\omega + S_\omega \tag{5.17}$$

In these partial differential equations, G_ω represents the generation of omega while G_k is the generation of turbulent kinetic energy due to mean velocity variation. Γ_ω and Γ_k are the effective diffusivity of the turbulent kinetic energy and its dissipation rate, while $Y_k$and Y_ω are the dissipation of the two coefficients due to turbulence. Finally, S_k and S_ω are user source defined terms. The effective diffusivities are calculated as follows:

$$\Gamma_k = \mu + \frac{\mu_t}{\sigma_k} \tag{5.18}$$

$$\Gamma_\omega = \mu + \frac{\mu_t}{\sigma_\omega} \tag{5.19}$$

Where σ_k and σ_ω are the turbulent Prandtl numbers for k and ω. Turbulent viscosity is then calculated.

$$\mu_t = \alpha^* \frac{\rho k}{\omega} \tag{5.20}$$

The coefficient α^* damps the turbulent viscosity, causing a low Reynolds number correction. The value of this variable varies between zero and one, basing on the Reynolds number. In particular, for high Reynolds number $\alpha^*$is equal to one [47].

5.4.3 k-ω SST

Until now two different models have been presented: one is precise for near wall regions (k-ω) and the other instead works good for free stream regions. The basic idea of the shear

stress transport (SST) k-ω model is to combine the two models taking advantage of their precision in two different zones of the domain; in this way the model is able to work as a k-ω model in the near wall regions and as a k-ε in the free stream. To realize this model starting from the k-ω method, few refinements are added:

The two different models are combined using a blending function. This is designed to have a value of one in the "near wall region" activating the k-ω model, and a value of zero away from the surface that activate the k-ε model. In Fig. 5-4 is illustrated the value of the blending function called $F1$, with respect to the vicinity of the wall.

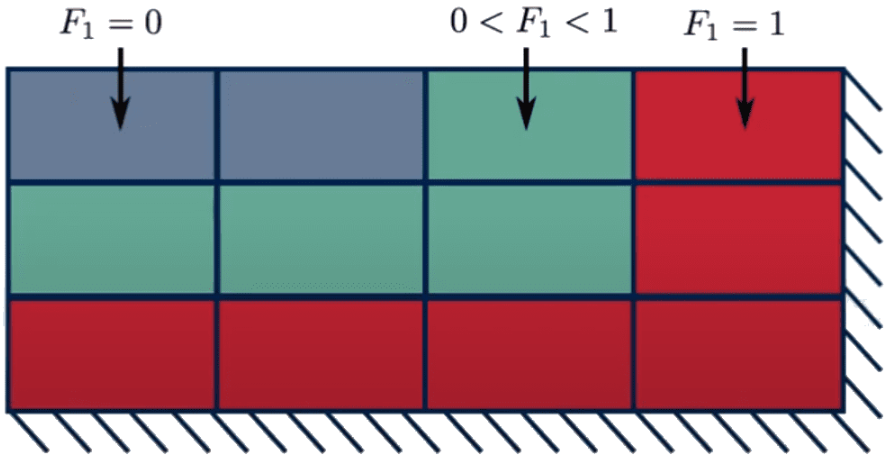

Figure 5-4: Values of the blending function depending on its distance to the wall [44].

- A damped cross-diffusion derivative term is present on the w equation.
- Turbulent viscosity formula is modified to account for the transport of the turbulent shear stress.
- The model constants are different.

Using this method is possible to have more accurate and reliable solution in a wider class of flows than the standard k-ω and k-ε. The transport functions of the SST k-ω model have a similar form to the standard kw model.

$$\frac{\partial(\rho k)}{\partial t} + \frac{\partial(\rho k u_i)}{\partial x_i} = \frac{\partial}{\partial x_j}\left(\Gamma_k \frac{\partial k}{\partial x_j}\right) + \widetilde{G_k} - Y_k + S_k \qquad 5.21$$

$$\frac{\partial(\rho \omega)}{\partial t} + \frac{\partial(\rho \omega u_i)}{\partial x_i} = \frac{\partial}{\partial x_j}\left(\Gamma_\omega \frac{\partial \omega}{\partial x_j}\right) + G_\omega - Y_\omega + D_\omega + S_\omega \qquad 5.22$$

In the equation 5.21, $\widetilde{G_k}$ represents the generation of turbulent kinetic energy due to mean velocity gradients, G_ω is the generation of ω. As in the standard k ω model, Γ_k and Γ_ω are the effective diffusivity ok k and w while Y_k and Y_ω are their dissipation due to turbulence. S_k and S_ω are user source defined terms and finally D_ω is the cross-diffusion term. The effective diffusivity factors are calculated as in the standard kω model, while instead the turbulent viscosity now is calculated as follow.

$$\mu_t = \frac{\rho k}{\omega} \frac{1}{\max\left[\frac{1}{\alpha^*}, \frac{SF_2}{\omega a_1}\right]} \tag{5.23}$$

Where S is the strain rate magnitude, α^* damps the turbulent viscosity, causing a low Reynolds number correction. For high Reynolds number $\alpha^*$is equal to one, while instead decrease around zero for low Reynolds number. The blending functions F_1 and F_2 are calculated as:

$$F_1 = \tanh\left(\Phi_1^4\right) \tag{5.24}$$

$$F_2 = \tanh\left(\Phi_2^2\right) \tag{5.25}$$

$$\Phi_1 = \min\left[\max\left(\frac{\sqrt{k}}{0{,}09\omega y}, \frac{500\mu}{\rho y^2 \omega}\right), \frac{4\rho k}{\sigma_{\omega,2}\, D_\omega^+ y^2}\right] \tag{5.26}$$

$$\Phi_2 = \max\left[2\frac{\sqrt{k}}{0{,}09\omega y}, \frac{500\mu}{\rho y^2 \omega}\right] \tag{5.27}$$

$$D_\omega^+ = \max\left[2\rho \frac{1}{\sigma_{\omega,2}} \frac{1}{\omega} \frac{\partial k}{\partial x_j} \frac{\partial \omega}{\partial x_j}, 10^{-10}\right] \tag{5.28}$$

Where, y is the distance to the nearest surface and D_ω^+ is the positive portion of the cross-diffusion term. Finally in this model, the cross-diffusion term of equation 5.22 to calculate the omega transport equation is calculated as [48]:

$$D_\omega = 2(1 - F_1)\rho\sigma_{\omega,2} \frac{1}{\omega} \frac{\partial k}{\partial x_j} \frac{\partial \omega}{\partial x_j} \tag{5.29}$$

5.4.4 Dimensionless number Y+

Talking about turbulence models in a CFD model one of the most important parameters is the dimensionless number Y^+. As represented in Fig. 5-5, starting from the average free stream velocity of the turbulent flow, as the flow get close to the wall boundary, the velocity reduces until it reaches a value of zero exactly at the wall [49].

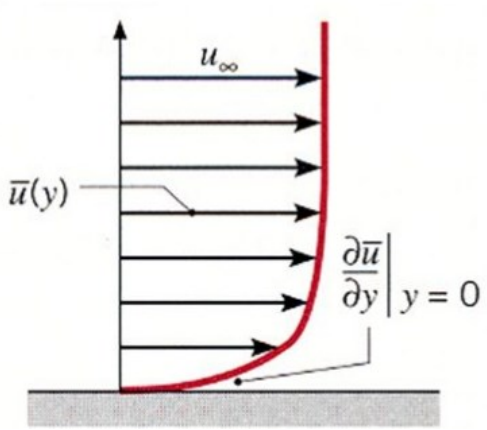

Figure 5-5: Turbulent flow average velocity variation near the wall [49].

As the velocity decreases, the inertial forces, which are predominant in turbulent flow, also become less significant. Near the wall, a thin layer forms, known as the boundary layer, where viscous forces dominate over inertial forces. Accurately modelling this layer is fundamental for a successful CFD simulation, as it helps predict fluid behaviour near the wall. To characterize this region, two dimensionless numbers are used: Y^+ and u^+. Y^+ can be interpreted as the local Reynolds number, which depends on local viscous and inertial forces. Instead u^+ is a dimensionless velocity, relating the local velocity to the frictional one. In wall-bounded flow, they are calculated as follows [50]:

$$Y^+ = \frac{\rho u_t y}{\mu} \tag{5.30}$$

$$u_t = \sqrt{\frac{\tau_w}{\rho}} \tag{5.31}$$

$$u^+ = \frac{u}{u_t} \tag{5.32}$$

Where u_t is the friction velocity y is the distance from the wall and τ_w is the wall shear stress. Depending on the flow conditions and on the distance taken as reference is possible

to identify three different ranges for the Y^+ parameter that can be used for different purposes: the viscous sub-layer, the buffer layer and the logarithmic law layer.

- Viscous sub layer $(Y^+ < 5)$: this region is characterized by a small reference distance *y* from the wall. Here the viscous forces dominate over the inertial one and it is assumed that the shear stress is equal to the wall shear stress τ_w. Due to those assumptions, it is possible to conclude, thanks to the definition of the dimensionless parameters, that $u^+ = Y^+$.
- Logarithmic law layer $(30 < Y^+ < 300)$: here both viscous but also inertial forces due to the turbulent regime are important. In this region there is anyway a logarithmic relation between the two parameters:

$$u^+ = \frac{1}{k}\ln(Y^+) + B \tag{5.33}$$

  In this correlation k is the Von Karman's constant while B is an empirical variable, that usually have a value of 5.5.
- Buffer layer $(5 < Y^+ < 30)$: this zone is characterized by a value of the Y^+ in between the viscous and logarithmic zone. Calculate the flow velocity in this zone is difficult as here both viscous and inertial forces are present and important without that one prevail over the other.

In Fig. 5-6, the correlation between the two parameters is showed. The black dotted lines are representing the constant and logarithmic correlation between the dimensionless parameters, while instead the red line in the plot represents the real flow values. It is possible to note how the real values follow the two black lines apart from the buffer layer zone. An additional zone in the figure can be distinguished: the defect layer. Here the distance from the wall is large and the logarithmic law do not follow the real values [51].

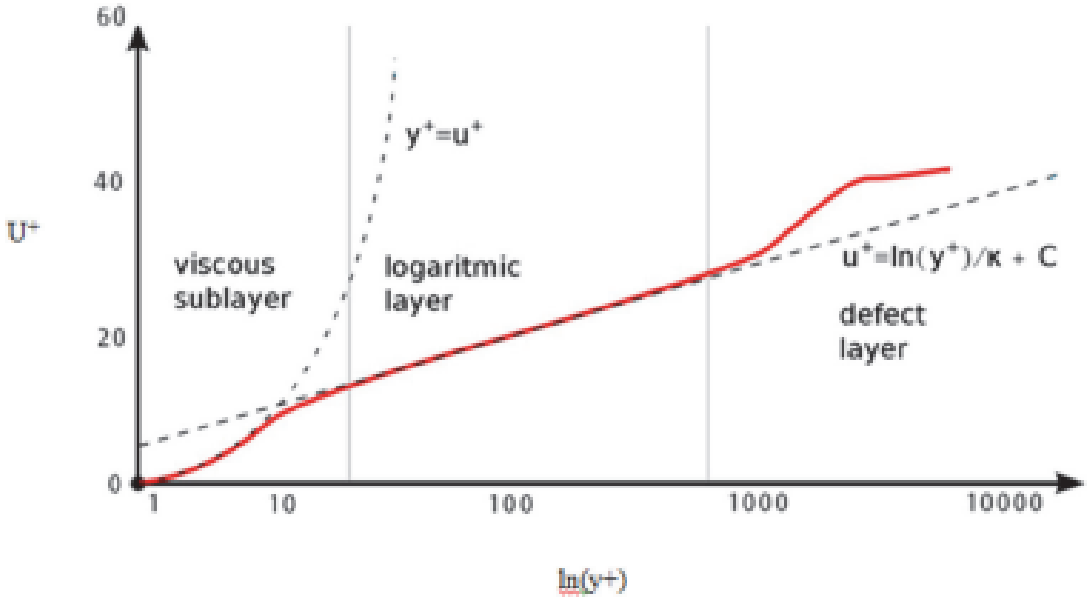

Figure 5-6: correlation between the two dimensionless parameters $Y^+$and u^+ [51].

In the ambient of the CFD modelling the reference distance is the centroid of the first cell adjacent to the wall. So, with the same flow conditions depending on the mesh the Ansys software will solve the equations in the near wall region in two different methods:

- With a finer mesh near the wall the value of Y^+ is in the viscous sub layer range. In this case the software solves the equations for each cell in the same way of the whole domain. Clearly a finer mesh requires also a higher computational effort and time of resolution.
- If instead the mesh is coarser, the Y^+ is in the logarithmic layer. In this case the software cannot solve the usual equations as the velocity gradient inside the cell are too elevated. In this case to solve the flow the software uses the wall functions. These are able to approximate the velocity flow near the wall thanks to a semi-empirical approach.

The buffer layer region instead is a zone that is generally unwanted. In fact, here the software uses a sort of interpolation between the two solving methods using some empirical translation functions, which cannot predict in a good way the flow.

5.5 Cavitation model

The introductory section of this chapter discusses the importance of studying cavitation through CFD models. As previously mentioned, cavitation is a complex phenomenon that occurs within milliseconds or microseconds and is influenced by key flow properties such as temperature, pressure, and velocity, which govern the overall flow. Additionally, the transport and evolution of the cavity within the liquid are closely linked to flow turbulence, making it essential to incorporate a turbulence model in the analysis. The challenge, however, lies in the fact that commonly used turbulence models were originally developed for single-phase flows, making their application to a two-phase phenomenon like cavitation problematic. Thus, it is necessary to develop a cavitation model capable of working with a turbulence model, with the aim of describing the formation, growth, motion, shape, and collapse of cavitation bubbles. In the work by Folden [52], various cavitation models are grouped and categorized based on the methodologies and physical models used in their development. One common and widely used category of models is the homogeneous mixture model. In this approach, the primary assumption is that the two phases are in mechanical and thermal equilibrium, sharing the same flow properties, with fluid characteristics such as density and viscosity treated as local properties of the single fluid. Specifically, in the mixture model, density and viscosity depend on the vapor volume fraction α_v.

$$\rho_m = \rho_v \alpha_v + (1 - \alpha_v)\rho_l \tag{5.34}$$

$$\mu_m = \mu_v \alpha_v + (1 - \alpha_v)\mu_l \tag{5.35}$$

Here, the letter *m* indicates the mixture property, while *l* and *v* represent the liquid and vapor phases, respectively. In this approach, the volume fraction serves as an approximation of the vapor distribution within the domain. When using this type of models, these two equations are combined with the Navier-Stokes equations to describe the flow within the domain. The limitations of this approach are illustrated in Fig. 5-7.

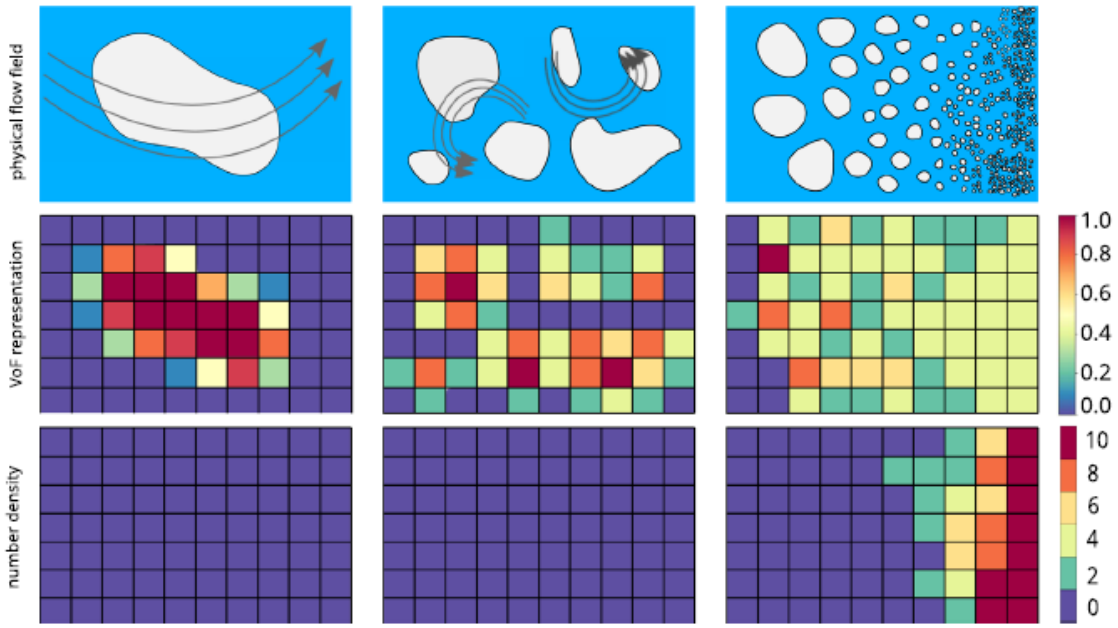

Figure 5-7: First row: real representation of a vapour cloud formation. Second row: representation of the real flow with a volume fraction method. Third row: concentration of bubbles in the real flow [52].

Good discretization of the domain is crucial to accurately describe the phenomena. In the figure, the first row of images represents a real flow with the formation of a vapor cloud from a large cavity, while the second row shows the representation based on the volume fraction within domain cells. It is evident that, in the first image, while there is only a single large vapor cavity, the model can effectively represent the actual flow. However, as the bubble changes into a vapor cloud, the model struggles to accurately depict the true distribution of bubbles. The cavities become indistinguishable, and each cell is averaged with a mean vapor fraction value. In the bottom row, a potential improvement is illustrated, where the number of bubbles per control volume is calculated. This approach can be incorporated into the classic method to account for vapor cavities smaller than a cell. In homogeneous mixture models, one of the most widely used approaches is to apply a transport equation to model the evolution of the liquid and vapor volume fractions.

$$\frac{\partial \rho_i \, \alpha_i}{\partial \mathrm{t}} + \nabla(\rho_i \, \alpha_i \, \boldsymbol{u}) = \dot{m}_\iota \qquad 5.36$$

Where $\dot{m}_\iota$ is the volume fraction source term that can be for the vapour or liquid phase, while $\boldsymbol{u}$ is the velocity vector. The source term gives an explicit rate for the phase transition, indicating if the vapour is condensing or evaporating. Is then possible to divide

this term in two distinct factors representing the two different phenomena of condensation, and evaporation. At any time just one of these two terms is active in every control volume basing on the relationship between the split source term and the pressure. When the pressure falls below the saturation value, the evaporation takes places, while instead in the opposite case the condensation process occurs.

$$\dot{m} = \begin{matrix} \dot{m}^+ , p > p_v \\ \dot{m}^- , p > p_v \end{matrix} \quad 5.37$$

The difficulty now is to develop a good expression for the source term. The most used approach is to assume that inside each cell of the domain the vapour volume fraction is equal to the amount of volume occupied by vapour cavities that form. Then depending on the dynamic conditions, they grow and finally as the pressure rises higher than the saturation one, they collapse. The growth and collapse of the cavitated nuclei is modelled using the Rayleigh Plesset equation.

$$R\,\frac{d^2R}{dt^2} + \frac{3}{2}\left(\frac{dR}{dt}\right)^2 = \frac{p_b(t) - p_\infty(t)}{\rho_l} - \frac{4\mu_l}{\rho_l R}\,\frac{dR}{dt} - \frac{2\sigma}{\rho_l R} \quad 5.38$$

This equation describes the evolution in time of the bubble radius R, with an internal pressure p_b under the influence of a reference one p_∞, the surface tension σ and the liquid viscosity. The fully Plesset equation is not commonly used as in general various terms like the surface tension, or the inertial effects can be neglected to facilitate the numerical resolution. Using the Ansys Fluent solver for the cavitation process inside a venturi, in literature there are two main models that are commonly used: the Schnerr-Sauer and the Zwart-Gerber-Belamri (ZGB). Both models account for all these effects: phase change, bubble dynamics, turbulent pressure fluctuations, and non-condensable gases.

5.5.1 Schnerr-Sauer model

The vapour mass source term used in this method is:

$$m = \frac{\rho_v \rho_l}{\rho_m}\,\frac{d\alpha_v}{dt} \quad 5.39$$

And the equation for the vapour volume fraction has a general form:

$$\frac{\partial(\rho_v \alpha_v)}{\partial \mathrm{t}} + \nabla(\rho_v \alpha_v\, \boldsymbol{u}) = m \quad 5.40$$

In their method, Schnerr and Sauer connected the vapour volume fraction to the number of bubbles per volume of liquid n_b:

$$\alpha_v = \frac{n_b \frac{4}{3} piR^3}{1 + n_b \frac{4}{3} piR^3} \tag{5.41}$$

Then it is possible to derive the equation for the mass source term.

$$m = \frac{\rho_v \rho_l}{\rho_m} \alpha_v (1 - \alpha_v) \frac{3}{R} \sqrt{\frac{2}{3} \frac{(p_v - p)}{\rho_l}} \tag{5.42}$$

$$R = \left(\frac{\alpha_v}{(1 - \alpha_v)} \frac{3}{4pin_b} \right)^{\frac{1}{3}} \tag{5.43}$$

It is interesting to note that in this method the mass transfer equation is proportional to $\alpha_v(1 - \alpha_v)$, the product between the vapor and liquid volume fraction. This mean that the equation is equal to zero when α_v reaches value of one or zero, instead its maximum is reached in between these two values. In this model the only parameter which must be determined by the user is the number of bubbles per volume of liquid n_b. The equation of the mass source term can be used to model the condensation and evaporation processes. Its final form is [53], [54]:

$$p < p_v \quad , \quad m_{evap} = \frac{\rho_v \rho_l}{\rho_m} \alpha_v (1 - \alpha_v) \frac{3}{R} \sqrt{\frac{2}{3} \frac{(p - p_v)}{\rho_l}} \tag{5.44}$$

$$p > p_v \quad , \quad m_{cond} = \frac{\rho_v \rho_l}{\rho_m} \alpha_v (1 - \alpha_v) \frac{3}{R} \sqrt{\frac{2}{3} \frac{(p - p_v)}{\rho_l}} \tag{5.45}$$

5.5.2 Zwart-Gerber-Belamri (ZGB) model

Assuming that in the flow all the bubbles have the same size, Zwart-Gerber-Belamri proposed that the mass transfer rate per unit volume is obtained using the bubble density numbers n and the mass change rate of a single bubble.

$$m = n \left(4piR^2 \rho_v \frac{dR}{dt} \right) \tag{5.46}$$

The volume fraction is related to n following the following formula:

$$\alpha_v = n\left(\frac{4}{3}piR^3\right) \tag{5.47}$$

And so is now possible to substitute n with the volume fraction in the previous formula.

$$m = \frac{3\alpha_v\rho_v}{R}\sqrt{\frac{2}{3}\frac{(p_b - p)}{\rho_l}} \tag{5.48}$$

This equation is obtained for the evaporation process, to apply it also to the condensation a generalized formula is used:

$$m = F\frac{3\alpha_v\rho_v}{R}\sqrt{\frac{2}{3}\frac{|p_b - p|}{\rho_l}sign(p_b - p)} \tag{5.49}$$

Where F is an empirical coefficient used for the calibration of the equation. But now this equation works only for the condensation process and not for the evaporation one, this because in this case is assumed that cavitated bubbles do not interact between each other. This clearly can be true only for the inception of the cavitation nuclei, but then as the volume fraction increases the nucleation site density must decrease accordingly. To account to this phenomenon, in this model the term α_v is replaced by $\alpha_{nuc}(1 - \alpha_v)$ in the equation. The complete form of the mass transfer function in this model is:

$$p < p_v \ , \ m_{evap} = F_{vap}\frac{3\alpha_{nuc}(1 - \alpha_v)\rho_v}{R}\sqrt{\frac{2}{3}\frac{p_v - p}{\rho_l}} \tag{5.50}$$

$$p > p_v \ , \ m_{cond} = F_{cond}\frac{3\alpha_v\rho_v}{R}\sqrt{\frac{2}{3}\frac{p - p_v}{\rho_l}} \tag{5.51}$$

Where α_{nuc} is the nucleation site volume fraction, and F_{vap}, F_{cond} are respectively the evaporation and condensation coefficients [53].

6 Construction of the model

The simulations performed in this thesis are based on the previous works of Jahangir [1] and Maxwell [2]. In Fig. 6-1 the experimental set-up used by Jahangir [1] for the experiment is shown.

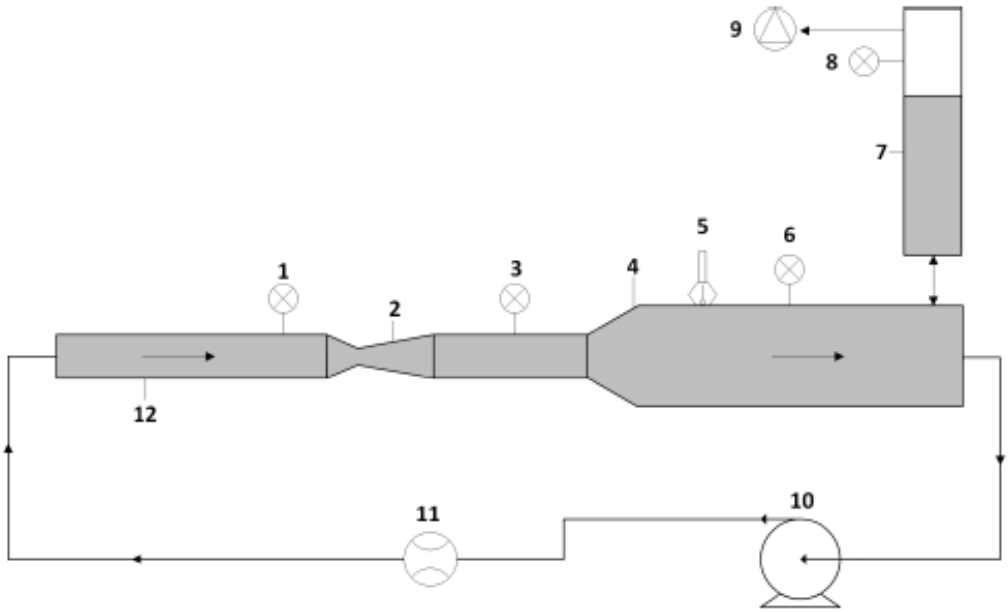

Figure 6-1: Schematic representation of the experimental set-up used in [1].

In this schematic view of the setup, the various components of the system are identified with different numbers. Numbers 1, 3, 6, and 8 represent pressure transducers, which are used to measure local pressure. Number 10 indicates the centrifugal pump, while number 11 represents the magnetic flowmeter used to measure the inlet mass flow rate. Numbers 12 and 4 correspond to the inlet and outlet pipes, respectively. Number 7 denotes a water column equipped with a vacuum pump, indicated by number 9, which is used to regulate the system's pressure. Number 5 is the temperature sensor, and finally, number 2 is the venturi tube.

In this thesis, the same venturi tube geometry is employed, and a figure illustrating the geometrical parameters is provided below in Fig. 6-2. Following previous studies, the divergent angle of 16° is chosen to avoid flow separation while maintaining a rapid pressure recovery.

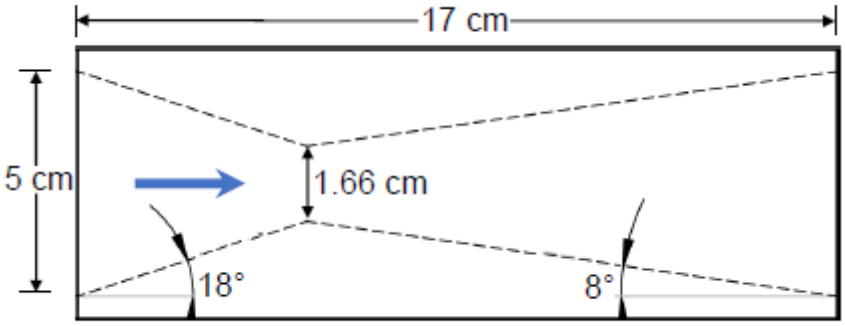

Figure 6-2: Geometrical properties of the venturi tube [1].

6.1 Fluid properties

The fluid properties are determined based on the experimental work of Jahangir [1]. In this study, the temperature ranges between 15°C and 25°C, so a mean value of 20°C is used to calculate the other parameters. Values for the fluids properties at 20°C are obtained from steam tables and previous studies [2], [55], [56]. Tables 6-1 and 6-2 presents all property values of the two fluids.

Water properties		
	Values	Unit
Density $\boldsymbol{\rho_l}$	998,2	kg/m^3
Viscosity μ_l	$1{,}003 * 10^{-3}$	$kg/m\,s$
Temperature $\boldsymbol{T}$	298,15	K
Sat.pressure $\boldsymbol{P_{sat}}$	2338	Pa

Table 6-1: Water properties.

Vapour properties		
	Values	Unit
Density $\boldsymbol{\rho_v}$	0,0173	kg/m^3
Viscosity μ_v	$1{,}34 * 10^{-5}$	$kg/m\ s$
Temperature $\boldsymbol{T}$	298,15	K
Poisson coeff. $\boldsymbol{\gamma}$	1,33	….

Table 6-2: Vapour properties.

6.2 Ansys Fluent geometry

With the tube dimensions established, the first step in the CFD procedure is to create the geometry in the Ansys workbench, using the software's "Design Modeler" tool. Rather than modelling the entire tube, only a radial section is designed. Since the tube has symmetrical geometry, it is possible to simulate the cavitation process in just one section, as the other sections will behave identically. This simplification reduces the complexity of the geometry and, consequently, the problem itself. Additionally, this approach saves a significant number of cells during the meshing process due to the reduced geometry. Fewer control volumes mean that the computational effort is reduced and so the user will save a large amount of time. Although this method is not perfectly precise, it is widely used in the literature, and results have been shown to be reliable. Fig. 6-3 shows the geometry constructed in Ansys Design Modeler.

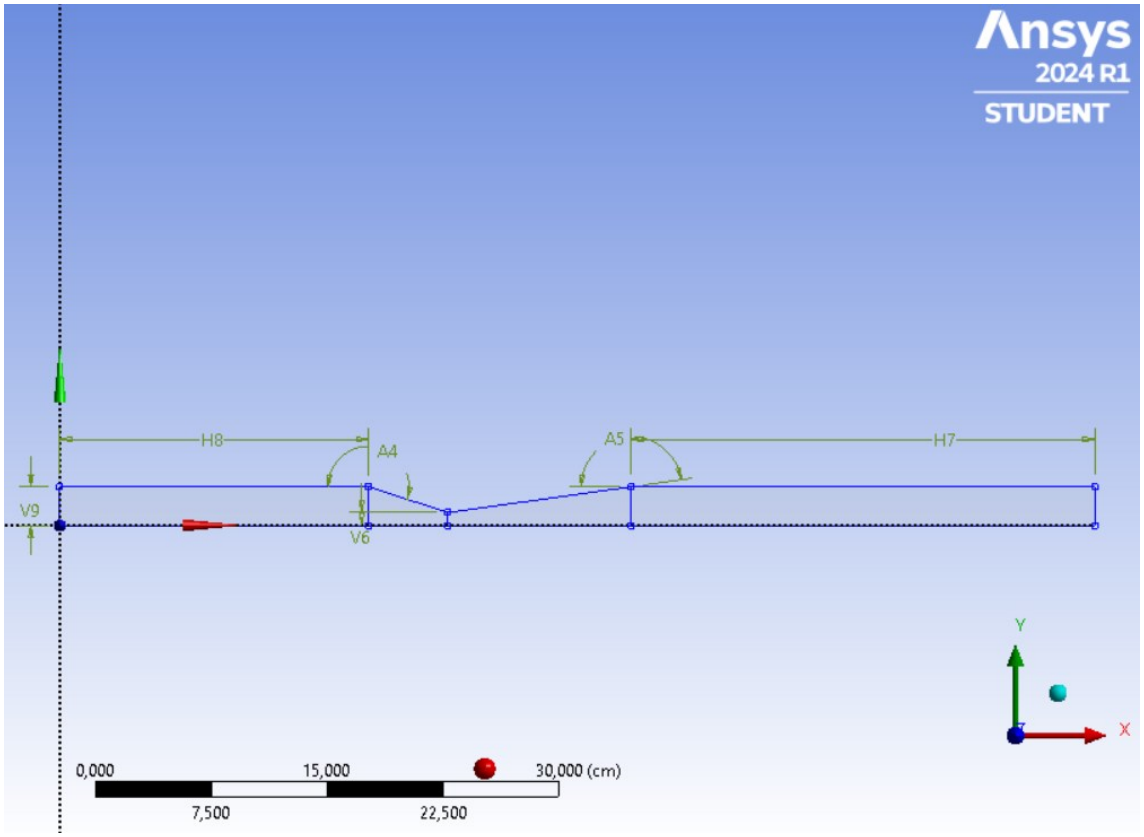

Figure 6-3: Geometric construction in the Ansys Fluent software.

Table 6-3 shows the values of the dimensional variables illustrated in Fig. 6-3.

Type	Name	Value	Units
Horizontal line	H8	20 cm	cm
	H7	30 cm	cm
Vertical line	V9	2,5 cm	cm
	V6	0,83 cm	cm
Angle	A4	198	°
	A5	172	°

Table 6-3: Geometrical properties of the venturi tube.

The geometry is then divided into four distinct sections to facilitate the sequent meshing process. In Fig. 6-4, the different sections are illustrated. Moving from left to right, these sections are: the inlet tube (highlighted in green), the convergent section, the divergent section (highlighted in green), and finally the outlet tube.

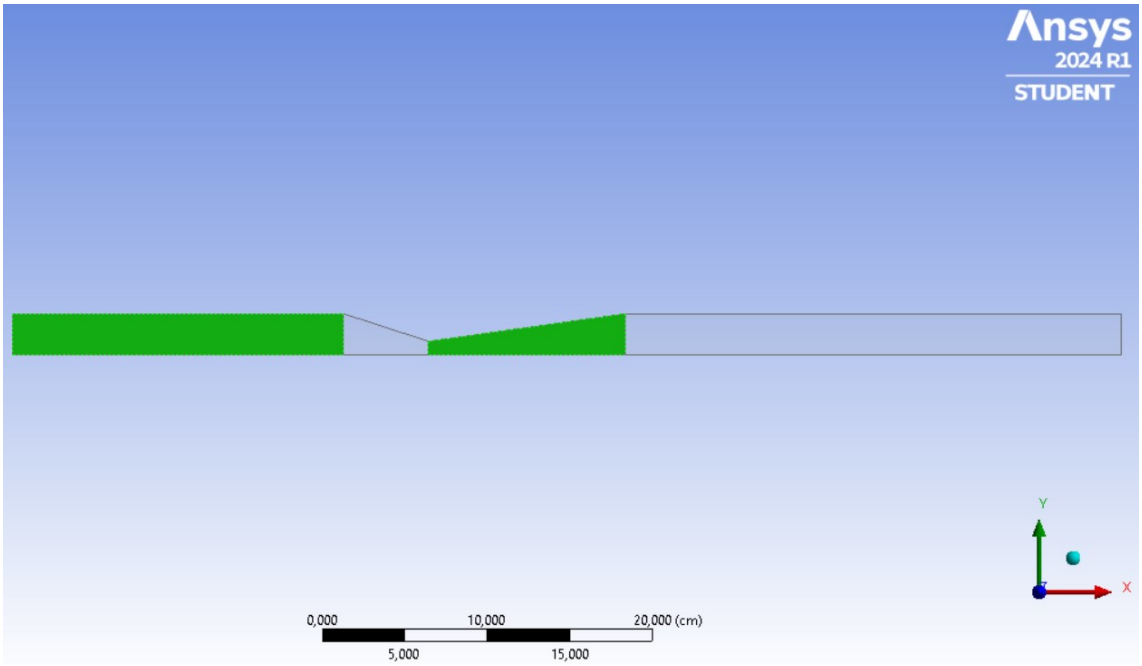

Figure 6-4: Illustration of the four different sections in the geometry.

The inlet and outlet tubes measure 20 cm and 30 cm, respectively. The inlet section is added to ensure that by the time the flow reaches the inlet of the venturi, the flow profile is fully developed. The outlet section, on the other hand, allows for pressure recovery in the tube. In particular, as vapor cavities diffuse in the outlet section of the tube, specific conditions like high pressures or other disturbances can occur at the venturi outlet. Adding an outlet section stabilizes the solution and allows these disturbances to progressively dissipate, far from the domain boundary.

6.3 Meshing process

After the generation of the domain, it is now possible to build the mesh in it. The aim of the mesh is to divide the domain in other small control volume called cells or control volumes. The solver will solve the governing equations for each of them. The construction of the mesh is a fundamental process for the construction of a CFD model. A mesh with a low number of cells with respect to a mesh with a higher number, may not capture the right flow values, averaging them, or some physical phenomenon, as in the cavitation process, the small bubble formation or concentration. So clearly a high number of cells gives a more precise solution, but on the other hand treating more cells means that the

solver will solve the governing equations a higher number of times and so the computational effort increases. From this statement is clear that in the construction of the mesh a compromise between these two aspects is the best solution. There are two main approaches for the mesh structure creation in CFD practice:

- Structured: a structured mesh is composed by a grid of squares or rectangles when operating in a 2D domain or parallelepipeds in a 3D domain. This means that for a 2D domain a structured mesh can be defined by two indices. Those meshes are particularly effective for the solving process as the neighbour point of each cell can be found by the increment of the indices. Therefore they require less computational effort for the numerical resolution. The main disadvantage of the structured mesh is that are difficult to implement for complicated geometries. A representation of a structured mesh is illustrated in Fig. 6-5.
- Unstructured: in this meshes the domain is not organized in a grid. The cells are triangular for 2D and tetrahedral for 3D domain, and the cells may have unique connection between neighbours' cells. This complicates the resolution of the governing equations in the cells. The main advantage for this type of mesh is that they adapt well to curved or complicated geometries. A representation of a structured mesh is illustrated in Fig. 6-5.

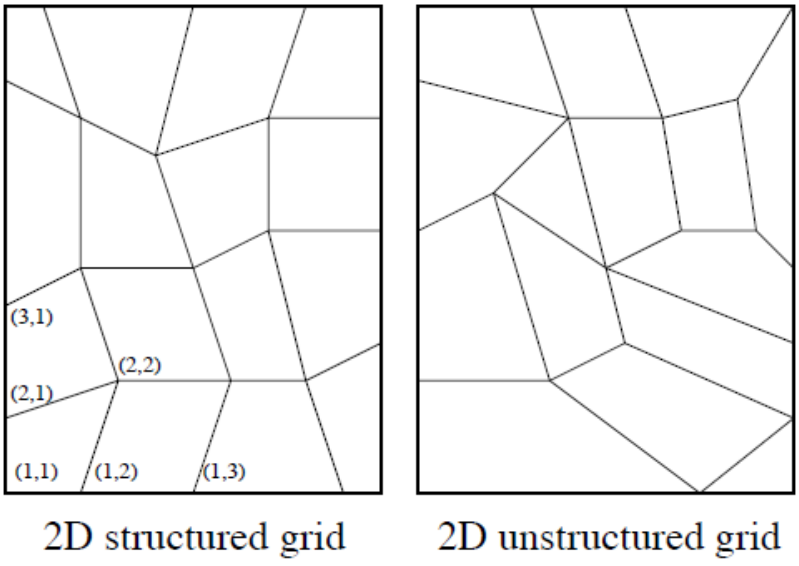

Figure 6-5: Example of a 2D structured and unstructured grid [57].

6.3.1 Mesh quality

In the mesh construction there are some parameters that can describe the quality of the mesh [58], [59], [60]. Ideally the best 2D mesh would be composed just by squares each equal and orthogonal between each other. Clearly this is the optimal solution and for example in the venturi tube geometry this is not possible. But the quality of the mesh indicates how far the mesh is from that ideal condition. Meshes with a good quality help to get a more stable solution reducing the possibility of errors in the numerical resolution and can also simplify the calculation of the flow problem, reducing the computational time. The main parameters to calculate the quality of the mesh are:

- Aspect ratio: This parameter is the ratio between the longest length side to the shortest one. Its minimum value is one and clearly the lower it is the closer the cell is to the ideal condition. In Fig. 6-6, the aspect ratio values of two different cells are showed. Clearly, the higher the aspect ratio the farther the cell is to its ideal condition.

Figure 6-6: Aspect ratio of two different cells [60].

- Skewness: it relates the distance between the two centroids of adjacent cells $\vec{d}$ with the distance from that line to the shared side centre $\vec{m}$. It is calculated as follow:

$$skewness = \frac{|\vec{m}|}{|\vec{d}|} \tag{6.1}$$

Its value can range from 0 to infinite, but too skewed cells are not preferred. In Fig. 6-7, an illustration explaining the parameter is showed.

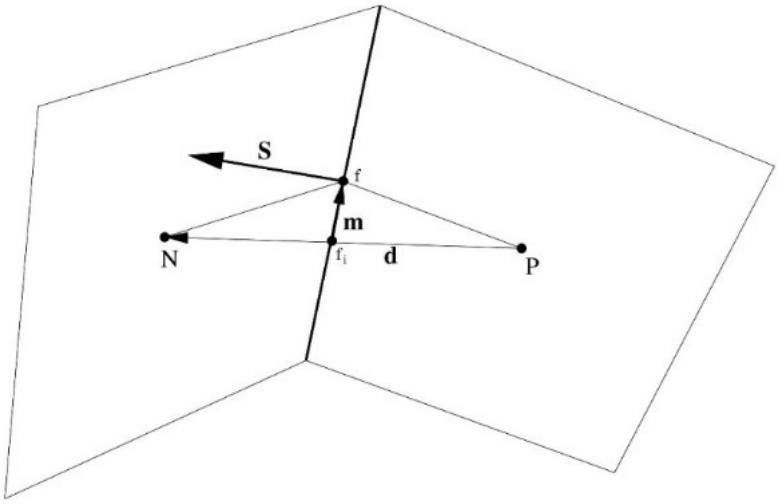

Figure 6-7: Illustration of the skewness parameter [59].

- Orthogonality: this parameter represents the angle, α_N, between the line connecting two centroids of adjacent cells, d, and the normal of the side shared between them S. The close this parameter is to zero the closer the cells are to the ideal condition of orthogonal cells. If this parameter is too high could cause numerical instability. In Fig. 6-8, an illustration of the parameter is showed.

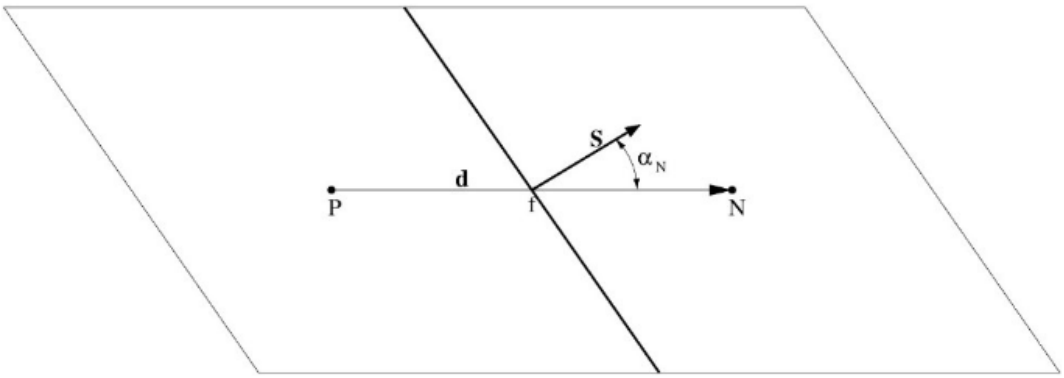

Figure 6-8: illustration of the orthogonality parameter [59].

6.3.2 Mesh constructions

The venturi tube is considered a simple geometry since there are no curved lines in a radial section of the tube. Therefore, the Ansys Meshing tool, is used to create a structured mesh in the previously constructed domain. The goal in mesh construction is to allocate cells efficiently, using fewer cells where high precision is unnecessary and more where greater accuracy is required. For instance, high precision is not needed in the inlet and outlet sections, where only water is flowing; however, in the diverging section of the venturi, where vapor cavities form, higher resolution is necessary. To build a mesh with refined resolution in specific areas, the domain is divided into four sections: the inlet pipe, converging section of the venturi, diverging section of the venturi, and outlet pipe. The first step in mesh construction is to apply face meshing. This tool creates an initial grid within the domain, allowing the user to choose whether the cells should be quadrilaterals or triangles. Since a structured mesh is desired, the quadrilateral option is selected. Fig. 6-9, shows the mesh created using the face meshing tool.

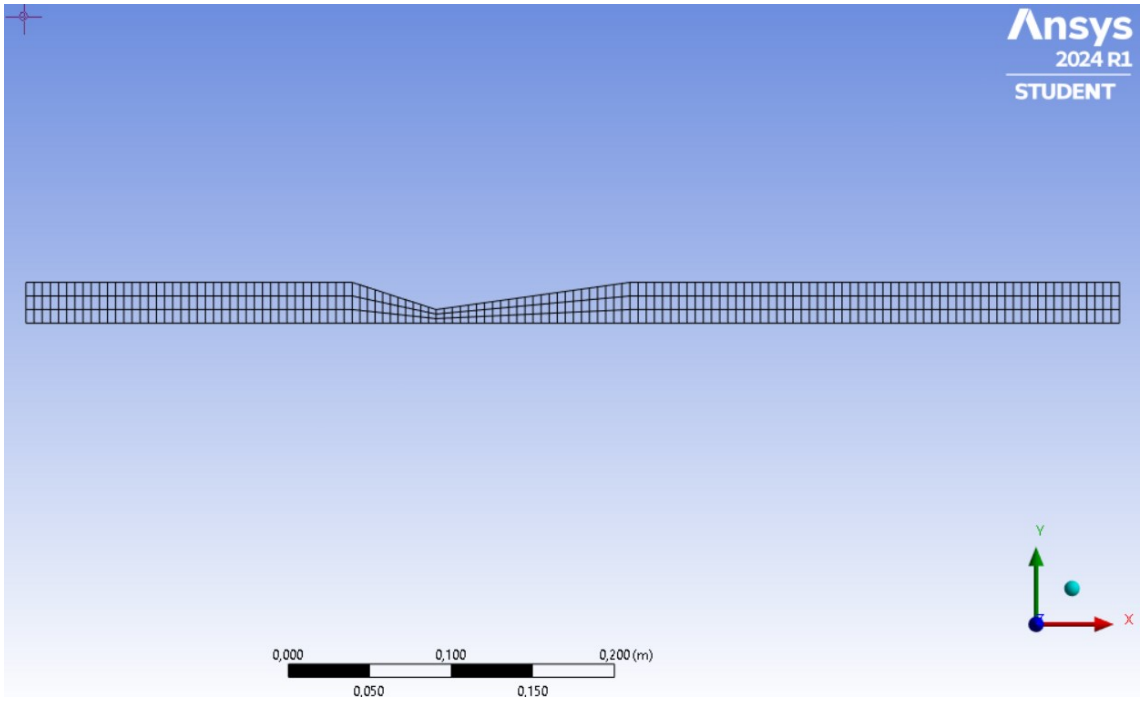

Figure 6-9: Mesh created by default in Ansys Fluent using only the face meshing tool.

This structured mesh is created by default in Ansys, but it may not have the desired element distribution or cell concentration. Therefore, after the face meshing step, it is

necessary to apply sizing to each side of the domain. The sizing option allows you to control the number of cells adjacent to a specific side by defining the number of divisions along that side. In the first mesh constructed, all the radial sides, from the tube's axis to the wall, are given a constant number of ninety divisions. As a result, the number of radial cells remains consistent throughout the entire domain. The horizontal side of the inlet and outlet pipe has a constant number of divisions as well. In these two sections the mesh appears as an ordered grid of equals rectangles, as illustrated in Fig.6-10 representing the grid at the start of the inlet tube.

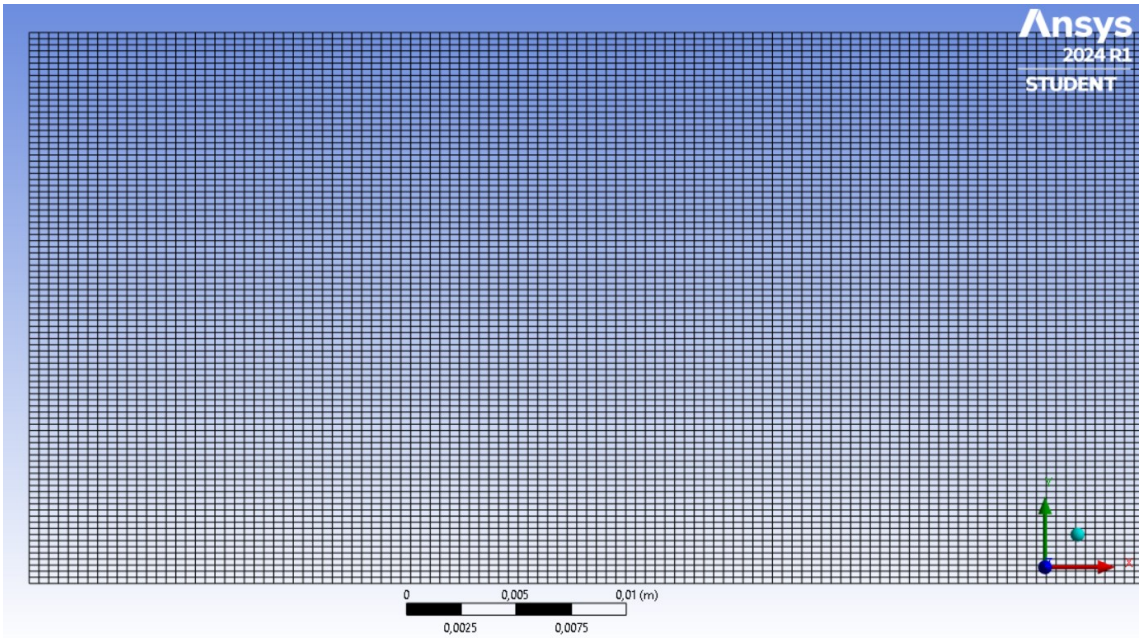

Figure 6-10: Mesh constructed in Ansys fluent at the inlet of the domain.

In the Venturi sections, some adjustments are made compared to other areas of the mesh. As previously explained, cavitation inception occurs at the throat, particularly in the divergent section, due to the lower pressures in this area. To improve accuracy in this critical region, a higher cell density is required. Therefore, a bias is applied to the number of divisions in the converging and diverging sections, concentrating cells in the areas of interest. The chosen bias type is a smooth transition, which gradually increases cell size with each division, based on a bias factor. This approach ensures that each cell is slightly larger than the previous one, creating a smooth growth rate. Fig. 6-11, illustrates the increased cell concentration at the throat.

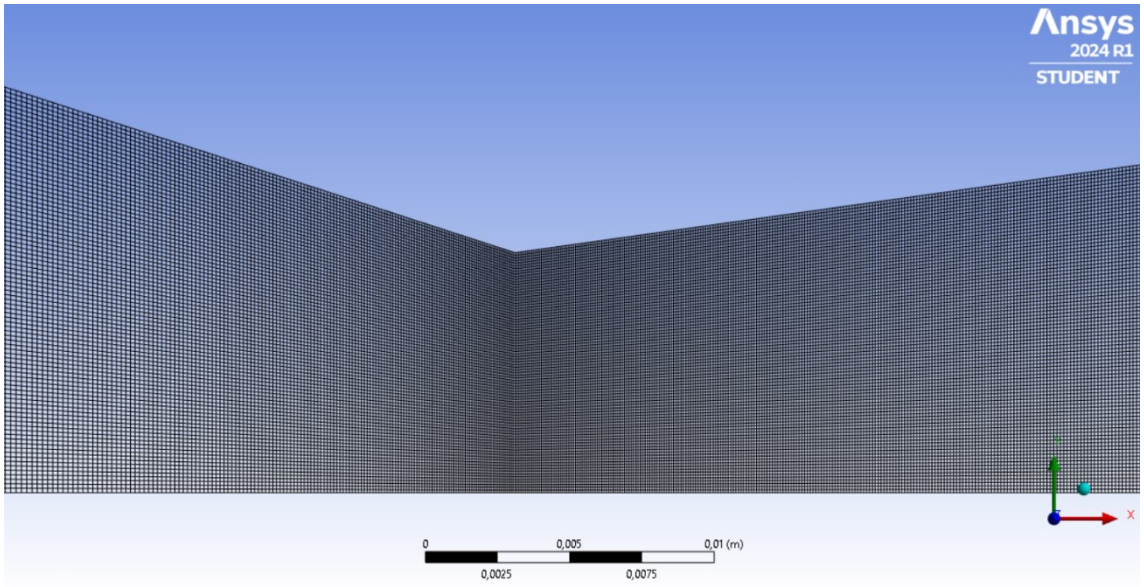

Figure 6-11: Distribution of the cells at the throat.

6.3.3 Problems in the mesh construction

In the construction of the mesh one main problem has occurred. As already said the zone of interest in the domain is the zone of the divergent section near the wall. In the axis of the tube with this geometry vapor cavities do not appear and so is not a zone of interest. In order to increase the precision of the result a bias in the radial direction of the mesh would have been an optimal solution. Numerous tests with different meshes with radial bias have been conducted but they whole failed to get a solution, and the software was not able to solve the flow problem.

6.4 User Defined Functions (UDF)

Ansys fluent is able to simulate a wide range of physical processes, using the implemented functions. Anyway, if a user would like to insert his own equation for a physical property different from the one used by fluent, can do it with the User defined functions (UDF). These are written in C+ code and can be implemented in the software. In this study two different UDFs are implemented: for the vapour density and for the turbulent viscosity.

6.4.1 Vapour compressibility UDF

As already explained, the aim of this thesis is to study the effect of vapour compressibility in the cavitation process. The physics and equations to describe the vapour compressibility have been already explained in Chapter 4.

The vapour density is calculated based on the local pressure, using the equation provided in Chapter Four (Equation 4.22). Particular attention is given to the density calculation as it depends on the pressure. An "if" condition is used to limit the density; at pressures below 400 *Pa* the density remains constant, and the fluid is treated as incompressible. This approach is used because, in the simulations, the solver sometimes produces imperfect solutions with negative pressures in some cells immediately downstream of the throat. These negative pressures are physically impossible and affect the density function, yielding negative densities that are clearly unfeasible and leads to the divergence of the problem flow solution.

6.4.2 Turbulent viscosity UDF

Depending on the different turbulence model, turbulent viscosity is calculated as explained in the section 5.4. In literature many authors used an UDF to limit the turbulent viscosity. This is done because otherwise high turbulent viscosity leads to the generation of a stable vapour cavity [61]. So, the phenomenon of re-entrant jet or condensation shock would not occur without it, oversimplifying the numerical solution. One of the most used methods to limit the turbulent viscosity is the one proposed by Reboud et al. [62]. The Formula proposed is the following:

$$\mu_t = f(\rho)\frac{k}{\omega} \tag{6.2}$$

With the limiting function $f(\rho)$ defined as follow:

$$f(\rho) = \rho_v + (1-\alpha_v)^n(\rho_l - \rho_v) \tag{6.3}$$

The variable *n* has a value between 6-10. With *n* equals to one turbulent viscosity does not change with respect to the normal turbulence model. While increasing it the turbulent viscosity starts to be limited, the higher *n* the higher the limitation of the turbulent viscosity. The volume fraction of the vapour is calculated from the formula:

$$\alpha_v = \frac{\rho - \rho_v}{\rho_v - \rho_l} \tag{6.4}$$

Where with ρ is defined the local pressure.

In this function, the vapour density is limited to a low value of $\rho_v = 0{,}002\ kg/m^3$. This limit is lower than the density threshold set in the previous function concerning vapor compressibility. This adjustment is necessary because, in the simulation, the software frequently exceeds the density limits specified by the function. Setting the limit exactly at the threshold would cause issues if the software-calculated density were to exceed this limit, resulting in a vapor fraction greater than one. Such a value would create problems in the function $f(\rho)$.

6.5 Sensitivity analysis and choice of the mesh

Having constructed the mesh, a sensitivity analysis is then conducted. This analysis is essential to validate the constructed mesh. Different meshes, where the primary difference is the number of elements, are tested and compared. The parameter used for comparison is the pressure difference, Δp , between the inlet and outlet of the Venturi. If an increase in the number of elements results in a significant change in Δp, it indicates that the coarser mesh does not accurately represent the phenomenon. On the other hand, if the Δp value does not change much with an increase in the number of cells, the coarser mesh can be used, as the difference with the finer mesh is not significant, thus requiring less computational power.

Another parameter considered in this analysis is the computational time. The construction of an optimal and efficient mesh is based on two main objectives: grant the best accuracy of the solution and maintain a low computational time. Unfortunately, these requirements have opposite dependence on the number of elements of the mesh: coarser meshes have lower solution time while finer meshes give more precise solutions. The mesh chosen after the analysis will be a trade-off between these two factors. In the initial analysis, the flow problem is examined using three different meshes:

Number of mesh	Number of elements
Mesh 1	100000
Mesh 2	150000
Mesh 3	200000

However, with Mesh 1, the software could not converge, likely because the mesh was too coarse. Therefore, it was decided to continue the analysis with four other meshes, the parameters of which are reported below in tables 6-4 to 6-7.

Mesh 1		
Section	Number of divisions	Bias factor
Inlet pipe	380	None
Converging section	180	1,007
Diverging section	435	1,0025
Outlet pipe	670	None
Radial direction	90	None
Total number of cells: 149850		

Table 6-4: Parameters of Mesh 1.

Mesh 2		
Section	Number of divisions	Bias factor
Inlet pipe	410	None
Converging section	216	1,007
Diverging section	536	1,0025
Outlet pipe	750	None
Radial direction	90	None
Total number of cells: 172080		

Table 6-5: Parameters of Mesh 2.

Mesh 3		
Section	Number of divisions	Bias factor
Inlet pipe	450	None
Converging section	267	1,007
Diverging section	665	1,0025
Outlet pipe	810	None
Radial direction	90	None
Total number of cells: 197280		

Table 6-6: Parameters of Mesh 3.

Mesh 4		
Section	Number of divisions	Bias factor
Inlet pipe	475	None
Converging section	304	1,007
Diverging section	800	1,0023
Outlet pipe	898	None
Radial direction	90	None
Total number of cells: 222930		

Table 6-7: Parameters of Mesh 4.

In the numerical solution, while the outlet pressure is a boundary condition and remains fixed at a constant value, the pressure at the inlet is not constant and varies in all meshes with the same cyclic shape. An illustration of how the inlet pressure varies during the simulation is shown in Fig. 6-14. Here the inlet pressure is plotted with respect to the flow time in the abscissa.

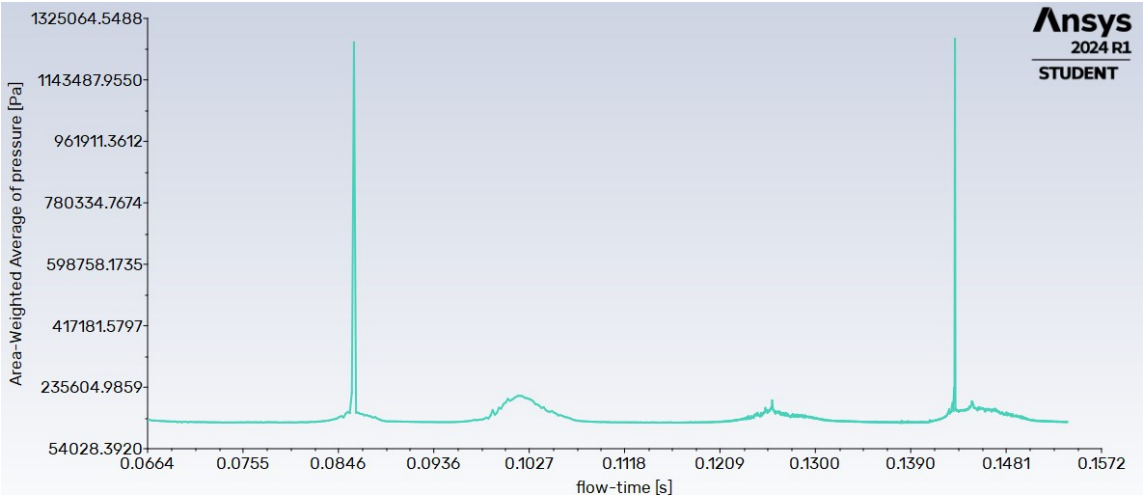

Figure 6-12: Inlet pressure variation during the numerical simulation.

The regions where the inlet pressure increases correspond to the bubble implosion in the divergent section of the Venturi. This occurs because, when solving the governing equations at the timesteps when the vapour bubble is collapsing, the solver finds a solution with extremely high pressure, around 10 bar, in the cells involving the collapse of the vapour bubble. These high pressures then affect the upstream pressure distribution,

creating discontinuities that also impact the inlet of the domain. To determine the inlet pressure values for the sensitivity analysis, the simulation is run until the pressure stabilizes after the peak caused by the bubble implosion. One hundred inlet pressure values, recorded every 50 time-steps, are then collected, and their mean is calculated. This average value is used for the sensitivity analysis.

At the start of the simulation, there is an initial transient phase that does not fully reflect real conditions. Once this phase stabilizes, the cavitation process begins, aligning with the parameters observed in the experimental results of Jahangir [1]. During the transient phase, each mesh configuration reaches convergence at each time step with a varying number of iterations. However, once the transient regime ends and the process begins accurately reflecting real conditions, all simulations, regardless of mesh configuration, reach convergence with a consistent number of iterations per time step. The computational time is then calculated from this stabilized regime onward, by determining the flow time simulated per hour. In Fig. 6-11 the results of the sensitivity analysis are reported in a graph.

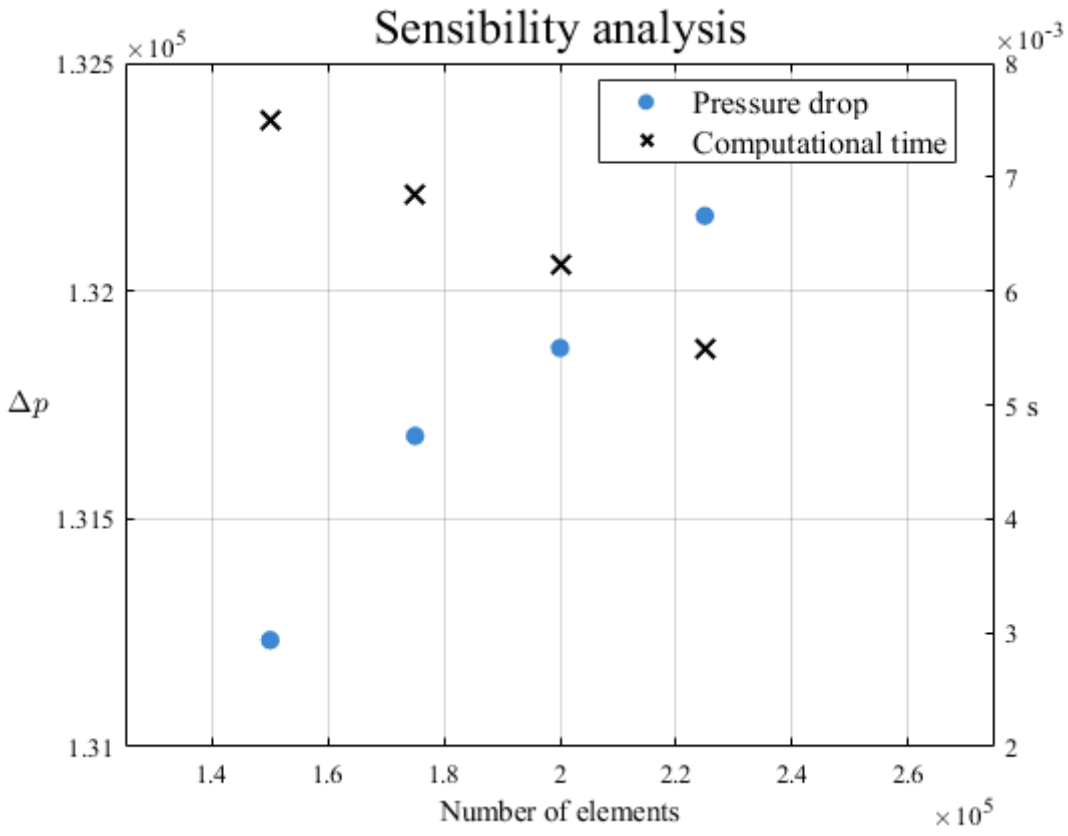

Figure 6-13: Results of the sensitivity analysis.

In the image, the x-axis represents the number of cells in the mesh, while the y-axis shows two sets of data: the blue dots correspond to values Δp, referenced to the left y-axis, and the black x indicate flow time per hour, referenced to the right y-axis. As expected, increasing the number of cells results in a lower flow time per hour and, in this case, also an increase in inlet pressure. Since the difference in Δp values between Mesh 3 and Mesh 4 remains non-negligible ($400\ Pa$), an additional mesh (Mesh 5) was created to determine the cell count at which Δp stabilizes. The data for the new Mesh 5 are reported below.

Mesh 5		
Section	Number of divisions	Bias factor
Inlet pipe	520	None
Converging section	330	1,0063
Diverging section	890	1,002
Outlet pipe	1025	None
Radial direction	90	None
Total number of cells: 248850		

The results of the new mesh are taken in the same way of the others and the new graph for the sensibility analysis is constructed. In Fig. 6-16, the new graph is reported.

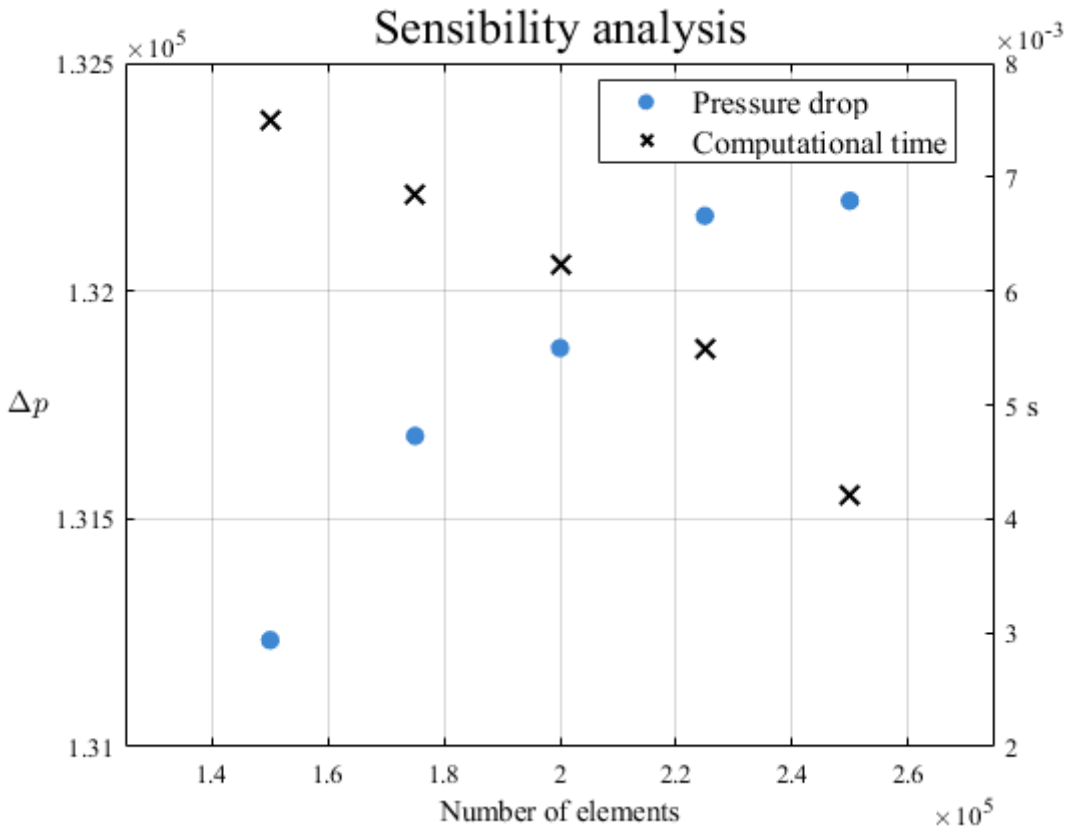

Figure 6-14: Results of the final sensitivity analysis.

With the new mesh a plateau in the Δp value is reached, as Mesh 5 differs from Mesh 4 just by 33 Pa. As regards the flow time Mesh 5 reduces it significantly and so Mesh 4 resulted to be the mesh with the best trade-off between all the meshes. This mesh is used for all further simulations discussed in the following sections of the thesis.

The main quality parameters of the mesh selected are illustrated below. Fig. 6-17 shows the aspect ratio of the mesh, which remains close to the ideal value of one throughout the domain and does not exceed a value of two. Fig. 6-18 illustrates the skewness parameter within the domain, which achieves an optimal level, with more than half of the cells exhibiting a value of zero. Additionally, the orthogonal quality, reported in Fig. 6-19, also reaches an optimal level, with over 60% of the cells having the ideal value of 0.

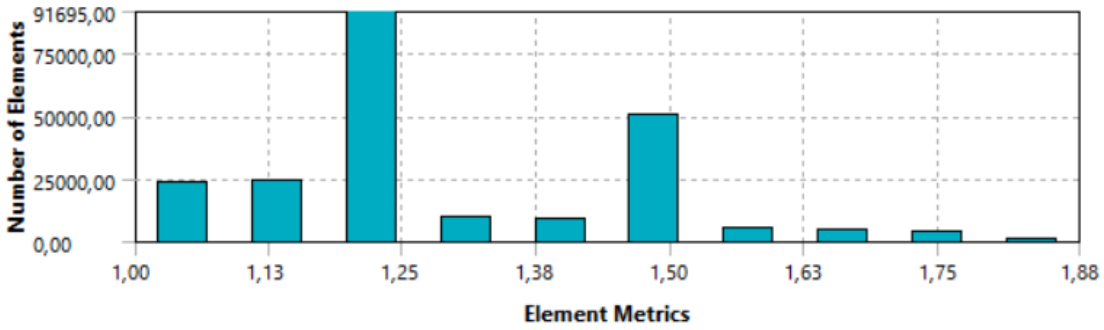

Figure 6-15: Value of the aspect ratio in all the domain.

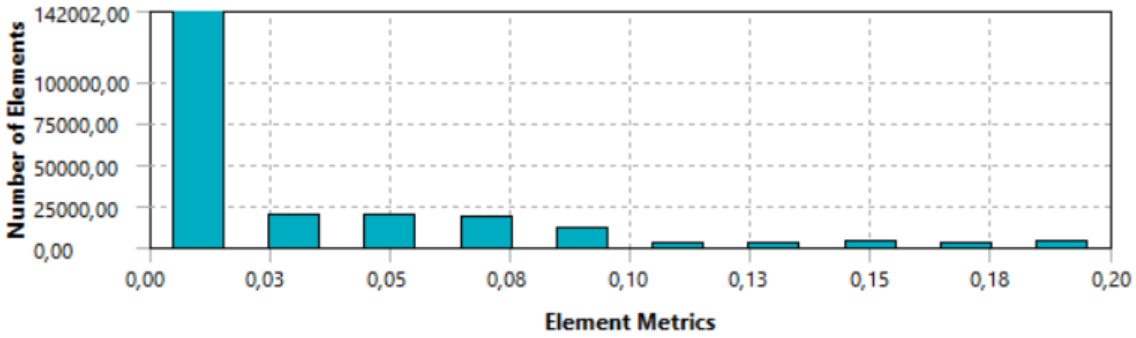

Figure 6-16: Skewness parameter in the domain.

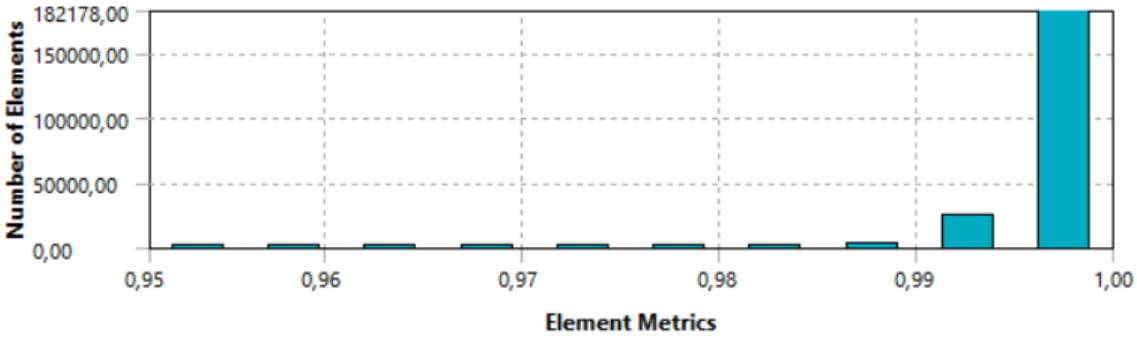

Figure 6-17:Orthogonal quality in the domain.

6.6 Setup and initialization

With the mesh construction complete, the solver can now be initiated to solve the flow problem. This section outlines the models and settings used in the simulations. The selection of these settings is informed by literature, particularly by the works of [63], [64] and [2], where the simulated data effectively replicated the experimental results.

6.6.1 General settings

In the general settings, the basic parameters of the simulation are defined. This simulation is set to transient mode, as it aims to analyse the shedding cycle of the cavitation process. This would not be possible with a steady state analysis. The solver is settled as pressure-based, and the flow is modelled as axisymmetric because only a radial section of the Venturi tube is provided to the solver.

6.6.2 Models

In this section, the necessary models for the simulation can be selected. The chosen homogeneous mixture model is the Volume of Fluid (VOF) model. Using this approach, the Schnerr and Sauer cavitation model is applied, with the saturation pressure set according to Table 6-1 and the number of bubbles per unit volume set as $n_b = 10^{11}$. In this setup, water is defined as phase one and vapour as phase two. The energy equation is enabled, as the problem involves a compressible fluid, and the k-ω SST model is selected for turbulence. This turbulence model is chosen due to the highly turbulent nature of the flow and to ensure accurate resolution near the walls, where cavitation phenomena primarily occur.

6.6.3 Materials

In the materials section all the properties settled in Table 6-1 are insert. For the vapour at the density selection the UDF option is selected and the UDF explained in the paragraph 6.4.1 is implemented. When the user defined option is selected in the density selection, a new paragraph for the speed of sound appears. Here in necessary to insert the speed of sound of the compressible liquid calculated following the equation already explained in chapter 4:

$$c = \sqrt{\frac{K_s}{\rho}} \qquad 6.5$$

So, from the properties of the material reported in table 6-2 and the formulas described in Chapter 4 is possible to calculate the speed of sound of the vapour:

$$c = \sqrt{\frac{K_s}{\rho}} = \sqrt{\frac{\gamma\, p_{ref}}{\rho_{ref}}} = \sqrt{\frac{1{,}33 * 2338}{0{,}0173}} \cong 424\ m/s \qquad 6.6$$

In the speed of sound paragraph is selected the option constant and this value is inserted.

6.6.4 Boundary conditions

In this section the boundary conditions of the domain are settled. First the reference pressure is fixed to zero. As regards the simulations of this study, the outlet pressure is fixed $80000\ Pa$, while the inlet velocity is varied to study the cavitation at different operative conditions as in the work of Brunhart [2]. In both inlet and outlet, the turbulence intensity is set to 5%. Regarding the vapour distribution, at the inlet the volume fraction of vapour is set to zero. For the wall, a no slip condition is chosen with a standard roughness model.

6.6.5 Methods

This section determines the methods used for the numerical solution of the flow problem. All the methods chosen are reported in Table 6-8. The SIMPLE scheme is one of the most used methods for solving the pressure-velocity coupling in CFD simulations. Since pressure does not explicitly appear in the continuity equation, the SIMPLE method employs a pressure correction function linked to velocity to compute pressure, ensuring continuity in the numerical solution. The PRESTO! scheme is adopted in this study, as it is recommended for flow problems involving adverse pressure gradients. For the volume fraction calculation, the CICSAM scheme is used, as the numerical solution failed to converge with the Geo-Reconstruct method. The Second-Order Upwind scheme is applied to all other variables. This approach provides a second-order approximation, as the variables in each cell are calculated based on the values from a larger surrounding region compared to the First-Order Upwind scheme. This ensures a more precise and accurate solution.

Pressure-velocity coupling	SIMPLE
Gradient	Least Squares Cell Based
Pressure	PRESTO!
Momentum	Second Order Upwind
Volume Fraction	CICSAM
Turbulent kinetic energy	Second order Upwind
Specific Dissipation Rate	Second order Upwind
Energy	Second order Upwind

Table 6-8: Methods Used for the numerical resolution.

6.6.6 Controls

In this section it is possible to set the under-relaxation factors. These can be modified to stabilize the numerical resolution of the flow problem. The Under-relaxation factors regulate the update values of the cells. They work following the sequent formula:

$$\phi_{new} = \phi_{old} + \alpha\,(\phi_{calculated} - \phi_{old}) \qquad 6.7$$

Here ϕ_{new} is the updated value of the parameter ϕ, ϕ_{old} is the value of the variable the iteration before while $\phi_{calculated}$ is the value calculated by the software. α instead, is the relaxation factor. For $\alpha = 1$ the new value will be exactly the one calculated by the solver, while instead decreasing it the new value of ϕ will result in a combination between the old value and the one calculated. This reduces the increase of ϕ and stabilize the solution. Anyway, Under-relaxation factors too low, may bring instabilities to the solving process. In fact, if not well settled they can increase a lot the computational time. They can also limit the change of some variables that need have a high change, leading to instability of the solution or to a solution not coherent or true of the flow problem. In the work done for this thesis numerous combinations of relaxation factors have been tested and the one comporting the higher stability was used.

6.6.7 Calculation

The time-step used is one microsecond according to the previous work. Forty iteration per time step are selected and the convergence of each time-step is reached when all the residuals have a value of 10^{-5} except for the energy where residuals must reach 10^{-6}.

6.6.8 Initialization

The initialization process of a CFD simulation provides an initial numerical solution to the flow problem. A proper initialization offers several benefits to the solving process, including reduced computational time, improved numerical stability, and better convergence of the flow problem toward the physical solution. In this study, the initialization is carried out by performing a steady-state analysis of the flow problem, using the same boundary conditions as the original case but excluding the cavitation model. Specifically, a steady-state analysis of water flow within the Venturi is conducted. Once convergence is achieved, all the previously described models are applied, and the transient simulation is initiated.

7 Results

In this chapter, the results of the numerical model are presented. First, an analysis is performed to explain how the cavitation process varies depending on the inlet velocity. Here it is explained how the initial transient regime behaves in the numerical simulations and the problems that brings in it. Then the shedding principles are individuated and explained basing on the results of the simulations. Finally, the numerical results basing on the dimensionless numbers are validated by comparison with the works of Jahangir [1] and Brunhart [2].

7.1 Analysis

In this thesis, as discussed in Chapter 6.6.4, different simulations are conducted by varying the inlet velocity while maintaining the same outlet pressure, in accordance with the work of Brunhart [2]. In table 7-1, are reported the boundary condition used for the simulations.

Boundary conditions	
Inlet velocity	80000 Pa
1,3 m/s	80000 Pa
1,45 m/s	80000 Pa
1,6 m/s	80000 Pa
1,75 m/s	80000 Pa
1,9 m/s	80000 Pa
2 m/s	80000 Pa

Table 7-1: Boundary conditions of the simulations performed.

In all simulations, as mentioned in previous chapters, once the numerical simulation begins, a transient regime develops that does not correspond to the experimental data from previous studies. Specifically, the higher the inlet velocity, the greater the deviation of the transient regime from the real phenomena. At the start of the simulation, an initial vapor cavity larger than what would occur in a real scenario is formed. After detachment, the vapor bubble flows into the divergent section and implodes at a distance from the

throat that is greater than the one registered after the transient regime. Fig. 7-1 presents a comparison between the bubble implosion in and after the transient with a cavitation number: $\sigma_D = 0{,}88$. In the transient, Fig. 7-1 (a), bubble implosion occurs at a distance from the throat of $5{,}4\ cm$ while after the transient the bubble implosion occurs at $3{,}3\ cm$. In the legend of the figure the volume fraction of water (phase one) is reported.

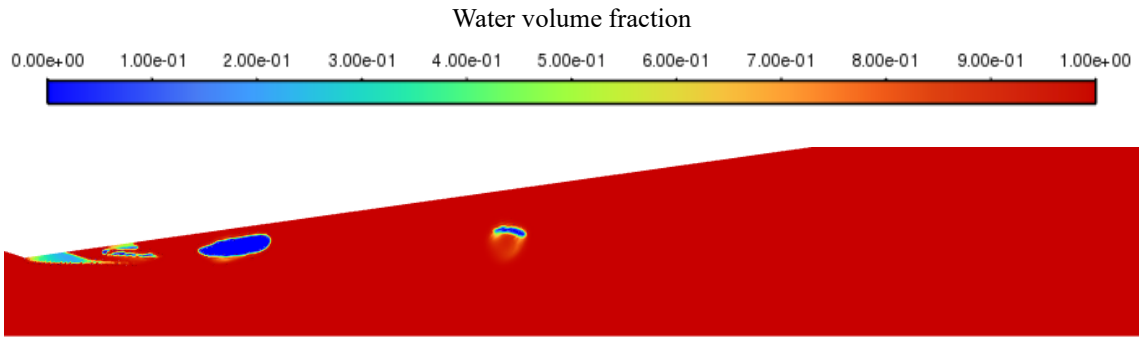

(a) Implosion in the transient regime.

(b) Implosion after the transient regime.

Figure 7-1: Comparison between bubble implosion in the transient (a) regime and after (b).

This transient regime created some problems in the initial convergence of the solution. In fact, for inlet velocities higher than $1.9\ m/s$, the implosion of the first bubble in the transient regime occurred too far from the throat, leading to a divergence in the solution. Therefore, during the timesteps involving the bubble implosion, the UDF for vapour density was deactivated, and a constant value equal to its reference value was applied. Immediately after the bubble implosion, the UDF was reactivated in the model. Once the transient regime is concluded the real regime reflecting the real cavitation process behaviour starts occurring. Depending on the shedding mechanism the development of the cavity started.

7.1.1 Re-entrant jet mechanism

At low velocities and thus high σ_D, the cavity develops following the re-entrant jet mechanism described in Chapter 3.1. As shown in Fig. 7-2, once the cavity begins to form, a re-entrant jet with an adverse velocity relative to the main flow appears, separating the vapor from the wall. As the simulation progresses, the vapor cavity continues to grow, and the jet increases in magnitude, reaching near the throat and completely detaching the vapor bubble from the wall. Subsequently, the vapor bubble is transported through the divergent section and collapses.

Meanwhile, at the throat, a new vapor cavity develops, accompanied by a re-entrant jet that generates a new bubble while the previous one is still collapsing in the divergent section. Once the first bubble collapses, both the second bubble formed and the vapour cavity at the throat condense, returning to the initial condition with no vapour in the venturi tube.

Figure 7-2 illustrates the evolution of the re-entrant jet phenomenon in the simulation with $\sigma_D = 0{,}88$. Using the first image as a reference time of zero, the relative flow time in millisecond for each subsequent image is indicated.

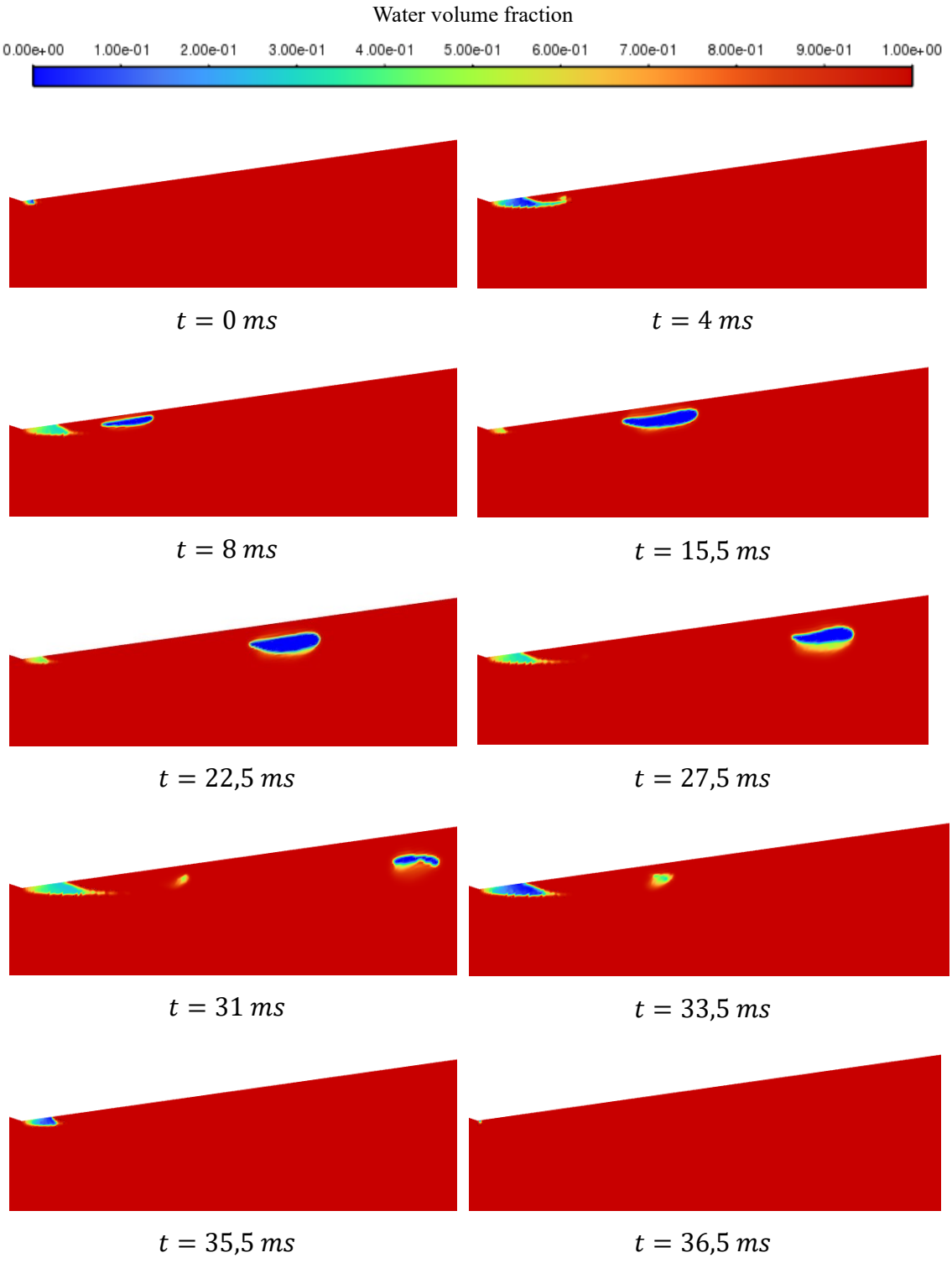

Figure 7-2: Re-entrant jet mechanism in the model with the operating conditions $\sigma_D = 0{,}88$.

The evolution of the re-entrant jet is illustrated in Fig. 7-3, using contours of the axial velocity. These are presented with the same reference time as before. It is possible to observe how the re-entrant jet grows and increases in magnitude as the vapor cavity expands, progressively approaching the throat. Subsequently, when a new cycle begins, the re-entrant jet near the throat starts to diminish in both the zones of interest and its magnitude in the vicinity of the throat. This process continues until a new vapor cavity develops and a new re-entrant jet begins to form.

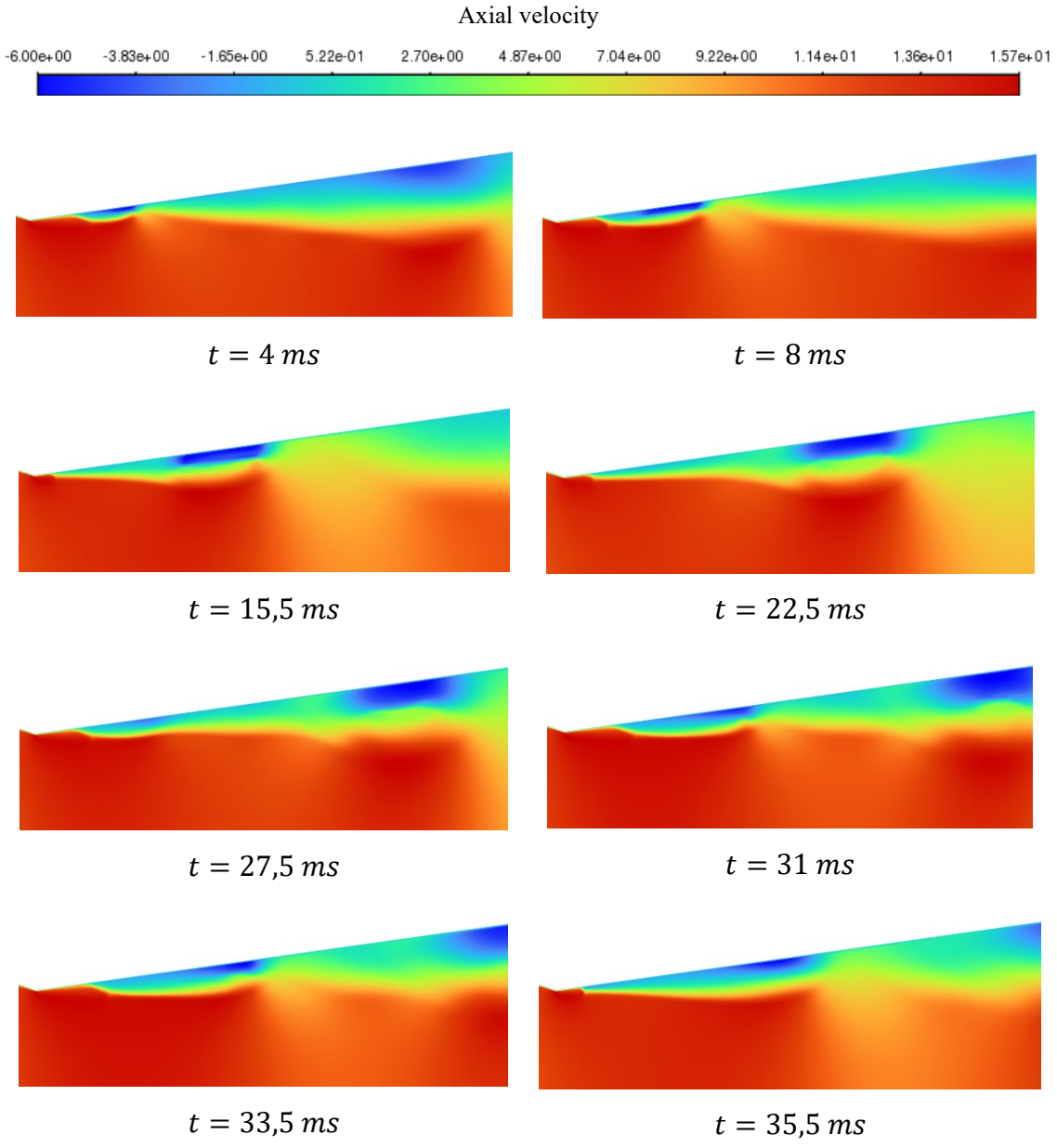

Figure 7-3: evolution of axial velocity in the model with the operating conditions: $\sigma_D = 0{,}88$.

7.1.2 Condensation shock

Increasing the inlet velocity, and thus reducing the cavitation number, changes the development of the vapor cavity leading to the condensation shock mechanism, explained in Chapter 3.2. Once cavitation inception occurs at the throat, a large vapor cavity forms and remains attached to the wall. Subsequently, due to the presence of an adverse velocity, a large vapor bubble detaches and is carried through the divergent section of the venturi.

Meanwhile, a stable presence of vapor remains attached at the throat, where another large vapour bubble begins to form. Unlike the previous bubble, this one remains attached to the wall near the throat, increasing in size as the first bubble begins to condense while moving through the divergent section of the venturi. When this downstream bubble starts to collapse, the vapor bubble at the throat is divided into many smaller bubbles. Instead of a single large bubble, a vapor cloud appears. Finally, once the implosion of the first bubble is complete, all vapor particles in the divergent condense, returning the system to its initial conditions.

In Fig. 7-4, the shedding mechanism is illustrated. To show it, the volume fraction of water at different flow times is showed of the model with a cavitation number $\sigma_D = 0{,}46$. As before a reference time of zero milliseconds is taken from the first image and at the initials flow times of the figure a focus in the near throat section is applied.

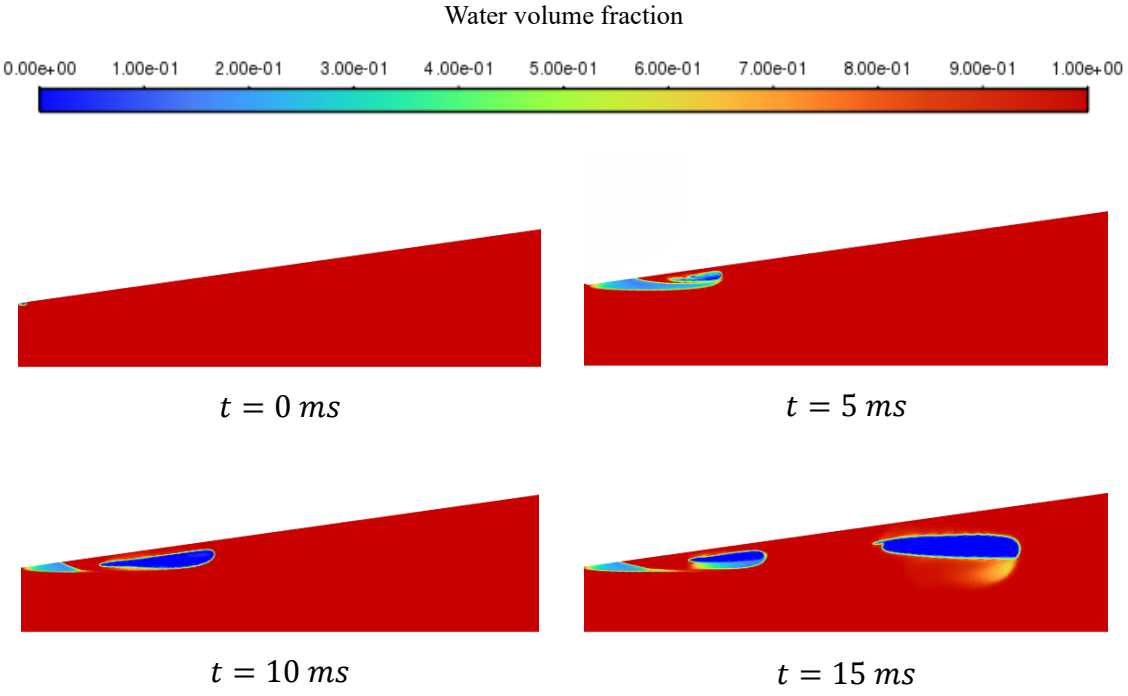

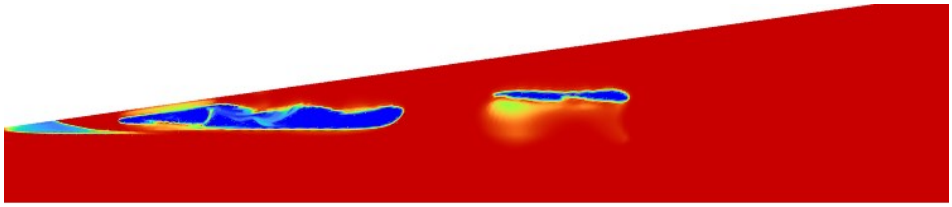

$t = 17{,}5\ ms$

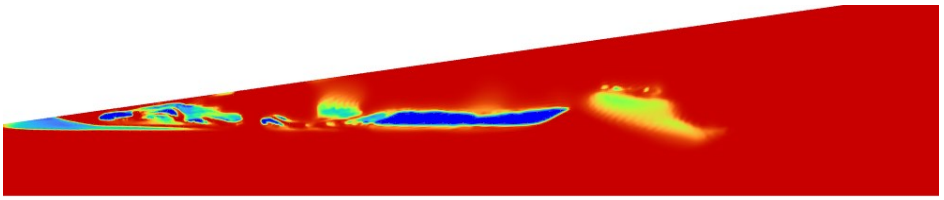

$t = 20{,}5\ ms$

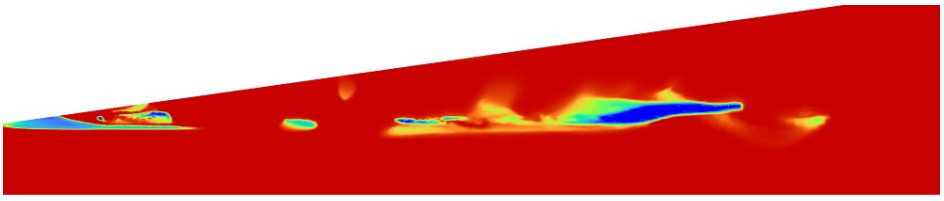

$t = 23{,}5\ ms$

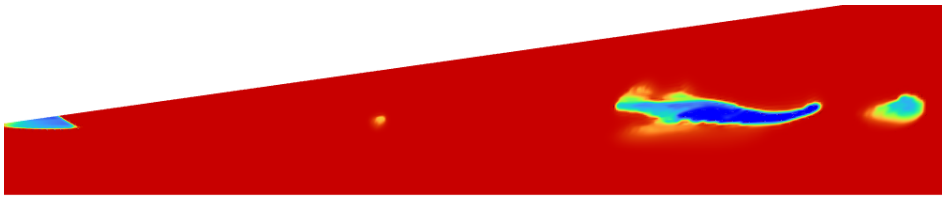

$t = 26{,}5\ ms$

$t = 29{,}5\ ms$

$t = 32{,}5\ ms$

Figure 7-4: Condensation shock mechanism of the model with $\sigma_D = 0{,}46$.

Unlike the previous mechanism, in the simulations conducted at this cavitation number, the axial velocity exhibits a different behaviour. During the initial inception of the cavitation process, as the vapor bubble begins to form, a re-entrant jet with greater magnitude and a larger zone of influence develops. This jet is responsible for the detachment of the first large vapor bubble in the process.

However, once this vapor bubble detaches, the velocity at the wall, as well as in the region where the second bubble forms, remains close to zero, with no re-entrant jet flowing in the opposite direction of the main flow. For this reason, the second cavity forms near the wall and does not detach from it.

Figure 7-5 shows the axial velocity at different flow times, referenced to the time in Fig. 7-4. In the first image at $t = 10\ ms$, the re-entrant jet separates the bubble from the wall. By $t = 17{,}5\ ms$, the velocity in the region where the vapor cavity forms is close to zero.

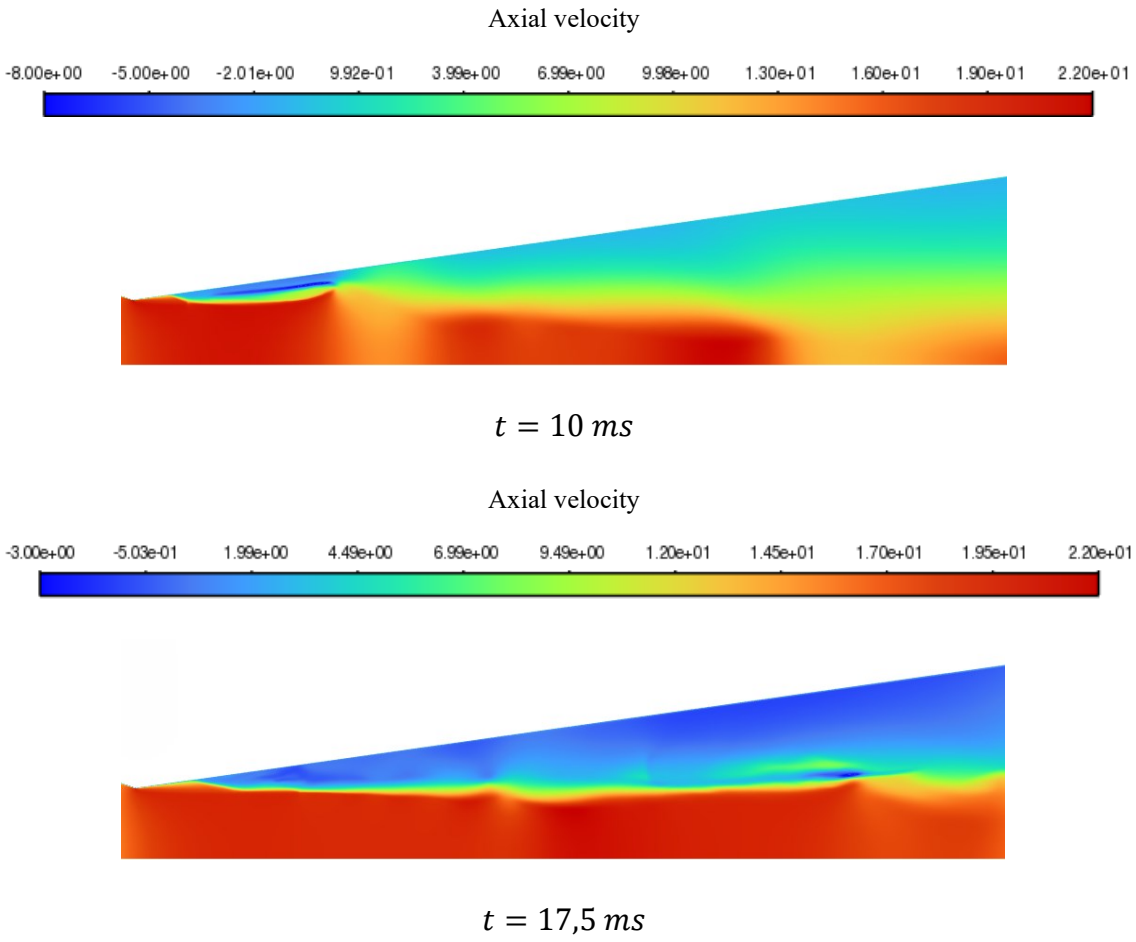

Figure 7-5: axial velocity for different flow times at $\sigma_D = 0{,}46$.

In the theory of the condensation shock mechanism described in Chapter 3.2, it is explained that the creation of a vapor cloud from a stable cavity is caused by the perturbation generated downstream by the vapor cloud implosion. This occurs because, as vapor is compressible, the cavity can transport the downstream disturbance to the upstream side of the Venturi. In line with this explanation, the vapor cloud formation observed in the model during the bubble implosion is attributed to the compressibility implemented in the vapor phase of the model. The bubble implosion acts as a perturbation, which diffuses through the vapor cavity and creates the vapor cloud. If the vapor phase were treated as incompressible, this perturbation would not have been transmitted in this manner, and the vapor cloud formation resulting from the bubble implosion would not have occurred.

7.1.3 Differences from experiment

In the results of the simulations conducted, the development of the vapor cavity at different cavitation numbers revealed several differences compared to the findings of Jahangir [1]. During the re-entrant jet process at a high cavitation number, the behaviour closely resembles the experimental observations. In particular, the development of the re-entrant jet in the axial velocity is almost identical to what is observed in the experiments.

However, under these operating conditions, the model reveals a correlation between the downstream bubble implosion and the remaining vapour on the upstream side of the Venturi that do not occur in the experiment. Specifically, as the downstream bubble implodes, all the upstream vapour in the Venturi condenses within three milliseconds. In the experiments conducted by Jahangir [1] and the findings reported by Brunhart [2], the implosion of the downstream bubble did not affect the upstream vapor in this manner. During the downstream bubble implosion, in fact, the new cycle at the throat continued undisturbed by the implosion.

When the inlet velocity increases, and thus the cavitation number decreases, the shedding mechanism shifts to a condensation shock regime. Here, one of the main differences between the simulations and the experiments is the initial formation of a large bubble and the appearance of a re-entrant jet that detaches this bubble from the wall. As the simulation progresses, similarly to what was observed in Jahangir [1], the second cavity remains attached to the wall and increases in size. Additionally, consistent with the

experiments, once the upstream bubble collapses, this cavity fragments and becomes a vapor cloud.

However, another difference from the experiments occurs at this stage. Following the experimental results of Jahangir [1] and how explained in Chapter 3.2, the vapour cloud formed, flows in the downstream of the venturi and its implosion is the driving mechanism to the formation of the new cycle vapour cloud. Instead in the model the vapour cloud formed completely condenses, until no vapour is present in the whole venturi, how well presented in Figure 7-4 , and the cycle restarts from the initial bubble formation.

In the numerical resolution of the model, for both shedding mechanisms, a correlation between the downstream bubble implosion and the remaining vapour in the domain is evident. Once the downstream bubble implodes, the vapour in the upstream direction condenses within a few timesteps. Specifically, during the bubble implosion, the numerical solution converges, resulting in a high local pressure on the order of $10\ MPa$. After the implosion is completed, this pressure diffuses upstream, reaching the nearest vapour bubble, causing its condensation and subsequent implosion. This pressure process continues until, within a few milliseconds, all vapor cavities or bubbles in the domain implode, leaving no vapor present in the Venturi.

This phenomenon was not observed in the experiment described by Jahangir [1], nor in the work of Brunhart [2], as the evolution of pressure in the numerical solution was not their focus. Nonetheless, the appearance of high pressure at the implosion location aligns with the cavitation phenomena theory explained in Chapter 3. However, further studies are required to determine whether this pressure process arises due to the numerical solution's method of solving the flow problem or if it reflects the actual cavitation process.

7.2 Validation

In this section, the numerical simulation results analysed earlier are validated based on the works of Jahangir [1] and Brunhart [2]. Specifically, in the work conducted by Brunhart [2], graphs of the dimensionless cavitation numbers, explained in the first chapter, are constructed and compared with the experimental results. The results obtained from the developed numerical simulations are added to these graphs to validate the numerical approach. Three different dimensionless numbers are used and are here reported.

Loss Factor: $$K = \frac{\Delta p}{\frac{1}{2}\rho u^2} \tag{7.1}$$

Strohual number: $$St_d = \frac{f\ D}{u} \tag{7.2}$$

Cavitation number: $$CN = \frac{\Delta p}{p_d - p_v} \tag{7.3}$$

Downstream cavitation number: $$\sigma_D = \frac{p_{down} - p_{vap}}{\frac{1}{2}\rho u^2} \tag{7.4}$$

Where St_d, K and σ_D, are all explained in Chapter 2.3. CN is an alternative cavitation number used in the work of Brunhart [2].

The first graph presented in Fig. 7-6 represents the correlation with K and σ_D. Here, the red dots represent the experimental values of Jahangir [1], the blue diamonds are the results from the work of Brunhart [2] and finally the green triangles are the results obtained from the simulation conducted in this study.

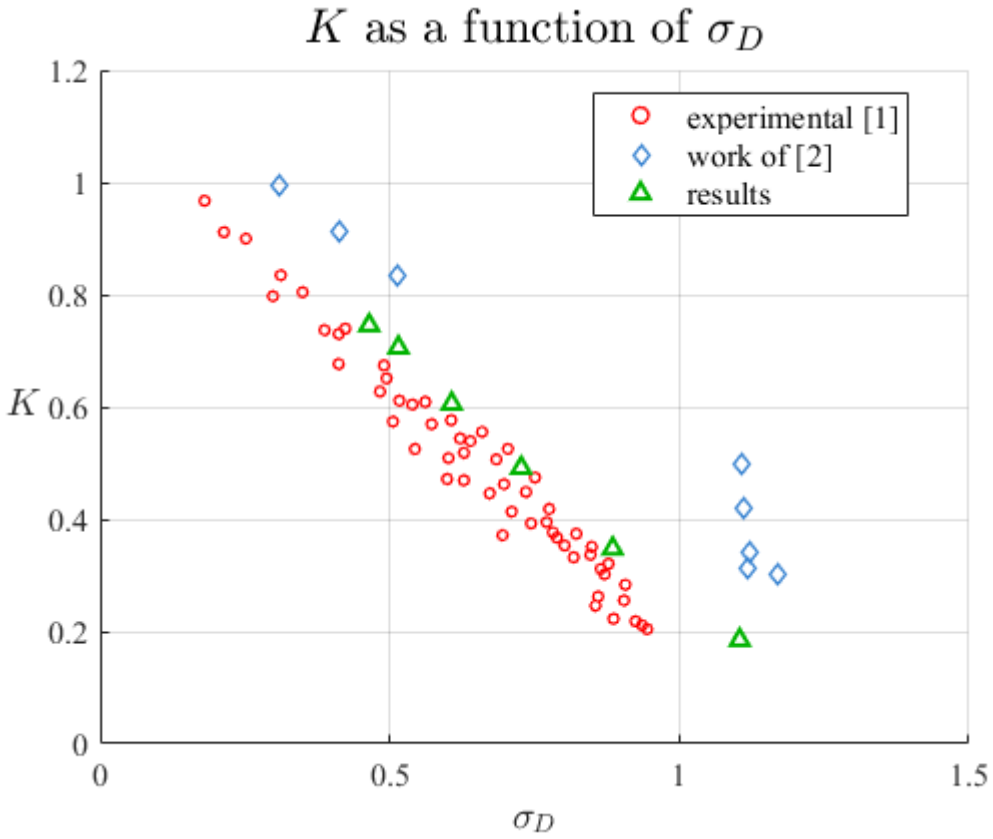

Figure 7-6: K as a function of σ_D.

As the inlet velocity increases, the cavitation number decreases, due to a consequent increment of the throat mean velocity. Additionally, a wider region at the throat will exhibit high velocity and consequently low pressure, leading to a greater presence of vapor in the divergent section. This can be confirmed by the values of the loss factor K. From these values, and the data presented in Fig. 7-6, the correlation between the amount of vapor and the pressure losses becomes evident. Specifically, as the inlet velocity increases, despite the rise in throat velocity, the pressure losses increase significantly, resulting in a higher loss factor. This supports the conclusion that the greater the amount of vapor in the divergent, the higher the pressure losses. This observation is further corroborated by the results of the simulations conducted. From the graph, it is evident that the data show a strong correlation with the experimental values reported in the work of Jahangir [1], giving better results than the values of Brunhart [2].

All these considerations are valid also using the additional cavitation number used by Brunhart [2] called CN. In Fig.7-7 is reported the $CN - K$ graph, where red dots represent

the experimental results, blue diamond's represent the results obtained in Brunhart [2] work and green triangles are the results of the simulations performed in this work.

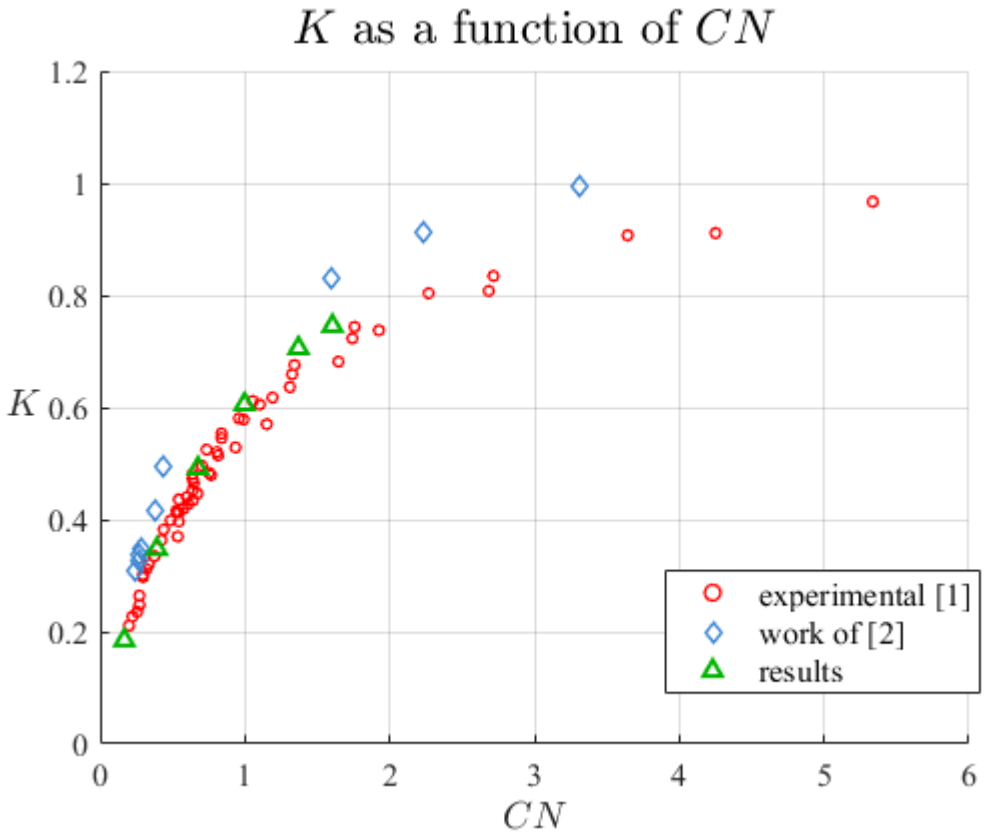

Figure 7-7: K as a function of CN.

So, as regards the performance of the model it is possible to conclude that the results obtained on the model constructed are reliable and reflect the real behaviour of the process.

Another crucial aspect to characterize cavitation phenomena is its frequency. As mentioned in the earlier chapters, and as observed in the discussion of the shedding mechanism during the analysis of the results, the cavitation process in a venturi tube, despite being extremely complex, occurs with a certain frequency that varies depending on the cavitation number. As explained in Chapter 3, each cycle of the cavitation process begins and ends when the vapor cavity at the throat disappears, regardless of the specific cavitation shedding mechanism. To capture this behaviour in the model, two monitoring lines were placed near the throat at the start of the divergent section. These lines were

used to track the average density values, recorded every 100 timesteps, corresponding to intervals of 0.1 milliseconds.

In Fig. 7-8 the two lines used for the frequency analysis are showed in the geometry of the venturi, highlighted by yellow.

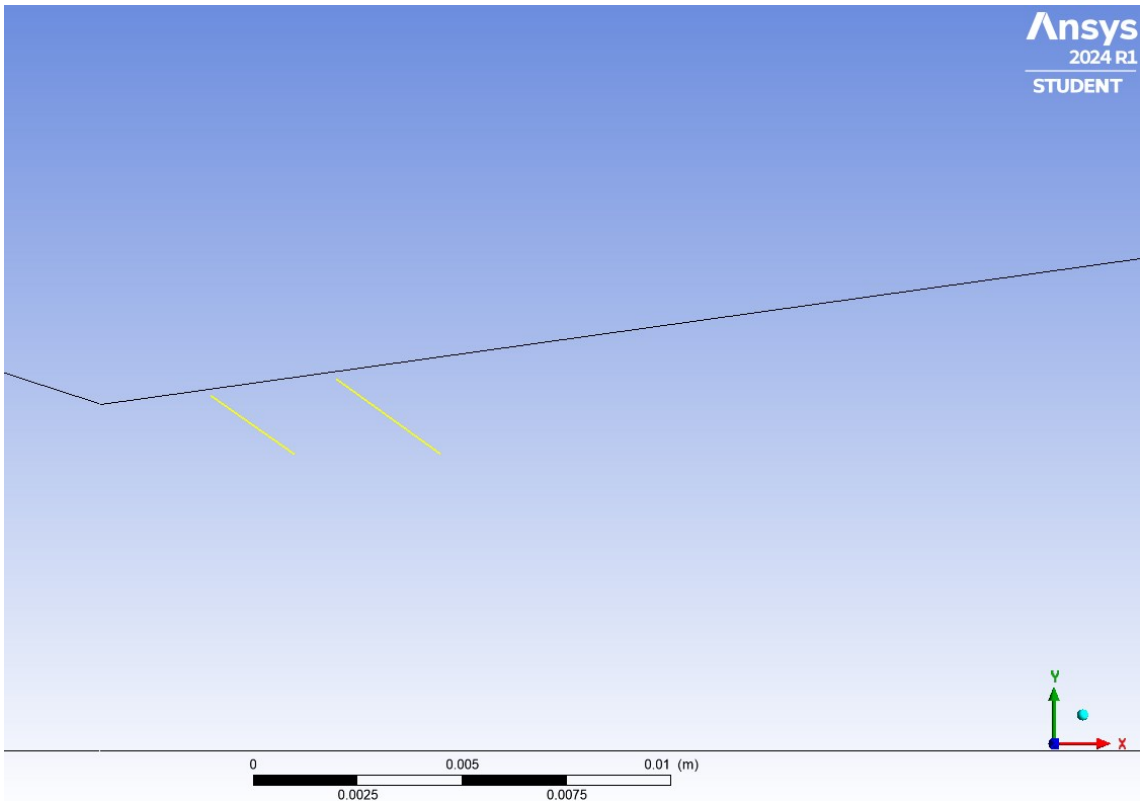

Figure 7-8: Lines used for the frequency analysis.

With these data it was possible to identify at which time step and flow time at the location of the line, there was only water and when the vapour started appearing in it. To determine the time required to complete an entire cycle, the flow time at the start of a cycle is subtracted from the flow time at the start of the previous cycle. The beginning of a cycle can be identified when the average density along the line decreases from the reference value of water. This decrease indicates the presence of a fraction of vapor in the line, signifying the start of a new cycle. Calculating the period of the cycle it was than possible to get its frequency and so to calculate the dimensionless number St_d.

The dimensionless numbers calculated were than reported with a graph to determine their accuracy with respect to the other two works. The results about the St_d number versus

the cavitation number σ_D, are reported in Fig. 7-9, where the different series of data are the same of the previous two graphs.

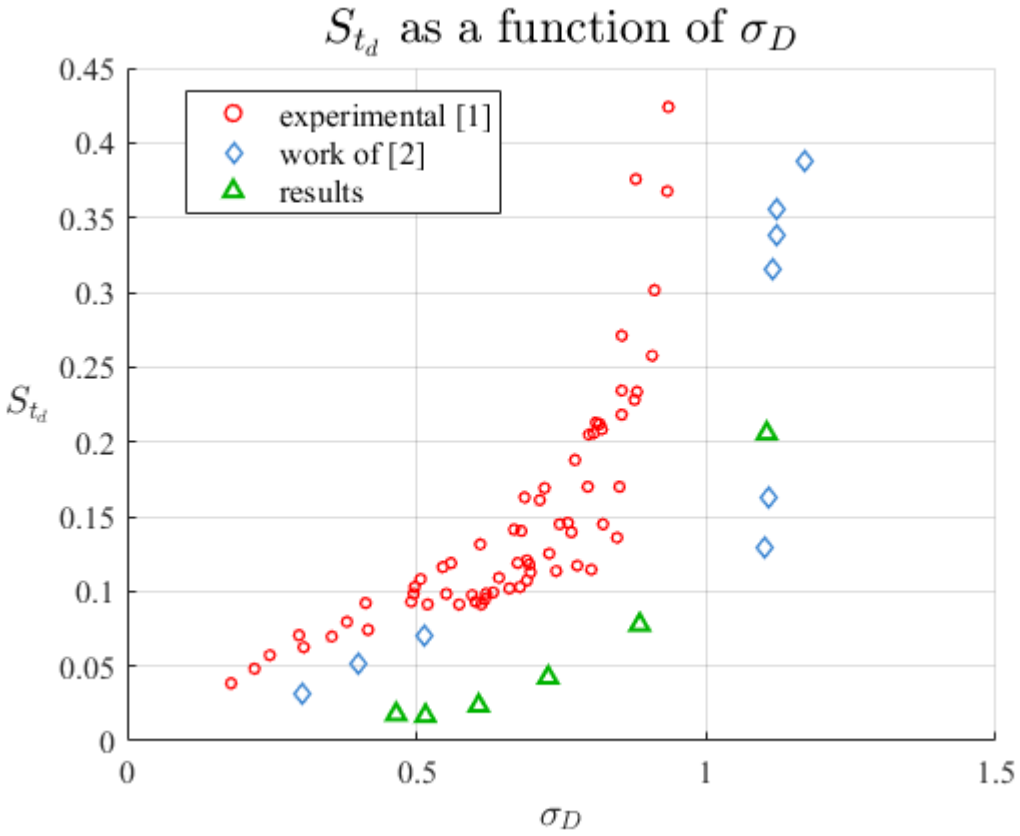

Figure 7-9: St_d as a function of σ_D.

Here is evident how the model does not attend the experimental results and neither the results of Brunhart [2]. In particular for the re-entrant jet shedding, the frequency of the simulations performed is half of the real phenomena or even less. Anyway, the general behaviour of the results is similar to the experiment. In fact, the frequency at high cavitation numbers is the higher, while decreasing it first a big difference is registered and then at low cavitation numbers a sort of plateau is registered once the condensation shock mechanism starts. These considerations are valid also when calculating the correlation between St_d and the cavitation number CN illustrated in Fig. 7-10. Here the results reported have a similar behaviour with respect to the previous data collected in Fig. 7-9 with a St_d number that is sensibly lower than the two works taken as reference.

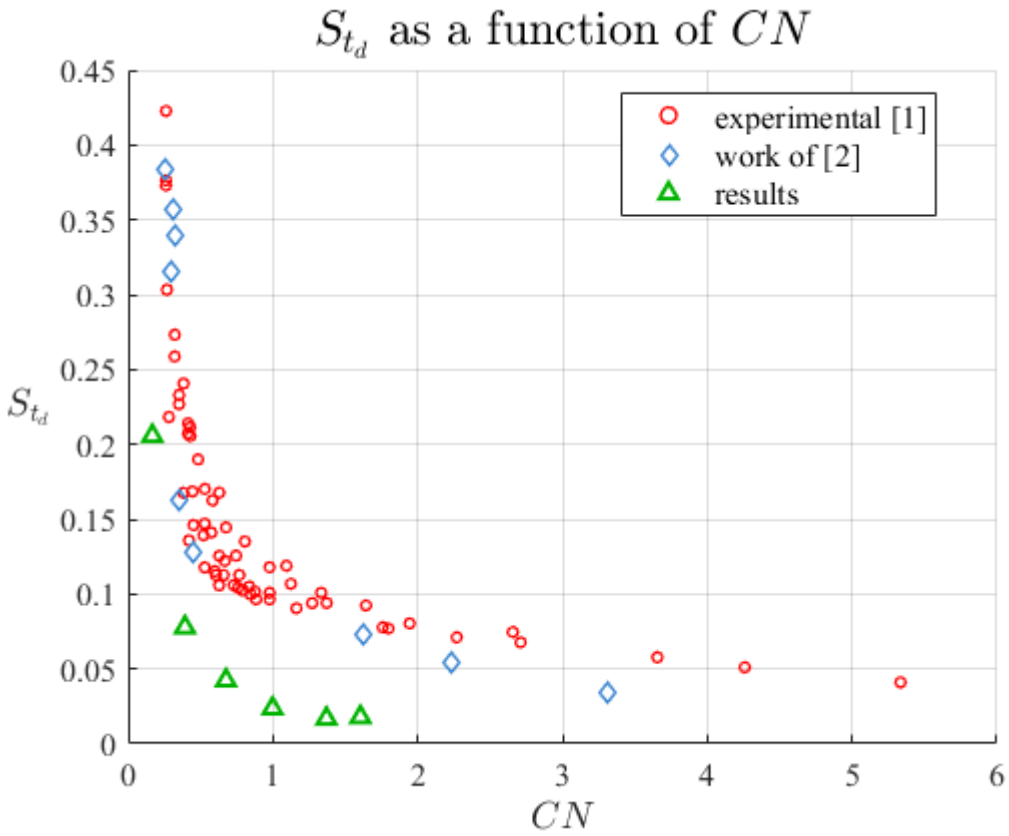

Figure 7-10: St_d as a function of CN.

Is evident from the results reported that while the performance of the model resulted to be reliable, its frequency is not. In fact, in particular for high cavitation number σ_D where the re-entrant jet shedding occur the frequency resulted to be sensibly lower than the experimental data.

7.3 Model limitations

In the simulations performed, the main limitation was the value of the dimensionless parameter Y^+. As explained in Chapter Five, this parameter is crucial for accurately resolving the flow in the vicinity of the wall. To achieve reliable results using the SST k-ω turbulence model, Y^+ must remain within specific ranges: values below 5 ensure accurate resolution of the wall boundary layer, while values above 30 allow the use of wall functions. However, Y^+ values falling between 5 and 30 correspond to the buffer layer, where neither approach can fully resolve the flow behavior near the wall.

In the simulations, Y^+ values varied depending on the inlet velocity. Given how Y^+ is defined, it is clear that increasing the velocity raises its value, while decreasing the velocity lowers it. In most simulations, the majority of the wall surface in the divergent section exhibited Y^+ values between 5 and 30, placing them in the buffer layer. This implies that the flow near the wall could not be accurately resolved, representing a significant limitation of the model. In Fig. 7-11 and Fig. 7-12 are showed the Y^+ values at two different cavitation numbers $\sigma_D = 0{,}51$ and $\sigma_D = 0{,}88$ respectively.

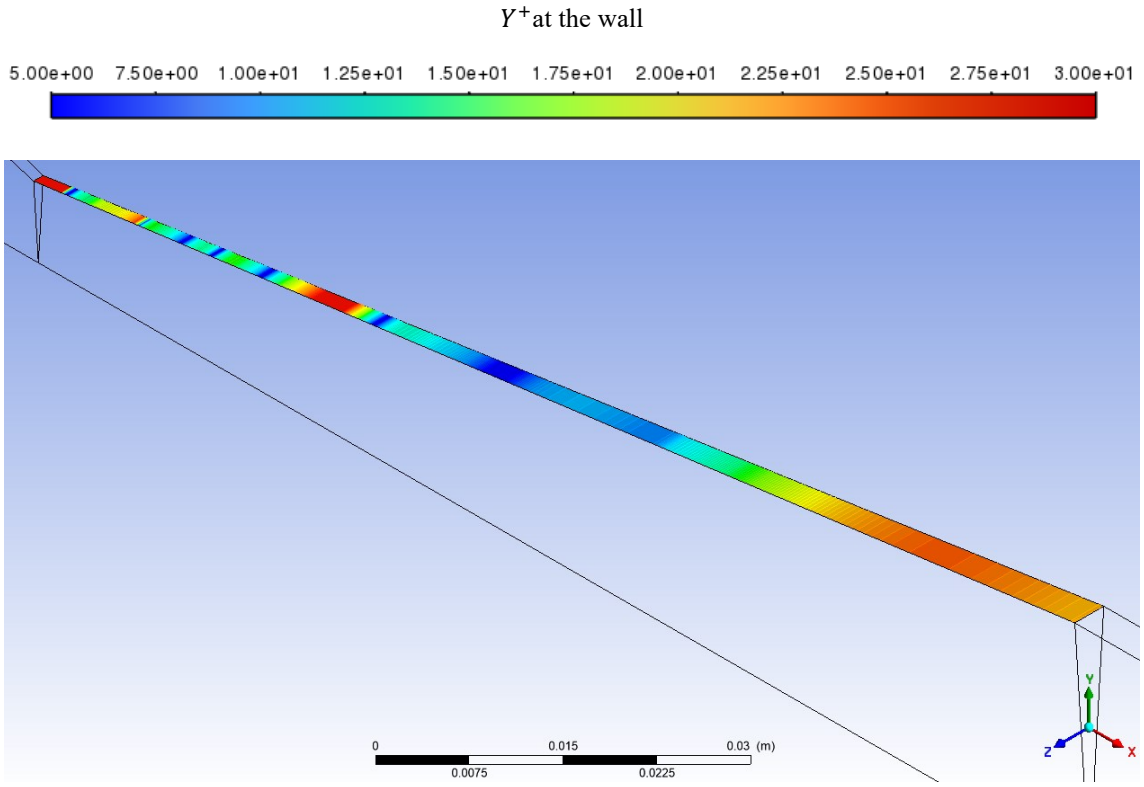

Figure 7-11: values of Y^+ at the divergent with a cavitation number $\sigma_D = 0{,}51$.

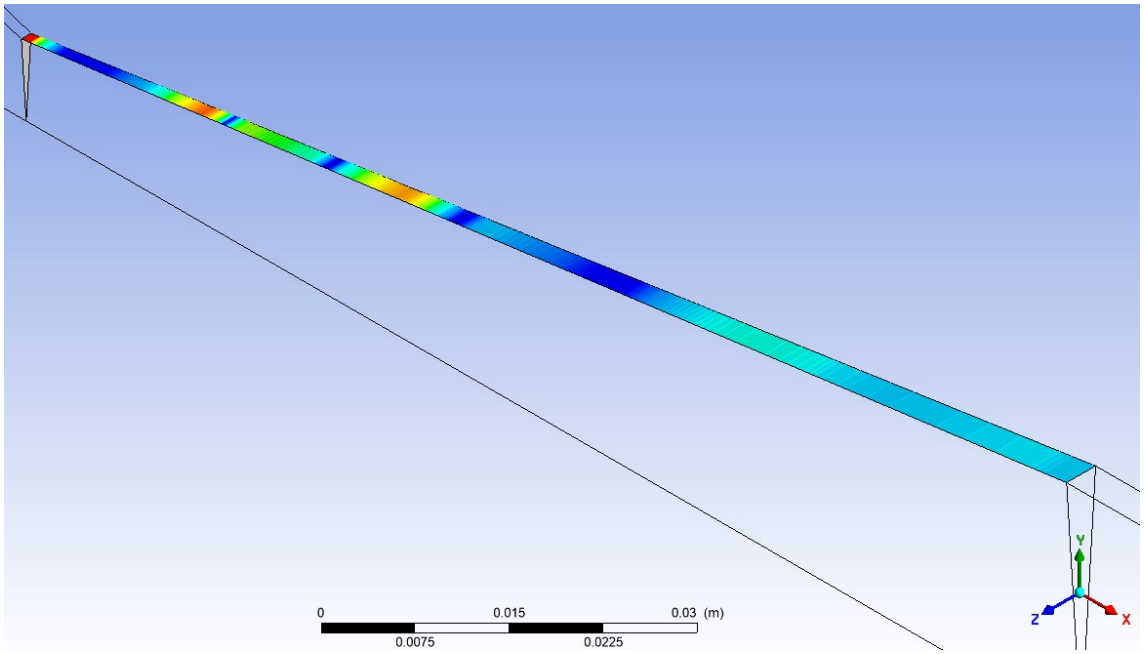

Figure 7-12: values of Y^+ at the divergent with a cavitation number $\sigma_D = 0{,}88$.

It is evident from the figures how the two limits of five and thirty are obtained just in a restricted zone of the wall, while in a major part of it the Y^+ dimensionless number describes the coincidence to the buffer layer zone. Depending on the cavitation number its value is closer to the lower limit of five for high cavitation numbers, while is closer to the value of thirty for low cavitation numbers but in both cases, it remains in the buffer layer zone.

This problem is due to an excessive coarse mesh at the wall in radial direction. To solve this problem bias in the number of divisions in radial directions were considered, but not adopted due to problems in convergence. Another way to pass this limitation could have been to increase in radial direction the number of divisions without bias, but this would increase excessively the number of cells in the mesh leading to an excessive computational time and effort.

8 Conclusion

The objective of this thesis was to develop an efficient CFD model capable of accurately describing cavitation phenomena in a Venturi tube while accounting for the compressibility effects of the vapor phase. This approach addresses a significant simplification commonly used in CFD modelling for cavitation, which assumes the vapor phase is incompressible.

The reference for the study was the works of Jahangir [1] and Brunhart [2], as the Venturi geometry, the experimental data and several features of the model were derived from these studies. Initially, the theory underlying vapor compressibility was examined demonstrating that treating the vapor as an ideal gas is a valid assumption. The next step involved the construction of the model. Following the creation of the geometry, a computational mesh was generated based on the particular requirements and convergence difficulties. A mesh sensitivity analysis was then conducted, using the pressure drop between the inlet and outlet of the domain and the computational time as key parameters between five meshes. The model setup was primarily based on insights from the literature, ensuring that the numerical analysis closely replicated the real phenomenon. Two custom UDFs were developed and implemented. The first UDF accounted for vapor compressibility, based on the theoretical framework discussed earlier. The second UDF limited turbulent viscosity, a necessary adjustment to accurately simulate the shedding mechanism in the numerical simulations.

In all simulations, first an initial transient regime that do not reflect the real phenomenon occurred, creating convergence problems at high inlet velocities, solved running the numerical resolution without the UDF for the vapour compressibility for few timesteps. After the transient regime, the real cavitation phenomenon reflecting the values and behaviour expected occurred. Regarding the two different shedding mechanisms some differences from the experimental behaviour were noted. In the re-entrant jet mechanism, the numerical solution was close the experimental behaviour as the re-entrant jet evolution in time was congruent with the experimental results. The main difference for this shedding mechanism was the total vapour condensation in the venturi after the first bubble implosion. As regards instead the condensation shock mechanism, more

incongruences were noted. First, in the numerical solution there is the presence of a big re-entrant jet at the start of the cycle with a successive detachment from the wall that do not reflect the real phenomena. After instead reflecting the experimental data a stable wall-attached cavity develops and after the downstream bubble implosion separate in small bubbles becoming a vapour cloud. However, while in the experiment this vapour cloud just flows in the divergent and condenses after the formation of a new stable cavity at the throat, in the simulations conducted in this work it completely condenses. The numerical results were successively validated using the dimensionless numbers and the graph used in the work of Brunhart [2]. As regard the performance of the model, in the $K - \sigma_D$ graph, it showed a good agreement with the experimental results of Jahangir [1] even better than the work of Brunhart [2]. Instead, as regards the frequency of the phenomenon, in the graph $St_d - \sigma_D$ it is evident how the numerical solution of the model does not reflect the experimental results. In particular, for the high cavitation numbers the frequency registered was half or even less than the experiment.

The main limit of the study is represented by an inefficient value of the dimensionless number Y^+. Its values in all the simulations are in the buffer layer zone, where the solver is not able to resolve precisely the boundary layer at the wall.

In future studies, finer meshes, particularly in the radial direction of the geometry, can be tested using the proposed UDF to achieve lower Y^+ values. This would help verify whether the frequency discrepancies observed in the phenomenon are due to this limitation. Additionally, other simulation setups can be explored, including the implementation of a mesh with radial bias in element size. Furthermore, models found in the literature that use a barotropic UDF to simulate the cavitation process could integrate the UDF developed in this work for vapor compressibility within the vapor phase section.

To conclude, the model demonstrated valid results regarding the performance of the venturi reactor but less regarding the frequency of the cavitation phenomenon. This work can be used for future studies in the cavitation phenomenon accounting for the vapour phase compressibility using the UDF constructed.

9 Bibliography

[1] S. Jahangir, Experimental Investigation of Partial Cavitation, Delft University of Technology, 2020.

[2] Brunhart Maxwell, “Investigation of cavitation and vapor shedding mechanisms,” *Physics of Fluids,* no. 32.8, 2020.

[3] B. Cointe, “CFD Analysis of Cavitation Dynamics in a converging diverging nozzle,” 2018.

[4] M. Dular, T. Požar, J. Zevnik and R. Petkovšek, “High speed observation of damage created by a collapse of a single,” *Wear,* pp. 13-23, 2019.

[5] Y. G. Adewuyi, “Sonochemistry: Environmental Science and Engineering,” *Ind. Eng. Chem. Res.,* pp. 4681-4715, 2001.

[6] J. Carpenter, M. Badve, S. Rajoriya, S. George, V. K. Saharan and A. B. Pandit, “Hydrodynamic cavitation: an emerging technology for the intensification of various chemical and physical processes in a chemical process industry,” *Reviews in Chemical Engineering,* January 2016.

[7] Z. Zhang, P. W. Shichuan Wei a, W. Qiu and G. Zhang, “Progress in applications of laser induced cavitation on surface processing,” *Optics and Laser Technology,* vol. 170, 2024.

[8] T. Q. Bui, H. T. M. Ngo and H. T. Tran, “Surface-protective assistance of ultrasound in synthesis of superparamagnetic magnetite nanoparticles and in preparation of mono-core magnetite-silica nanocomposites,” *Journal of Science: Advanced Materials and Devices,* pp. 323-330, 2018.

[9] M. Ashokkumar, “The characterization of acoustic cavitation bubbles – An overview,” *Ultrasonics Sonochemistry,* p. 864–872, 2011.

[10] P. P. Gohil and a. R. P. Saini, “Numerical Study of Cavitation in Francis Turbine of a Small Hydro Power Plant,” *Journal of Applied Fluid Mechanics,* vol. 9, no. 9, pp. 357-365, 2016.

[11] O. P. Stebeleva and a. A. V. Minakov, “Application of Cavitation in Oil Processing: An Overview of Mechanisms and Results of Treatment,” *ACS Omega,* vol. 6, p. 31411−31420, 2021.

[12] G. Darandalea, M. Jadhava, A. Waradeb and V. S. Hakke, “Hydrodynamic cavitation a novel approach in wastewater treatment: A review,” *Materials Today: Proceedings,* vol. 77, p. 960–968, 2023.

[13] T. A. Bimestrea, J. A. M. Júniorb, C. A. Boturab, E. Canettieria and C. E. Tunaa, “Theoretical modeling and experimental validation of hydrodynamic cavitation reactor with a Venturi tube for sugarcane bagasse pretreatment,” *Bioresource Technology,* vol. 311, 2020.

[14] H. Soyama, “Luminescence intensity of vortex cavitation in a Venturi tube changing with cavitation number,” *Ultrasonics Sonochemistry,* vol. 71, 2021.

[15] Z. Li, Z. Zuo and Z. Qian, “A Venturi tube design for studying travelling bubble cavitation,” *Journal of Physics: Conference Series,* vol. 2217, 2022.

[16] T. Pham, F. Larrarte and D. Fruman, “Investigation of Unsteady Sheet Cavitation and cloud cavitation mechanism,” *Journal of Fluids Engineering,* vol. 121, p. 289–296, 1999.

[17] Y. Kawanami, H. Kato, H. Yamaguchi, M. Tanimura and Y. and Tagaya, “Mechanism an control of cloud cavitation,” *Journal of Fluids Engineering,* vol. 119, 1997.

[18] M. Callenaere, J.-P. Franc, J.-M. Michel and M. and Riondet, “The cavitation instability induced by the development of a re-entrant jet,” *Journal of FluidMechanics,* vol. 444, pp. 223-256, 2001.

[19] A. Kumar, A. Ghobadian and J. M. Nouri, “Assessment of Cavitation Models for Compressible Flows Inside a Nozzle,” *Fluids,* vol. 5, no. 134, 2020.

[20] A. Laugier and J. Garai, “Derivation of the ideal gas law,” *journal of chemical education,* vol. 84, no. 11, pp. 1832-1833, 2007.

[21] K. M. Tenny and J. S. Cooper., “ideal gas behavior,” 2017.

[22] L. A. Kareem, T. M. Iwalewa and M. Al-Marhoun, “New explicit correlation for the compressibility factor of natural gas: linearized z-factor isotherms,” *Journal of Petroleum Exploration and Production Technology,* December 2015.

[23] Phase Behavior of Natural Gas and condensate, “Principle of Corresponding States (PCS),” [Online]. Available: https://www.e-education.psu.edu/png520/m8_p2.html.

[24] Cardozo-Filho, G. B. M. d. Souza, M. B. Pereira, L. C. Moura˜o, M. P. d. Santos, J. A. d. Oliveira, I. A. A. Garde, C. G. Alonso, V. Jegatheesan and L. cio, “Supercritical water technology: an emerging treatment,” *Reviews in Environmental Science and Bio/Technology,* pp. 75-104, 2022.

[25] San Diego University, “Nelson Obert Compressiblity Charts,” [Online]. Available: https://energy.sdsu.edu/testhome/tablesModule/tablesRG/zNO.html.

[26] H. Gholizadeh, R. Burton and G. Schoenau, “FLUID BULK MODULUS: A LITERATURE SURVEY,” *International Journal of Fluid Power 12,* pp. 5-15, 2011.

[27] unacademy, “Bulk Modulus for Gases,” [Online]. Available: https://unacademy.com/content/jee/study-material/chemistry/bulk-modulus-for-gases.

[28] Massachusetts institute of technology, [Online]. Available: https://web.mit.edu/8.03-esg/watkins/8.03/bmod.pdf.

[29] A. D. Pierce, ACOUSTICS. An Introduction to Its Physical Principles and Applications, Frank J. Cerra and Madelaine Eichberg, 1981.

[30] S. L. Garrett, Understanding Acoustic. An Experimentalist's View of Sound and Vibration, Springer Nature, 2020.

[31] IOWA STATE UNIVERSITY, "Physics of Nondestructive Evaluation - Sound," [Online]. Available: https://www.nde-ed.org/Physics/Sound/index.xhtml.

[32] Geeksforgeeks, "Speed of Sound," 2023. [Online]. Available: https://www.geeksforgeeks.org/speed-of-sound.

[33] K. A. K. a. S. H. Sohrab*, "On the Speed of Sound," *International Journal of Thermodynamics (IJoT),* pp. 29-34, 2016.

[34] V. G. Kirtskhalia, "Speed of Sound in Atmosphere of the Earth," *Open Journal of Acoustics,,* pp. 80-85, 2012.

[35] S. Benjelloun and J.-M. Ghidaglia, "On the sound speed in two-fluid mixtures and the implications for CFD model validation," Mohammed VI Polytechnic University, 2020.

[36] H. Shamsborhan, O. Coutier-Delgosha, G. Caignaert and F. A. Nour, "Experimental determination of the speed of sound in cavitating," *Exp Fluids,* pp. 1359-1373, 2010.

[37] S. W. KIEFFER, "Sound Speed in Liquid-Gas Mixtures' Water-Air and Water-Steam," *JOURNAL OF GEOPHYSICAL RESEARCH,* 1977.

[38] H. K. Versteeg and W. Malalasekera, An Introduction to Computational Fluid Dynamics, Pearson Prentice Hall, 2007.

[39] A. Sayma, Computational Fluid Dynamics, Elsevier, 2009.

[40] J. Blazek, COMPUTATIONAL FLUID DYNAMICS: PRINCIPLES AND APPLICATIONS, Elsevier, 2001.

[41] F. Magoulès, Computational Fluid Dynamics, CHAPMAN & HALL/CRC, 2011.

[42] H.-G. Kim, "A Method of Accelerating the Convergence of Computational Fluid Dynamics for Micro-Siting Wind Mapping," *Computation,* vol. 7, no. 22, 2019.

[43] V. KOTRA, S. K. KONIDALA, N. ANUSHA, R. N. RAO and B. H. BABU, "Recent Advances and Applications of Turbulent Flow Chromatography," *ASIAN JOURNAL OF CHEMISTRY,* vol. 29, no. 4, pp. 771-778, 2017.

[44] SIMSCALE, "K-Omega Turbulence Models," SIMSCALE, [Online]. Available: https://www.simscale.com/docs/simulation-setup/global-settings/k-omega-sst/.

[45] AFS ENEA, "Standard, RNG, and Realizable k-epsilon Models," [Online]. Available: https://www.afs.enea.it/project/neptunius/docs/fluent/html/th/node57.htm.

[46] NASA-Langley Research Center, "Wilcox k-omega Model - Turbulence Modeling Resource," 2024. [Online]. Available: https://turbmodels.larc.nasa.gov/wilcox.html.

[47] AFS ENEA, "Standard k-omega model," [Online]. Available: https://www.afs.enea.it/project/neptunius/docs/fluent/html/th/node66.htm.

[48] AFS ENEA, "Shear-Stress Transport (SST) k-omega Model," [Online]. Available: https://www.afs.enea.it/project/neptunius/docs/fluent/html/th/node67.htm.

[49] SIMTEQ ENGINEERING, "Targeting a Specific y+ Value for your Turbulent Flow CFD Simulation (Part 1)," [Online]. Available: https://simteq.co.za/blog/targeting-a-specific-y-value-for-your-turbulent-flow-cfd-simulation-part-1/.

[50] CFD LAND, "What is y+ in CFD," [Online]. Available: https://cfdland.com/what-is-y-plus-in-cfd/.

[51] J. Febina, M. Y. Sikkandar and N. M. Sudharsan, "Wall Shear Stress Estimation of Thoracic Aortic Aneurysm Using Computational Fluid Dynamics," *Computational and Mathematical Methods in Medicine,* vol. 2018, 2018.

[52] T. S. Folden and F. J. Aschmoneit, “A classification and review of cavitation models with an emphasis on physical aspects of cavitation,” *Physics of Fluids,* vol. 35, 2023.

[53] AFS ENEA, “ANSYS FLUENT 12.0 Theory Guide - 16.7.4 Cavitation Models,” [Online]. Available: https://www.afs.enea.it/project/neptunius/docs/fluent/html/th/node343.htm#eqn5.

[54] D. O. Villafranco, H. K. Do, S. M. Grace, E. M. Ryan and R. G. Holt, “ASSESSMENT OF CAVITATION MODELS IN THE PREDICTION OF CAVITATION IN NOZZLE FLOW,” *Proceedings of the ASME,* 2008.

[55] J. Hilsenrath, C. W. Beckett, W. S. Benedict, L. Fano, H. J. Hoge, J. F. Masi, R. L. Nuttall, Y. S. Touloukian and H. W. Woolley, Tables of Thermal Properties of Gases, National Bureau of Standards Circular 564, 1955.

[56] H.-J. Kretzschmar and W. Wagner, International Steam Tables, Springer Vieweg, 2024.

[57] F. Magoulès, Computational Fluid Dynamics, CHAPMAN & HALL/CRC, 2011.

[58] SIMSCALE, “Mesh quality,” [Online]. Available: https://www.simscale.com/docs/simulation-setup/meshing/mesh-quality/.

[59] cfmesh, “Is It Always The Mesh? Part 1: Discretisation Basics And Mesh-Quality Metrics,” [Online]. Available: https://cfmesh.com/is-it-always-the-mesh-part-1-discretisation-basics-and-mesh-quality-metrics/.

[60] MECHEAD, “Ansys Mesh Metrics Explained,” [Online]. Available: https://www.mechead.com/mesh-quality-checking-ansys-workbench/.

[61] M. D. l. Cruz-Ávila, J. E. D. León-Ruiz, I. Carvajal-Mariscal and J. Klapp, “CFD Turbulence Models Assessment for the Cavitation Phenomenon in a Rectangular Profile Venturi Tube,” *fluids,* vol. 9, no. 71, 2024.

[62] J.-L. Reboud, B. Stutz and O. Coutier, “Two-phase flow structure of cavitation: Experiment and modelling of unsteady effects.,” in *In proceedings of the 3rd International Symposium on Cavitation CAV1998*, Grenoble, 1988.

[63] P. Pipp, M. Hoˇcevar and M. Dular, “Numerical Insight into the Kelvin-Helmholtz Instability Appearance in Cavitating Flow,” *applied sciences,* vol. 11, no. 2644, 2021.

[64] W. Jian, M. Petkovšek, L. Houlin, B. Širok and M. Dular, “Combined numerical and experimental investigation of the cavitation erosion process.,” *Journal of Fluids Engineering,* 2015.